LUND UNIVERSITY

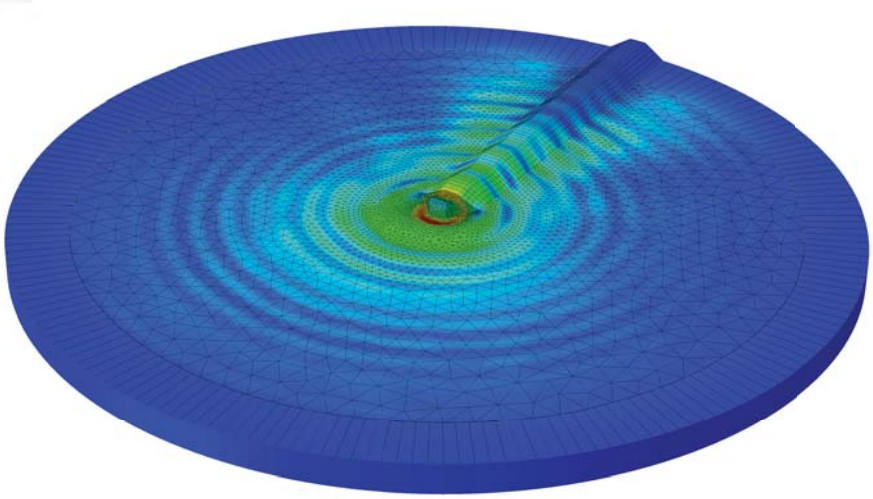

DYNAMIC SOIL-STRUCTURE INTERACTION OF PORTAL FRAME BRIDGE WALLS FOR HIGH-SPEED RAILWAYS

HENRIK MALM

Structural Mechanics

Master's Dissertation

DEPARTMENT OF CONSTRUCTION SCIENCES
DIVISION OF STRUCTURAL MECHANICS

ISRN LUTVDG/TVSM--16/5219--SE (1-109) | ISSN 0281-6679
MASTER'S DISSERTATION

DYNAMIC SOIL-STRUCTURE INTERACTION OF PORTAL FRAME BRIDGE WALLS FOR HIGH-SPEED RAILWAYS

HENRIK MALM

Supervisors: Professor **PER-ERIK AUSTRELL**, Div. of Structural Mechanics, LTH,
together with **MAHIR ÜLKER-KAUSTELL**, PhD and **JOHAN ÖSTLUND**, MSc, Tyréns AB.
Examiner: Professor **KENT PERSSON**, Div. of Structural Mechanics, LTH.

Printed by Media-Tryck LU, Lund, Sweden, October 2016 *(Pl)*.

For information, address:
Division of Structural Mechanics,
Faculty of Engineering LTH, Lund University, Box 118, SE-221 00 Lund, Sweden.
Homepage: www.byggmek.lth.se

Preface

This master's thesis was initiated in cooperation between the Division of Structural Mechanics at Lund University and the bridge department at Tyréns AB.

I would like to address my sincerest gratitude to my supervisor, Ph.D. Mahir Ülker-Kaustell at Tyréns AB, for his enthusiasm and excellent support and guidance throughout the course of this work. Thanks also to my supervisor Johan Östlund, Ph.D. student at KTH and Tyréns, who has been of huge help when I have been running into trouble, and whose master's thesis has been an enormous source of inspiration for me.

Furthermore, I would like to thank my supervisor at LTH, Prof. Per-Erik Austrell at the Division of Structural Mechanics, for guidance and for invaluable knowledge in the field of structural dynamics. My examiner, Prof. Kent Persson at the Division of Structural Mechanics at LTH has been of great help by letting me partake in a project, enabling the whole thesis through access to the supercomputers of Lunarc. Thanks also to Anders Sjöström at Lunarc and LTH, for help with troubleshooting when using the supercomputers.

I would like to thank Scanscot Technology AB, for sponsoring me with a license to the finite element software BRIGADE Plus. I am also very grateful to Tyréns AB for providing me with workspace during the work with the thesis and I owe a special thanks to the entire staff of the bridge department of said company for making the time there much enjoyable.

Finally, I would like to thank my famly, friends and loved ones for the support they have given me throughout my five years at LTH.

Malmö, October 2016

Henrik Malm

Abstract

In Sweden, high-speed railways is a subject for public debate. The first stage of a high-speed train network, Ostlänken between Stockholm and Linköping, is under investigation, and is planned to be trafficked in 2028. The high-speed railway is intended to hold traffic with speeds up to 320 km/h. At such speeds, the design requirements of the accelerations of the bridge superstructure become more stringent. Previous studies show that the interaction between the bridge and the backfill soil can reduce these accelerations.

In this thesis, dynamic soil-structure interaction (SSI) of portal frame bridge walls has been studied. The SSI was represented by complex impedance functions that were calculated and analyzed for different parameters of a bridge-embankment interface.

The impedances, representing dynamic stiffness and damping, were in this thesis calculated in the frequency domain with finite element (FE) software, by performing steady state analyses on 3D solid bridge-embankment models. To discretize the infinite extent of an embankment, the *standard viscous boundary* method was used, implemented by inserting infinite continuum elements at the boundary in the FE-software ABAQUS. The method showed successful with mitigating waves at the boundary. A parameter study was conducted, where the influence of geometries and material properties were shown through a comparison of impedance functions. Both embankments on a fixed boundary, representing bedrock, and embankments on circular ground soil plates of various thickness and stiffness, were compared.

SSI showed to induce large amounts of dynamic stiffness and damping to a bridge structure. A stiffer embankment, as well as a stiffer ground soil, has shown large influence on the dynamic stiffness and is believed to reduce vibrations in a bridge deck. The study suggested that proper material modeling is important for both the soil and the concrete, to receive accuracy in the impedance functions. The work also indicates that a properly designed bridge wall geometry could be an important step towards developing the design of future high-speed railway bridges.

Keywords: SSI, soil-structure interaction, structural dynamics, high-speed railway bridges, impedance, receptance, finite element method, portal frame bridge

Sammanfattning

I Sverige är höghastighetsjärnvägar ett debatterat ämne. Undersökningsarbeten har startat för det första steget i ett höghastighetsnät – Ostlänken mellan Järna och Linköping – som planeras vara trafikerad år 2028. Höghastighetsjärnvägen är avsedd att tillåta hastigheter på 320 km/h. Vid så höga hastigheter blir dimensioneringskraven för brobanans vibrationer strängare. Tidigare studier har visat att dessa vibrationer kan reduceras om man tillgodoräknar sig interaktionen mellan bron och jordbanken.

Det här examensarbetet behandlar dynamisk jord-struktur-interaktion (SSI, från Soil-structure Interaction) för ramben på plattrambroar. SSI representeras här av komplexa impedansfunktioner som har beräknats och analyserats för olika parametrar i ett gränssnitt mellan jord och bro.

I examensarbetet beräknades impedanser, som representerar dynamisk styvhet och dämpning, i frekvensdomänen genom steady-state analyser på tredimensionella FE-modeller som utgjordes av ett ramben och en intilliggande jordbank. För att avgränsa den oändliga utsträckningen av en jordbank, användes den så kallade *standard viscous boundary*-metoden, vilken implementeras i FE-mjukvaran ABAQUS genom 3D-element som simulerar oändlig utsträckning. Metoden visade sig effektivt kunna dämpa ut vågrörelser som nådde jordbankens bortre gräns. En parameterstudie utfördes, där betydelsen av geometrier och materialegenskaper kunde påvisas genom att jämföra impedansfunktioner. I parameterstudien jämfördes både modeller med jordbank på berggrund och jordbank på cirkulära jordskivor av olika djup och styvhet med varandra.

Studien visade att SSI kan bidra mycket till dynamisk styvhet och dämpning för en vidhängande struktur. Styvare jordbank, såväl som styvare mark, visade sig i stor utsträckning påverka den dynamiska styvheten, och tros kunna reducera vibrationerna i den intilliggande brobanan. Studien antyder att noggrant valda materialegenskaper i både jorden och betongen är viktigt för noggrannheten i uppskattning av impedansen. Studien visade även tendenser till att vidare utredning av utformningen av rambenen är ett viktigt steg för att utforma framtidens höghastighetsjärnvägsbroar.

Sökord: SSI, jord-struktur-interaktion, strukturdynamik, höghastighetståg, järnvägsbro, impedans, receptans, finita elementmetoden, plattrambro

Abbreviations

Abbreviation	Description
2D	Two-dimensional
3D	Three-dimensional
BC	Boundary Condition
CPU	Central Processing Unit
DFT	Discrete Fourier Transform
DOF	Degree of Freedom
FE	Finite Element
FEM	Finite Element Method
HEX	Hexahedral
FFT	Fast Fourier Transform
FRF	Frequency Response Function
GPU	Graphics Processing Unit
GUI	Graphical User Interface
HSR	High-speed Railway
HSLM	High-speed Load Model
OCR	Over Consolidation Ratio
SGI	Swedish Geotechnical Institute
SSH	Secure Shell
SSI	Soil-structure Interaction
TET	Tetrahedral

Table of Contents

Chapter 1

Introduction

1.1 High-speed trains and portal frame bridges

In Sweden, high-speed railways (HSR) is a subject for public debate. High-speed connections between Stockholm, Gothenburg and Malmö is supposed to relieve the existing rail network in favor for freight traffic, as well as to satisfy a changed demand for mobility with fast, environmental friendly connections to the rest of Europe. The railway network is as of today planned to be stretched according to Figure 1.1, and will with speeds up to 320 km/h make it possible to travel between Stockholm and Gothenburg in 2 hours, and between Stockholm and Malmö in 2.5 hours. The first stage of the high-speed train network – Ostlänken between Stockholm and Linköping – is under investigation, and is planned to be trafficked in 2028.

The high-speed line is intended to hold traffic with speeds up to 320 km/h. At such speeds, the design requirements for railway bridges become more stringent. Reasons for this is that increased speeds mean higher loading frequencies, which lead to higher risks of hitting the bridge's resonance frequencies. This might lead to several complications due to the large accelerations in the bridge superstructure, including faster deterioration of the tracks and the superstructure itself. In the future, it would be highly desirable to be able to produce reliable predictions of vibrations in bridges along high-speed railways.

In parallel, the demand for increasing train speeds on the existing train network grows larger. Better understanding of the parameters influencing the dynamic behavior of train bridges can reduce the costs for such projects, when existing bridges can be validated to hold for increased speeds due to a lesser need for safety factors, which today is the way of dealing with uncertainties in the design models.

Figure 1.1: Planned high-speed network in Sweden, connected to the rest of Europe, through Denmark. From Andersson and Karoumi (2015).

According to research made by, for example, Talkemiya & Bian (2007) and Ülker-Kaustell (2009), soil-structure interaction (SSI) can have an important effect on the stiffness and damping of the structural system, especially on short and stiff structures such as portal frame bridges. It has been shown in previous research (Östlund, 2016), that including SSI as boundary conditions in end-frame bridges can limit the bridge's displacements and accelerations. The same is believed to hold also for portal frame bridges.

One of the most commonly used railway bridge designs in Sweden is the portal frame bridge. Portal frame bridges are commonly used for spans less than 30 meters and have the advantage that the road or railway does not have to be elevated to cross an obstacle. Such is the case in for example a railway crossing a pedestrian subway, or a smaller road, as is illustrated in Figure 1.2. The bridge is cast in one piece and embedded by backfill on both sides. Depending on the type of soil, the foundation can either be deep (pile groups) or shallow (open or closed plate).

Figure 1.2: Portal frame bridge in Dagstorp north of Lund. From BaTMan (2015).

Dynamic analyses of portal frame bridges are often performed with FE software using shell and beam theory. Typically, no consideration of the interaction with the surrounding soil is taken, due to increased computation cost, geotechnical uncertainties and modeling complexities. In Figure 1.3, three ways to model a portal frame bridge foundation are shown schematically. One of these is to model the effects of the surrounding soil by applying static springs and dashpots to the foundation. Apart from being a complex matter to determine the correct parameters of these springs and dashpots, they do not take into account the moving nature of the masses of the backfill.

A way of taking the dynamic nature of the soil into account is to calculate impedance functions, and then apply them to the bridge model as boundary conditions with dynamic spring and dashpot coefficients. In the bottom figure, these boundary conditions are obtained through the SSI in the interface between soil and the portal frame bridge foundation. In this thesis, the same type of boundary conditions will be obtained, but for the interface between the soil and the bridge wall. The difficulties with this method is of the same nature as when using static springs, that more soil parameters than those obtained through a regular geotechnical survey need to be determined.

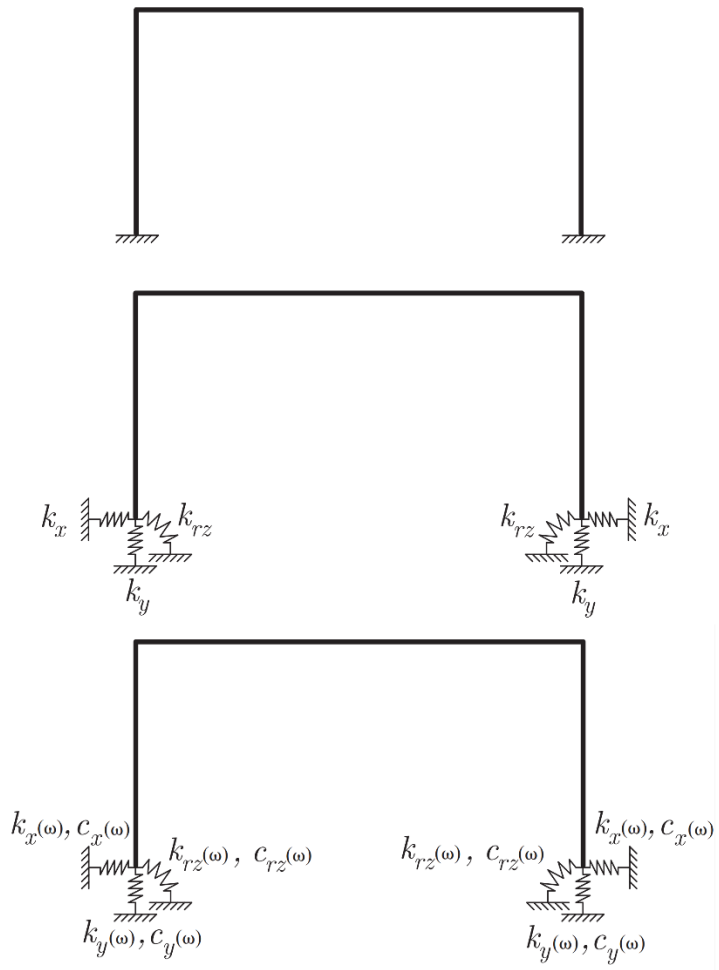

Figure 1.3: Three different boundary conditions for the foundation in a 2D-model of a portal frame bridge. *Top:* Clamped. *Middle:* Static springs. *Bottom:* Dynamic springs and dashpot coefficients. From (Ülker-Kaustell, 2009).

1.2 Objective

Dynamic soil-structure interaction (SSI) of portal frame bridges will be studied. The aim is to develop a numerical model for evaluation of dynamic impedance functions for a variation of soil layer profiles, geometries and levels of detail in the model. The impedance functions can then be used as boundary conditions in a simplified finite element (FE) bridge-model.

The intention of this study is to provide a finite element-model that can work as a platform for future research, and to perform a parameter study on how different factors, such as the material properties of the soil, influence the interaction with the structure.

1.3 Dynamic design requirements to Eurocode

On railway lines with speed limits exceeding 200 km/h, a dynamic analysis is required in addition to the static one required for all bridges (TRVK Bro, 2011). As mentioned before, higher speeds lead to increased risk for resonance in the bridge. The main difference between the static and dynamic analysis is that the dynamic consider the effects of resonance. According to Eurocode – Basis of Structural Design (SS-EN 1990, 2002) – the following bridge responses must be checked in a dynamic analysis:

- Vertical bridge deck acceleration
- Vertical and horizontal displacements
- Rotations at bearings and supports
- Torsions

The maximum vertical bridge deck accelerations are 3.5 m/s^2 for a ballasted track and 5 m/s^2 for an un-ballasted track. The requirement is set lower for a ballasted track because of risk for ballast instability from high accelerations. The requirements are also set in consideration of traveler comfort and for reducing risk of derailing. The maximum displacement of the bridge depend on span length and train speed, and is obtained in Eurocode (SS-EN 1990, 2002) through the diagram shown in Figure 1.4. The span length versus displacement ratios obtained from Figure 1.4 should be multiplied with a reduction factor depending of the type of bridge: 0.7 for simply supported bridges with one or two spans, and for continuous bridges with two spans; 0.9 for continuous bridges with three or more spans.

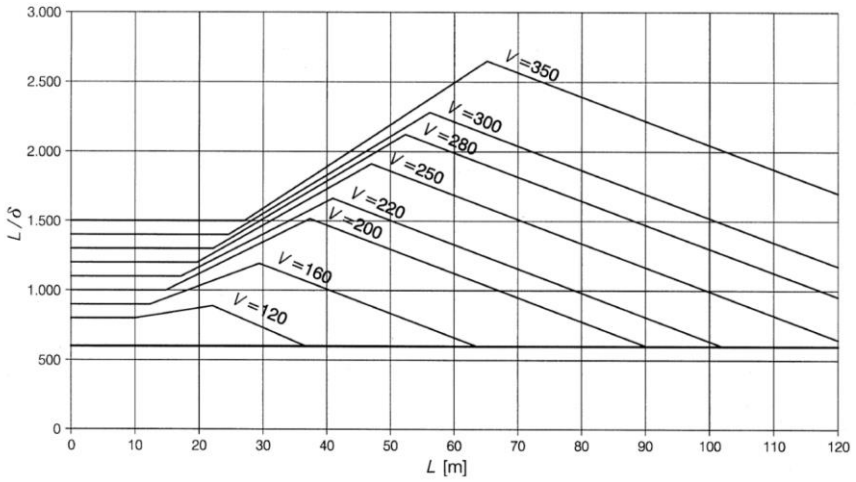

Figure 1.4: Figure A2.3. in SS-EN 1990 (2002). The vertical axis gives the limiting ratio between span length and displacement for a specific train speed.

Concerning loading, the load model that should be used for dynamic analysis according to Eurocode is the high speed load model, HSLM. It is subdivided into HSLM-A and HSLM-B, where HSLM-B comprises a series of moving point loads with equal spacing, and HSLM-A consists of sets of 10 different point load configurations, resembling real trains, see Figure 1.5.

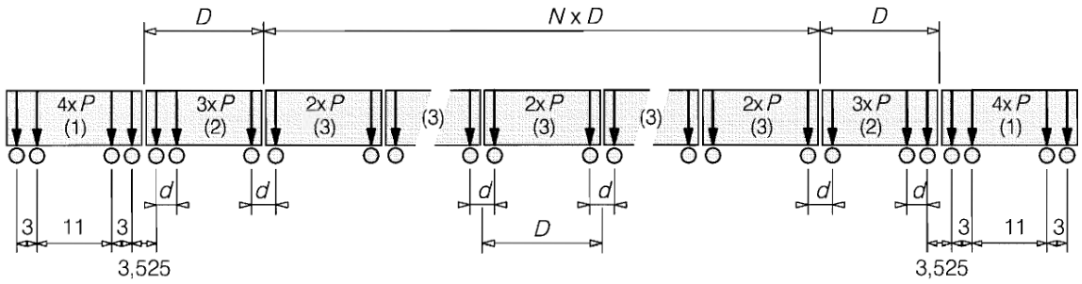

Figure 1.5: HSLM-A. Train load model according to SS-EN 1991-2 (2003).

Chapter 2

Theory

In this chapter, a brief theoretical background to the methods used in this thesis will be given. For a more detailed description of the finite element-method and structural dynamics, the reader is referred to standard textbooks such as (Zienkiewicz & Taylor, 2000), (Ottosen & Petersson, 1992) and Chopra (2014), being the only sources that sections (2.1) and (2.2) are based on.

2.1 The finite element method

The finite element method (FEM) is an approximate numerical method of solving differential equations for field problems such as stress analysis, often encountered in engineering mechanics. A one-, two-, or three-dimensional region, for which a certain physical problem can be described by a differential equation, is divided in smaller parts, so-called finite elements, assigned certain material properties. Through so-called shape functions, the field variable within each element is prescribed a certain spatial variation. The differential equation can thus be calculated for each element, and through element nodes the elements can be assembled. The aim of the discretization of the region into elements is that the approximate solution should converge towards the exact, analytical solution when decreasing the element size (the convergence requirement). In stress analysis, each node is assigned a freedom to translate and rotate in a given way, which enables equilibrium equations to be formulated for each degree of freedom. The equation to be solved in a static analysis is:

$$\mathbf{Ku} = \mathbf{f} \tag{2.1}$$

where $\mathbf{K}$ is the stiffness matrix, $\mathbf{u}$ is the displacement vector and $\mathbf{f}$ is the loading vector.

2.2 Structural dynamics

In some sense, all loads are of dynamic nature. Applying a static load will cause a displacement in the loaded structure, and has thereby caused a dynamic movement. It will, however, not cause a considerable acceleration of the structure, and Newton's first law of motion is applicable. The distinction between static and dynamic analysis is made on the basis of whether the force gives enough acceleration compared to the structure's natural frequency. Large accelerations can emerge from periodic loading or if the load is applied suddenly, i.e. through an impact. The dynamics of a single d.o.f. system with a mass, a spring and a viscous damper, illustrated in Figure 2.1, is governed by the equation of motion:

$$m\ddot{u} + c\dot{u} + ku = f(t), \tag{2.2}$$

where m is the mass, c is the viscous damping coefficient of the dashpot, k is the spring stiffness, $f(t)$ is the time dependent loading and $u, \dot{u}$ and $\ddot{u}$ is the displacement, velocity and acceleration respectively. If a system is subjected to a harmonic excitation, the force $f(t)$ in equation (2.2) can be written as $f(t) = f_0 \sin \omega t$, where f_0 is the force amplitude and ω is the forcing angular frequency.

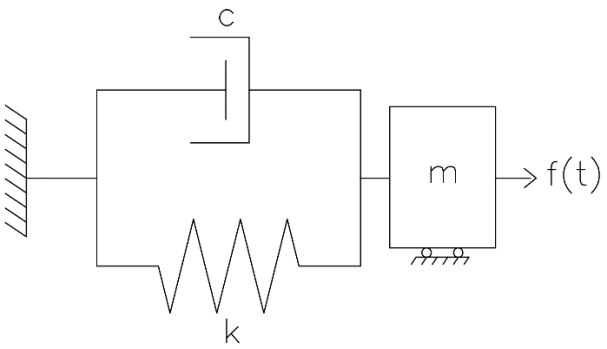

Figure 2.1: Single degree of freedom system with a mass, a spring and a viscous damper.

In structural dynamics, the natural frequency is central for describing the response of the system. The natural frequency, also called resonance frequency or eigenfrequency, can be calculated by setting the force to zero, and is thus the frequency in which the system tend to oscillate "by own means". Harmonic loading frequencies near the natural frequency amplifies the motions of the system and make it oscillate with larger amplitude. For equation (2.2), ignoring the damping, the natural frequency can be expressed as:

$$\omega_n = \sqrt{\frac{k}{m}} \tag{2.3}$$

Ignoring the damping is, however, a simplification. Introducing damping to the system yields a damped natural frequency, calculated as:

$$\omega_d = \omega_n\sqrt{1-\xi^2} \tag{2.4}$$

where ξ is the damping ratio, defined as:

$$\xi = \frac{c}{2\sqrt{km}} \tag{2.5}$$

For multiple degree of freedom systems, the equation of motion can be described as:

$$\mathbf{M\ddot{u} + C\dot{u} + Ku = f}(t) \tag{2.6}$$

which is the FE-formulation for a dynamic system with damping, where **M, C,** and **K** are the mass, damping and stiffness matrices, **u**, **u̇**, and **ü** response vectors and **f**(t) is a time dependent force vector. One way of discretizing the masses are to use lumped mass, which means to divide the mass and lump it at the nodes. In this way the mass matrix becomes diagonal, making the solution to the differential equation much simpler.

2.2.1 Steady state dynamics

A common topic in structural dynamics is the response of a system to harmonic loading. Understanding the system's response behavior to harmonic excitation at different frequencies also provide knowledge about the response to arbitrary load excitation cases. A harmonic steady state excitation implies that the excitation has existed for a long time, and thus that the transient vibration associated with the initial displacement and velocity has decayed. This implies that only the particular solution for the undamped version of equation (2.2),

$$u_p(t) = \frac{f_0}{k}\frac{1}{1-\left(\omega/\omega_n\right)^2}\sin\omega t\ , \qquad \omega \neq \omega_n, \tag{2.7}$$

is of interest when the excitation is a sinusoidal load. Equation (2.7) is thereby unaffected by the initial conditions and is called the steady-state vibration.

The steady-state dynamic response can be written as:

$$u(t) = \frac{f_0}{k}\left[\frac{1}{1-\left(\omega/\omega_n\right)^2}\right]\sin\omega t, \tag{2.8}$$

Varying the angular frequency ω can make the factor in brackets in equation (2.8) either positive or negative, which determines if the displacements will be in or out of

phase with the applied force. Introducing damping to the equation of motion, the steady-state response of a harmonic load with angular frequency ω can be written as:

$$u(t) = u_0 \sin(\omega t - \phi), \tag{2.9}$$

which indicates that there is a phase lag between the force and the response of the system. For elegance and computational ease, a frequency representation is more convenient. A Fourier transform, explained in a subsequent section, yields:

$$f(t) = F(\omega)e^{i\omega t} \tag{2.10}$$

and

$$u(t) = U(\omega)e^{i\omega t}, \tag{2.11}$$

with the derivatives:

$$\dot{u}(t) = i\omega U(\omega)e^{i\omega t} \tag{2.12}$$

$$\ddot{u}(t) = -\omega^2 U(\omega)e^{i\omega t} \tag{2.13}$$

Canceling the $e^{i\omega t}$ term in each of equations (2.10)-(2.13) gives the steady state amplitude of a single d.o.f. system:

$$U(\omega) = \frac{F(\omega)}{[k - \omega^2 m + i\omega c]} \tag{2.14}$$

In equation (2.14), damping is as mentioned also considered giving the steady state behavior of the system in Figure 2.1.

2.2.2 Damping

Damping is the process by which vibration steadily diminishes in amplitude. It arises from strain energy and kinematic energy being dissipated due to various mechanisms. All structures have a certain amount of damping that contribute to the vibrating response to excitation. In a free vibration test, without damping the vibrations would go on forever with constant amplitude and for a forced response at resonance frequencies the amplitude would increase towards infinity.

The mechanisms causing damping in a structure are numerous but can for example include opening and closing of micro cracks in concrete, friction between particles in soil or friction between different structural elements or between structural and non-structural elements. Identifying and mathematically describing each of these

mechanisms seems next to impossible, why a highly idealized representation is used when describing the damping of a structural system. A way of doing so is to let the energy dissipated in all mechanisms be represented by a damping coefficient of a linear viscous damper, called a dashpot. A more thorough description of the damping used in the models of this thesis will be given in section 2.3.

2.3 Soil material models

Modeling of soil is a complex subject due to soil being a non-linear material, which is described by Figure 2.2. Even under the assumption of small strains, when a linear elastic material model may be used, the material properties must be properly estimated. There are several in-situ methods known by geotechnical engineers for making these estimations, some of which are described by Gazetas (1991).

What material model that can be used is highly dependent on the level of strain in the soil. The range of application of different material models is illustrated in Figure 2.3. For the smallest strains, less than 10^{-5}, elastic soil models may be used. This is the strains at which the maximum tangent modulus G_0 in Figure 2.2 may be used in the material model. When the strains are increased, plastic deformations occur and the shear modulus decrease non-linearly. The plastic behavior also leads to an increase in damping due to higher energy dissipation.

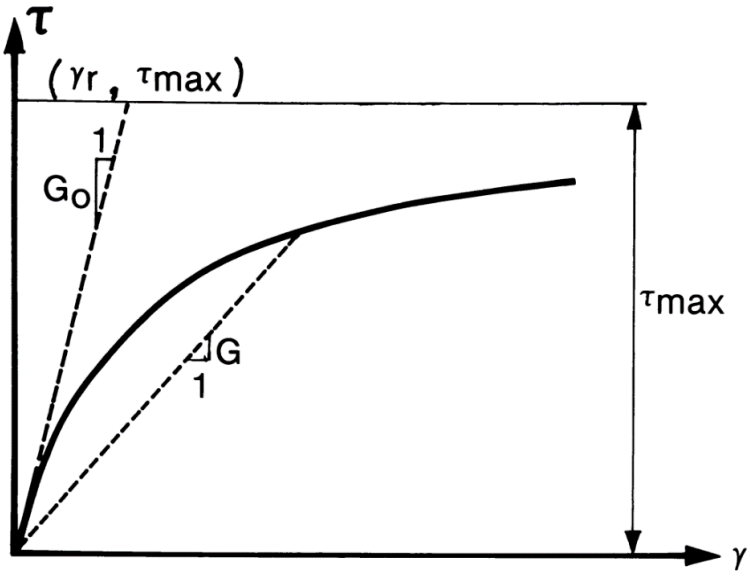

Figure 2.2: The non-linear variation of the shear moduli with strain. τ and γ is the shear stress and strain, G is the secant modulus and G_0 is the maximum tangent modulus, valid for small strains. From (SGI-i1, 2008).

According to Ishihara (1996), for medium strains in the order of 10^{-3} and 10^{-4} the soil can be analyzed with an equivalent linear method and a visco-elastic material model can be used, see Figure 2.3. This model has a reasonable degree of accuracy where the stress-strain relation is assumed linear, and the energy dissipated by the cyclically loaded soil constitutes the damping. For strains less than 10^{-4}, the soil material behavior can be considered as nearly linearly elastic, and either the linearly elastic, visco-elastic or the so called hysteretic material models may be used. This assumption has been made when creating the FE-models in this thesis.

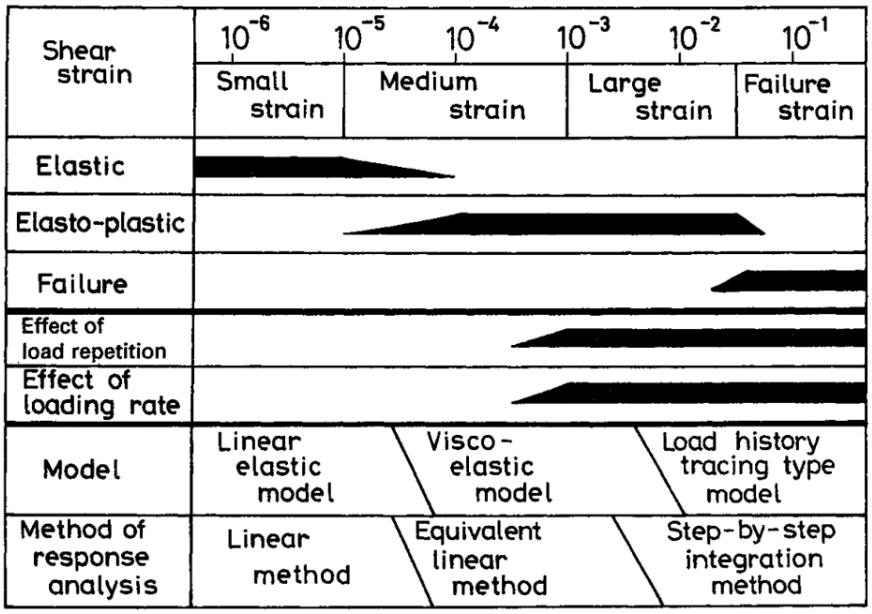

Figure 2.3: Material behavior of soils at different magnitudes of shear strain. The figure indicates the span of shear strain in which a visco-elastic model can be used. From (Ishihara, 1996).

The most widespread model for linear viscoelasticity is to represent the damping as a linear spring and a viscous dashpot. This model is called the rate-dependent Kelvin solid and can be seen in Figure 2.5.

Most materials, including soil and concrete, possess frequency and strain rate-independent damping properties. For such materials, use of a modified version of the Kelvin solid called the rate-independent Kelvin solid is widely used. The damping in this material model is in geotechnical literature referred to as hysteretic damping, and structural damping in the field of structural dynamics. To derive the equations for the rate-independent Kelvin solid, one must start with understanding the theory behind visco-elasticity and the rate-dependent Kelvin solid. The expressions following in this section are derived from Ishihara (1996).

2.3.1 General expression of the cyclic stress-strain relationship

A sinusoidal alternating shear stress can be expressed as:

$$\tau = \tau_a sin\omega t, \tag{2.15}$$

and the resulting shear strain as:

$$\gamma = \gamma_a \sin(\omega t - \delta), \tag{2.16}$$

where τ_a and γ_a is the amplitudes, t is the time, ω the angular frequency and δ is the angle of phase difference giving a time lag in strain response to the application of stress. Introducing complex denotation gives:

$$\bar{\tau} = \tau_a e^{i\omega t}, \qquad \bar{\gamma} = \gamma_a e^{i(\omega t - \delta)} \tag{2.17}$$

The strain versus stress response

$$\frac{\bar{\gamma}}{\bar{\tau}} = \frac{\tau_a}{\gamma_a} e^{i\delta} = \frac{\tau_a}{\gamma_a}(\cos\delta + i\sin\delta) \tag{2.18}$$

can be written as:

$$\frac{\bar{\gamma}}{\bar{\tau}} = \mu + i\mu' = \mu^* \tag{2.19}$$

by putting

$$\mu = \frac{\tau_a}{\gamma_a}\cos\delta, \qquad \mu' = \frac{\tau_a}{\gamma_a}\sin\delta \tag{2.20}$$

where μ is the elastic modulus indicating the immediate response and μ' is the loss modulus representing the energy dissipating properties of the viscoelastic material. μ^* is called the complex modulus, and from equation (2.19) it is shown that the absolute value of the complex modulus indicates the dynamic shear modulus of the material so that:

$$|\mu^*| = \frac{\gamma}{\bar{\tau}} = G_{dyn} \tag{2.21}$$

Equation (2.20) can also be rewritten as

$$\tan\delta = \frac{\mu'}{\bar{\mu}} = \eta \tag{2.22}$$

Here, η is called the loss coefficient, indicating the energy loss in the material. The loss coefficient is related to the damping ratio of the material according to

$$\eta = 2\xi \tag{2.23}$$

where ξ is the damping ratio. The loss coefficient η is also related to the ratio of energy loss per hysteresis cycle, ΔW, and maximum stored energy, W, through:

$$\eta = \frac{1}{2\pi}\frac{\Delta W}{W} \tag{2.24}$$

In Figure 2.4, a hysteresis stress-strain loop is presented. It is derived from the stress-strain relation of equations (2.15) and (2.16), by eliminating the term ωt, divide the shear stress into two components, τ_1 and τ_2 and rearranging the equation on elliptic form. Each loading cycle represents one loop on the ellipse, and the area created by the loop represents the loss of energy in each loading cycle.

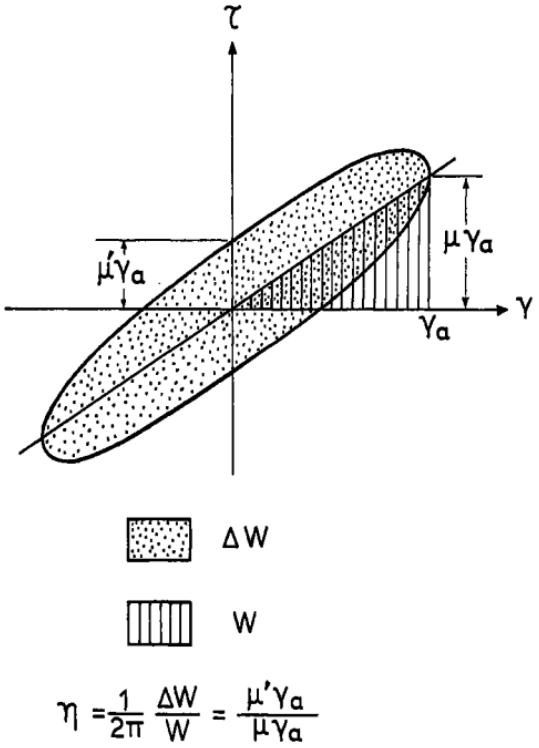

Figure 2.4: The hysteretic stress-strain curve of the linear visco-elastic model. From Ishihara (1996).

2.3.2 Rate-dependent Kelvin solid

As earlier mentioned, the simplest and most widely used material model is the one with a spring and a viscous dashpot connected in parallel, called the rate-dependent Kelvin solid and presented in Figure 2.5. The rate-dependency stems from the dashpot which is velocity dependent and thereby gives more damping on higher frequencies. In this model, the strain is the same for the elements, while the stress τ is divided into one part for the spring, τ_1 and one part for the dashpot, τ_2. Denoting the spring constant G and the dashpot constant G', the total stress becomes:

$$\tau = \tau_1 + \tau_2 = G\gamma + G'\frac{d\gamma}{dt} \tag{2.25}$$

If the complex expressions for the stress and strain in equation (2.17) is introduced for τ and γ, equation (2.25) becomes:

$$\tau_a e^{i\delta} = (G + i\omega G')\gamma_a \,, \tag{2.26}$$

which with reference to equation (2.20) can be rewritten as:

$$\mu + i\mu' = G + i\omega G' \tag{2.27}$$

Equation (2.27) indicates that

$$\mu = G \,, \quad \mu' = \omega G' \,, \quad \eta = \tan\delta = \frac{\omega G'}{G} \tag{2.28}$$

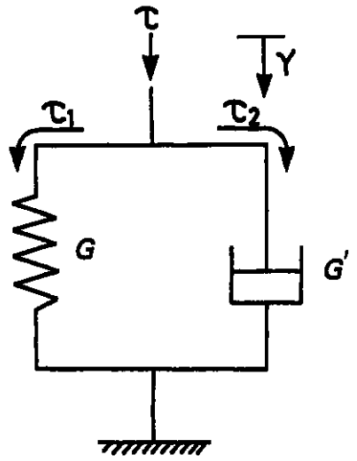

Figure 2.5: The rate-dependent Kelvin solid. From Ishihara (1996).

2.3.3 Rate-independent Kelvin solid

Soil is characterized by not having an increase of damping from increased time rate of strain. A method for reflecting the behavior of soils to a good degree of accuracy is to use a rate-independent dashpot and incorporate in the Kelvin solid. The rate-independent Kelvin solid is written as:

$$\tau = (G + iG'_0)\gamma \tag{2.29}$$

where G'_0 is the dashpot constant. The imaginary term iG'_0 does not have a physical interpretation, but is necessary to represent a phase lag which is characteristic for damping properties of soil. Following the same procedure as for the rate-dependent Kelvin solid, the complex version of the stress can be written:

$$\tau_a e^{i\delta} = (G + iG'_0)\gamma_a \tag{2.30}$$

and the elastic modulus μ and the loss modulus μ' can be derived as:

$$\mu = G \,, \quad \mu' = G'_0 \,, \quad \eta = \tan\delta = \frac{G'_0}{G} \tag{2.31}$$

In equations (2.29) - (2.31), the ω term has been cancelled out and all moduli take constant values, making the model rate-independent. Using equation (2.31), one can rewrite the complex modulus μ^* (equation (2.19)) as:

$$\bar{G} = (1 + i\eta)G \tag{2.32}$$

Equation (2.32) can be expressed in terms of Young's modulus and damping ratio as:

$$\bar{E} = (1 + i2\xi)E \tag{2.33}$$

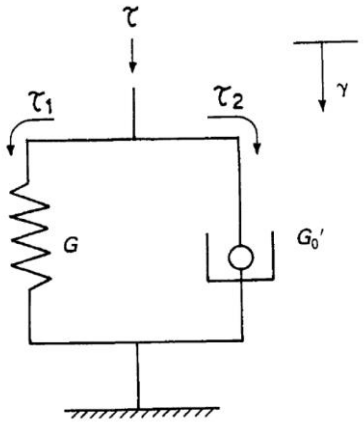

Figure 2.6: The Rate-independent Kelvin solid. The dashpot is here independent on frequency. From Ishihara (1996).

2.3.4 Shear modulus

According to Hardin and Drnevich (1972), the most important factors to determine the damping and stiffness of all types of soils are shear strain amplitude, effective stress level and void ratio, and over consolidation ratio (OCR) and plasticity index for clays specifically.

The shear modulus can either be expressed as the secant or the tangent of the shear stress-strain relationship of a material as:

$$G = \frac{\Delta\tau}{\Delta\gamma} \qquad \text{(secant modulus)} \tag{2.34}$$

$$G = \frac{\delta\tau}{\delta\gamma} \qquad \text{(tangent modulus)} \tag{2.35}$$

where τ is the shear stress and γ is the shear strain.

As mentioned in the introduction to section 2.3, the visco-elastic model uses a linear stress-strain relationship. In the linear region, the tangent and secant shear moduli have the same values and are called the maximum shear moduli or the initial static

shear moduli. The maximum shear modulus, G_0, can be expressed empirically as a function of the form:

$$G_0 = Cf_1(e)f_2(OCR)(\sigma'_0)^n \tag{2.36}$$

where e is the void ratio, OCR is the over consolidation ratio, σ'_0 is the mean effective stress, and n, C, f_1 and f_2 are material specific constants and functions. A formula on this form is adapted in the methods chapter of this report.

The mean effective stress is calculated through the expression

$$\sigma'_0 = \frac{1 + 2K_0}{3}\sigma'_v \tag{2.37}$$

where σ'_v is the effective vertical stress component calculated as the weight density times the depth minus the pore water pressure as:

$$\sigma'_v = \sigma_v - u \tag{2.38}$$

For an embankment, the pore water pressure is typically zero as it is situated above the ground water level. K_0 is the at rest earth pressure coefficient which depends on the drained frictional angle ϕ' and can for frictional soil be expressed as (Zhang, Shamoto, & Tokimatsu, 1998):

$$K_0 = 1 - \sin\phi' \tag{2.39}$$

2.4 Impedance functions

Impedance is a complex valued measure of how much a structure resist motion when subjected to a harmonic force. The resistance to motion of a soil-structure interface can be represented by impedance functions that can be represented by dynamic springs (real part) and dashpot coefficients (imaginary part). The damping consists of both material damping due to energy losses from hysteretic action of the soil, and of radiation damping due to waves carrying energy out of the system.

The formulas following in this section can be generalized to harmonic forces and moments in all directions, but the derivation, taken from Gazetas (1991), is given for a vertical force only.

In Figure 2.7, the concept of soil-structure interaction and interface impedance is presented. In the figure, a rigid foundation block of mass m, underlain by linearly deforming soil layers, is subjected to a vertical harmonic force $F_z(t)$. The foundation is affected by the harmonic force, the inertia force and the soil reaction resultant. The soil reaction resultant consists of both damping and stiffness. Vibrations from the

harmonic force $F_z(t)$ will induce wave motions in the soil. In this way, energy is transferred away from the structure in the soil, which damps the vibrations in the structure.

The foundation block is symmetric around the z-axis and hence it will only have vertical harmonic displacements $u_z(t)$. In the figure, the motion of the foundation block and that of the soil is separated through a free-body cut. Newton's second law gives

$$F_z(t) - P_z(t) = m\ddot{u}_z(t) \tag{2.40}$$

for the mass, or with complex denotation:

$$\bar{F}_z - \bar{P}_z = -\omega^2 m\bar{u}_z \tag{2.41}$$

For the foundation, the equivalent equation of equilibrium can be summarized as:

$$\bar{P}_z = \bar{\Re}_z \bar{u}_z\,, \tag{2.42}$$

where $\bar{\Re}_z$ is the dynamic vertical impedance determined for this specific soil-layer profile. If equation (2.42) is rewritten as

$$\bar{\Re}_z = \frac{\bar{P}_z}{\bar{u}_z}\,, \tag{2.43}$$

it is clear that the impedance is the force-over-displacement ratio, and thus a form of ground stiffness. The complex modulus in equation (2.32) is proportional to the complex ground stiffness, which then can be written as

$$\bar{k}_z = k(1 + i\eta) \tag{2.44}$$

for the rate-independent material model used in this thesis. Here, k and η are functions of the angular frequency ω. If we let the resisting force from the static stiffness and damping of the soil be expressed as $\bar{f}_{s,z} = k(1 + i\eta)\bar{u}_z = \bar{k}_z\bar{u}_z$, then the vertical equilibrium of the soil-foundation interface becomes:

$$\bar{P}_z = \bar{k}_z\bar{u}_z - \omega^2 m\bar{u}_z \tag{2.45}$$

Combined with equation (2.42) the expression for the impedance becomes:

$$\begin{gathered} \bar{P}_z = \bar{\Re}_z\bar{u}_z = \bar{k}_z\bar{u}_z - \omega^2 m\bar{u}_z \\ => \bar{\Re}_z = \bar{k}_z - \omega^2 m = k(1 + i\eta) - \omega^2 m \end{gathered} \tag{2.46}$$

Generally, the impedance can be expressed as:

$$\bar{\Re}_z = \bar{K}_z + i\omega C_z, \tag{2.47}$$

where the real part $\bar{K}_z$ is the dynamic stiffness, which reflects the stiffness and inertia of the supporting soil, and the imaginary part ωC_z is the angular frequency times the "dashpot coefficient" reflecting radiation and soil-material damping.

A combination of equations (2.41), (2.42) and (2.44) gives the complex displacement

$$\bar{u}_z = \frac{\bar{F}_z}{k(1+i\eta) - \omega^2 m} \tag{2.48}$$

and the amplitude of oscillation for a particular frequency can be obtained as

$$u_z = |\bar{u}_z| = \frac{F_z}{\sqrt{k^2(1+i\eta)^2 + \omega^2 m^2}} \tag{2.49}$$

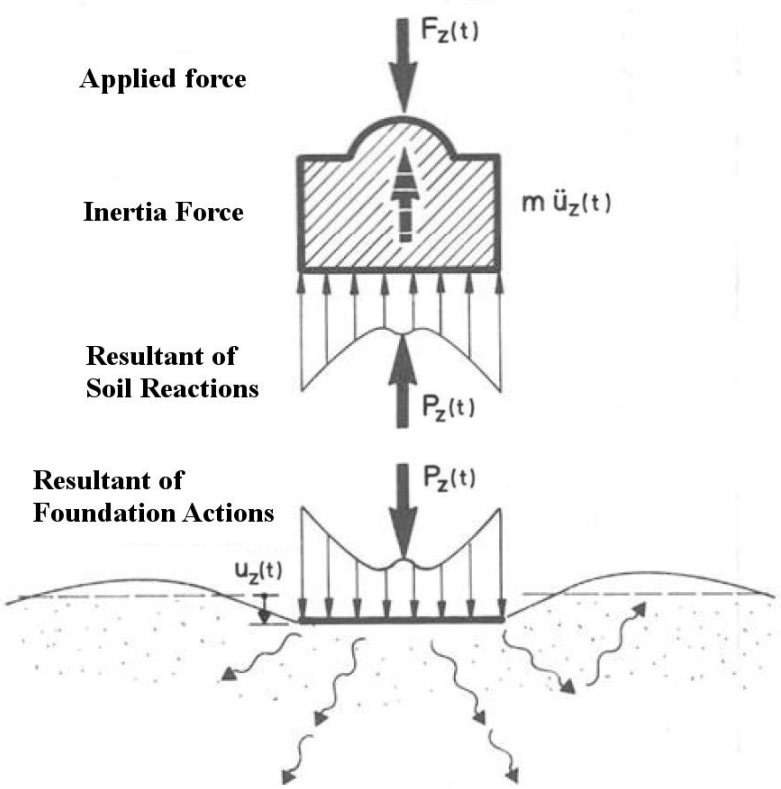

Figure 2.7: Dynamic equilibrium of a vertically oscillating foundation block. From Gazetas (1991).

Equation (2.48) makes it possible to compute the impedance from known stiffness and damping parameters. The formulas derived in this section can, as explained above, be generalized to all directions and rotations.

A way of computing the impedance functions is to first compute the complex frequency-response function (FRF) $\bar{H}_u(\omega)$, called the receptance, which contain the steady state responses of displacements. Again consider the equation of motion for a single d.o.f. system, expressed in equation (2.2). If a harmonic steady state unit load is applied such as $F(t) = 1e^{i\omega t}$, the steady-state response can be expressed as:

$$u(t) = \bar{H}_u(\omega)e^{i\omega t} \tag{2.50}$$

By cancelling the $e^{i\omega t}$ term and inserting the unity load into equation (2.48), the receptance is obtained as:

$$\bar{H}_u(\omega) = \frac{1}{-\omega^2 m + k(1+i\eta)}, \tag{2.51}$$

which is the inverse of the impedance and can thereby also be written as:

$$\bar{H}_u(\omega) = \frac{1}{\bar{\Re}(\omega)} = \frac{1}{\bar{K}(\omega) + i\omega C(\omega)}, \tag{2.52}$$

By first computing the receptance as the steady state response of displacements, one can thus obtain the impedance functions by inverting the receptance. The dynamic stiffness and dynamic damping is thereafter obtained as the real and the imaginary part of the impedance, respectively.

2.5 Wave propagation in elastic solids

A vibrating structure emits waves into the supporting soil. A wave can be defined as a transmission of disturbance from one particle of the medium to the next. There are four major types of waves in elastic solids, all of which are illustrated in Figure 2.8 to Figure 2.10. The primary wave, or P-wave, is the fastest one and has a soil motion in the same direction as the wave propagation. The phase velocity of the primary wave is calculated through (Gazetas, 1991):

$$V_P = \sqrt{\frac{M_C}{\rho}}, \tag{2.53}$$

where M_c is the compression modulus, related to the Young's modulus E as:

$$M_C = \frac{E(1-\nu)}{(1+\nu)(1-2\nu)}, \tag{2.54}$$

with ν being the Poisson's ratio. In shear waves, or S-waves, the particles move perpendicular to the wave direction. The shear wave speed is typically about $0.5V_P$ but may be even lower in, for example, organic soils (Andersen, 2006). This is due to the fact that shear waves only propagate through the soil particles and cannot propagate through water.

The phase velocity of the S-wave is defined as

$$V_S = \sqrt{\frac{G}{\rho}} \tag{2.55}$$

where ρ is the mass density and G is the shear modulus, defined as

$$G = \frac{E}{2(1+\nu)} \tag{2.56}$$

Both P-waves and S-waves are non-dispersive (i.e. not depending on the wavenumber) and can propagate in an unbounded solid. The Rayleigh wave, on the other hand, are a so-called surface wave and can only propagate in half-spaces, defined as a homogeneous space which extends only under a plane. The Rayleigh wave may be compared to the surface waves of water, and has elliptical soil motions. Rayleigh waves have a lower energy attenuation than other waves, and is thus dominant on large distances from the source. The phase velocity of the Rayleigh wave is typically around $V_R = 0.9V_S$.

The wavelength λ at a specific wave speed and frequency is calculated through:

$$\lambda_i = \frac{V_i}{f} \tag{2.57}$$

where V_i is the speed of any of the above described waves and f is the frequency of vibration.

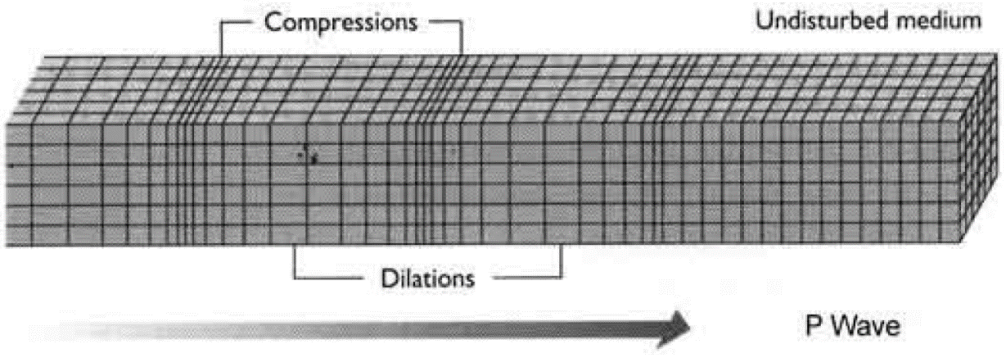

Figure 2.8: The P-wave, also called the primary, dilatational, or compression wave

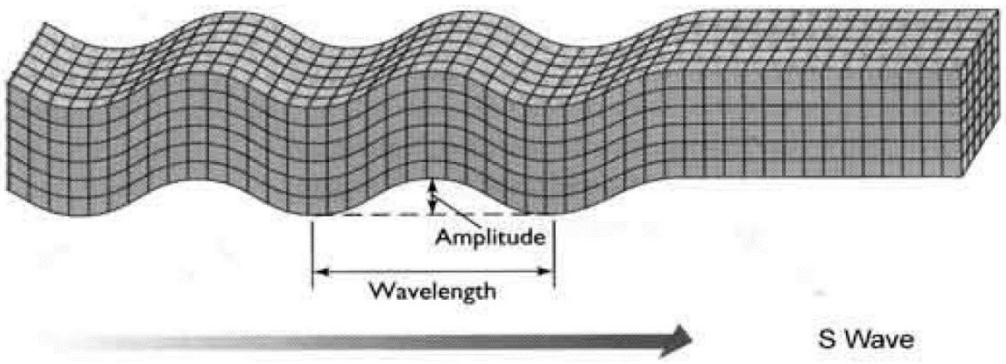

Figure 2.9: The S-wave, also called the shear wave or secondary wave.

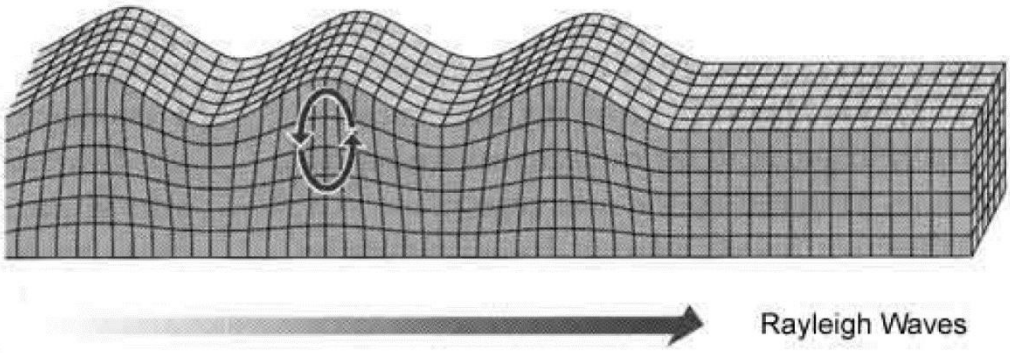

Figure 2.10: The Rayleigh wave.

2.5.1 Radiating boundary

During a dynamic analysis, a wave propagating against a boundary will reflect into the discretized domain, producing so-called spurious waves (Kausel, 2005). Spurious waves occur not only at boundaries, but in all interfaces where the stiffness or damping is changed. When travelling through layers of different stiffness, a fraction of the wave will be reflected with a small change of angle compared to the original direction of the wave.

There are several methods of dealing with this problem and thereby fulfill this part of the so-called radiation condition, some of which are the *plane wave approximation, perfectly matched layers,* the *absorbing region* and the *standard viscous boundary.* In this thesis, the standard viscous boundary is used as it is implemented in ABAQUS and has shown good results in previous studies (Ülker-Kaustell, 2009). The standard viscous boundary was developed by Lysmer and Kuhlemeyer (1969) to replace an infinite continuous system with a finite one, by implementing a boundary condition

simulating the energy absorption of the infinite medium. The boundary condition was made up by a set of viscous dampers that absorbed the energy of the waves entering the boundary.

The method works close to perfect for primary and secondary waves entering the boundary at angles greater than 30°, but less satisfactory for smaller angles and for Rayleigh waves. These two drawbacks of the method can be circumvented by choosing an appropriate geometry and size of the model. To avoid too acute angles of the incoming waves, it is suggested to model either a half-sphere for deep soil-models, or a circular plate for shallow soil-stratum near bedrock. In the circular plate, the waves will either enter the infinite boundary in a near right angle, or reflect against the bottom of the model, as they would when entering the bedrock. In the half-sphere, the waves will enter the boundary at a near right angle at any location in the model, and behave like in a very deep soil deposit.

Because it is a surface wave, the Rayleigh wave cannot be mitigated by the standard viscous boundary with the same efficiency as primary waves or shear waves that propagate in unbounded solids. The solution to the problem with Rayleigh wave reflections is to choose a sufficiently large computational domain. It is important to mention that, even with sufficient length, not all waves are completely mitigated and the boundary cannot be considered silent, but instead be considered as quiet.

2.6 Fourier transform

The Fourier transform is used to transform data from the time domain to the frequency domain. The interface between the time and frequency domain is shown and explained in Figure 2.11, from where it can be read that the frequency domain represent an extraction of the frequencies of the signals.

The basis for the Fourier transform is the Fourier series, with which one can express arbitrary periodic functions as series of trigonometric functions. The Fourier series of a periodic function can be expressed:

$$f(t) = a_0 + \sum_{j=1}^{\infty} a_j \cos j\omega_0 t + \sum_{j=1}^{\infty} b_j \sin j\omega_0 t \tag{2.58}$$

where

$$a_0 = \frac{1}{T_0}\int_0^{T_0} f(t)dt\,, \tag{2.59}$$

$$a_j = \frac{2}{T_0}\int_0^{T_0} f(t)\cos j\omega_0 t\, dt \qquad j = 1, 2, 3, \ldots \tag{2.60}$$

$$b_j = \frac{2}{T_0}\int_0^{T_0} f(t)\sin j\omega_0 t\, dt \qquad j = 1, 2, 3, \ldots \tag{2.61}$$

The fundamental harmonic frequency ω_0 is expressed:

$$\omega_0 = \frac{2\pi}{T_0} \tag{2.62}$$

When the excitation $f(t)$ is not periodic, it can instead be represented by the Fourier integral, here expressed with complex denotation:

$$f(t) = \frac{1}{2\pi}\int_{-\infty}^{\infty} F(\omega)e^{i\omega t}d\omega \tag{2.63}$$

where

$$F(\omega) = \int_{-\infty}^{\infty} f(t)e^{-i\omega t}dt \tag{2.64}$$

Equation (2.63) is also referred to as the *inverse Fourier transform* of the frequency function $F(\omega)$, and equation (2.64) as the *Fourier transform* of the time function $f(t)$, also known as the *direct Fourier transform*.

The response to an arbitrary excitation of a linear system can be determined by combining the responses to individual harmonic excitation terms in the Fourier integral given in equation (2.63). The response of the system to the excitation $P(\omega)e^{i\omega t}$ is given as:

$$\mathrm{U}(\omega) = \mathrm{H}(\omega)\mathrm{P}(\omega)e^{i\omega t} \tag{2.65}$$

where $\mathrm{H}(\omega)$ is a complex frequency-response function. The time domain response is given by superposing the responses to all harmonic terms in equation (2.63), as in equation (2.66).

$$u(t) = \frac{1}{2\pi}\int_{-\infty}^{\infty} \mathrm{U}(\omega)e^{i\omega t}d\omega \tag{2.66}$$

This is known as the frequency-domain method for analysis of structural response to arbitrary excitation, and requires that both the Fourier transform of $f(t)$ and the inverse Fourier transform of $U(\omega)$ are determined. Except for simple systems with excitations described by simple, continuous functions, analytical evaluation of these direct and inverse Fourier transforms is not possible. In FE modeling and signal analysis, values are sampled digitally and the complex frequency response is described numerically. Hence, analytical evaluation of the integrals in equations (2.64) and (2.66) is not possible and an adaptation for discrete sampling is needed. A method for

numerical evaluation is the *discrete Fourier transform* (DFT), which requires truncating the Fourier integrals over infinite range to a finite range. The discrete Fourier transform is given by:

$$P_j(\omega) = \frac{1}{N}\sum_{n=0}^{N-1} p_n(t) e^{-i(2\pi nj/N)} \tag{2.67}$$

And the inverse DFT is given by:

$$p_n(\mathrm{t}) = \sum_{j=0}^{N-1} P_j e^{i(2\pi nj/N)} \tag{2.68}$$

where p_n is an array describing the discretized forcing function $p(t)$ as a superposition of N harmonic functions.

Practical use of the computation of the Fourier transform was made possible after Cooley and Tukey (1965) published an algorithm called the *fast Fourier transform* (FFT). The FFT is a highly efficient and accurate algorithm for calculating the DFT and inverse DFT, without expensive computational cost.

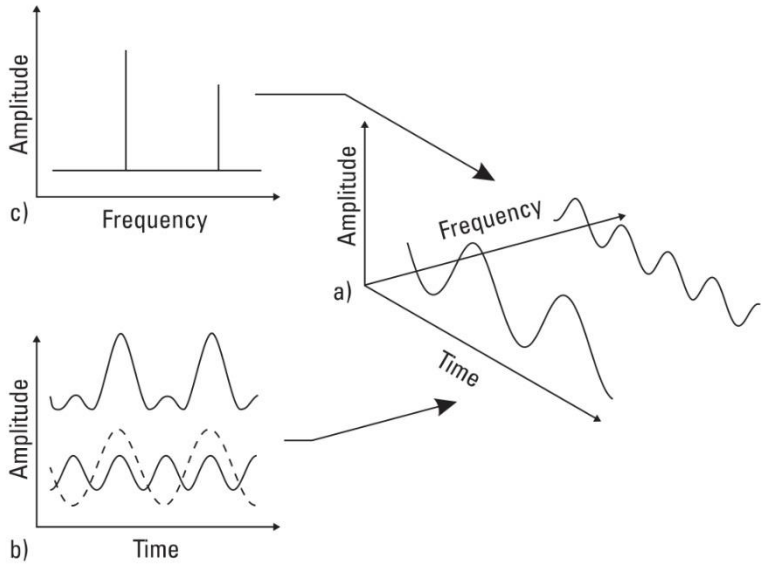

Figure 2.11: The relationship between the time and frequency domains. a) Three dimensional coordinates showing amplitude, frequency and time. b) Time domain. c) Frequency domain. From Hewlett-Packard (2000).

Chapter 3

Modeling and method of analysis

To analyze how the soil-structure interaction can affect the dynamic analysis of a railway bridge, a solid finite element bridge-embankment-model was made to obtain impedance functions. In this thesis, only a part of the portal frame bridge has been modeled, namely the bridge wall and the wing walls connected to the bridge wall. This was decided in order to reduce the computational capacity needed and to reduce the risk of errors due to details in the bridge model. By modeling the whole bridge, the bridge's own vibration behavior would be taken into account, which would disturb the results of the analysis. The loading of the embankment soil need to be controlled, and should be applied as unity loads either directly to the soil or to the bridge wall in contact with the soil.

In Figure 3.1, the methodology of obtaining impedance functions is described through a flow chart. To obtain the impedance functions, the FE software ABAQUS together with mostly Python, but also Matlab was used. The steps in the flow chart will be described more thoroughly in this chapter.

A comparison was made between two types of models of different size. The smaller model consisted of a bridge wall and embankment only, and the bigger model consisted of the small model plus a circular soil plate with the same radius as the length of the embankment, plus a foundation that the bridge wall rested on. The choice to develop two different models was made for several reasons, among which the most important was to be able to compare results and determine if the differences in results were relevant in contrast to the extra computational costs related to the bigger model. The smaller model was also used in time saving purpose during the convergence tests, under the assumption that if a parameter converges in the small model it will also do so in the bigger model.

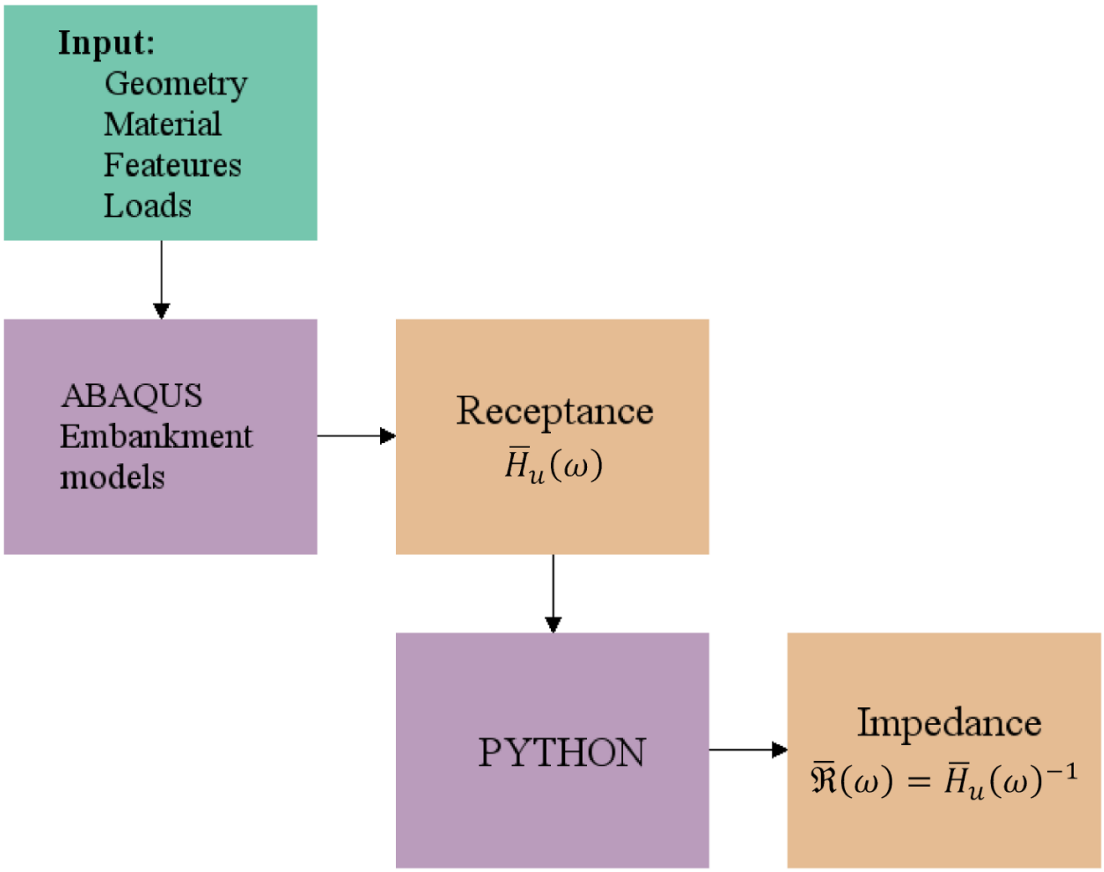

Figure 3.1: Flow chart describing the procedure of obtaining impedance functions.

3.1 Modeling procedure in ABAQUS

In order to make the bridge geometry as relevant as possible, the dimensions of an existing bridge was used in the bridge-embankment-models. The bridge is situated in Dösjebro, 5 km outside of Lund and is shown in Figure 1.2.

During the work with this thesis, the finite element-software BRIGADE Plus has been used. BRIGADE Plus is a software package for structural analysis and design of bridges and civil structures. BRIGADE uses the kernel of ABAQUS but supplies tools for performing dynamic analyses according to Eurocode. As the tools specific for Brigade were not used in this thesis, the methods used are applicable even using ABAQUS. To avoid confusion, hereafter the software used will be denoted ABAQUS.

The models were first developed in the ABAQUS graphical user interface (GUI) and then reworked in the Python script-files to make all geometries and material properties variable. This made the parameter test easier to perform and will ease the recreation for those interested in using the model in future research.

3.1.1 Geometry

Some dimensions of the embankment model were varied in a parameter study and some were set through convergence tests and then kept constant. Presented in this section is only the methods for deciding the default dimensions given to the embankments models in the convergence study. The general geometry and features of one of the bridge-embankment models is shown in Figure 3.2, and the features of the big model is shown in Figure 3.3.

The embankment that is placed on the ground soil layer in the big model has the same dimensions as the final geometry of the embankment, which depend on the results from the convergence study. In the following sections, the geometry and features of the models as well as the methods used to derive the impedance functions, will be given a more thorough description.

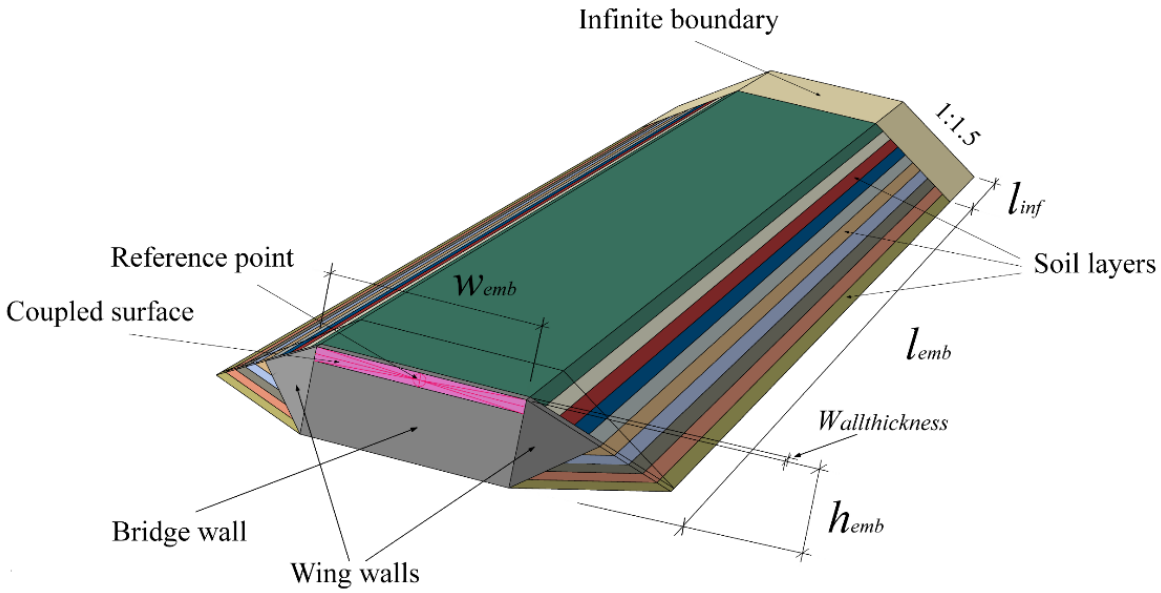

Figure 3.2: Geometry and features of one of the small models used in the parameter study.

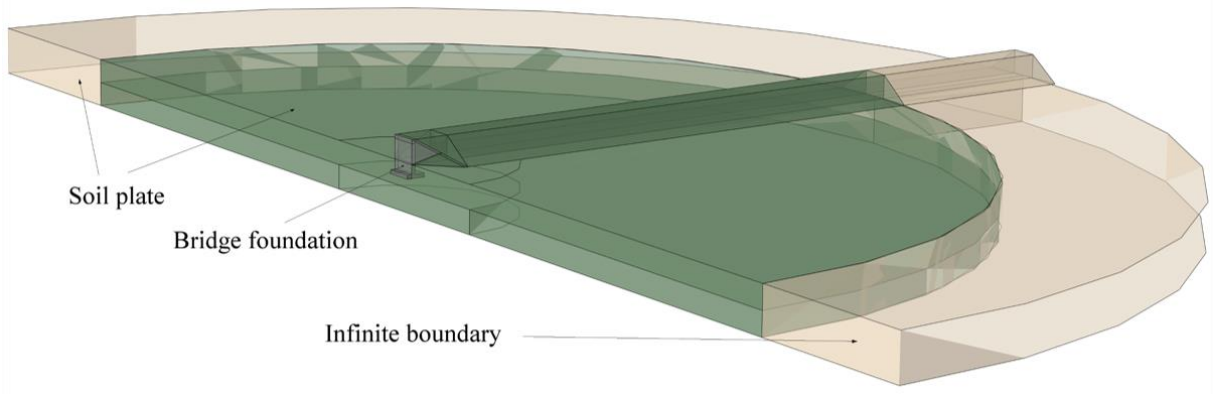

Figure 3.3: The big model, cut in half and slightly translucent. The features of the embankment are the same as for the small models, only with a foundation embedded in the soil plate.

Length of embankment

The length of the calculative domain, meaning the length of the embankment up to where the infinite boundary starts (l_{emb} in Figure 3.2), depend on the longest expected wave length. The default length of the embankment (and thereby also the radius of the soil plate) was set to a fourth of the longest wavelength. The longest wavelength occur, according to equation (2.57), from the highest wave speed at the lowest frequency.

Height and width of embankment and bridge wall

Depending on if the bridge is one- or two-tracked, the width will be different, either around 6 meters or around 12 meters. In this thesis, both 6 and 12 meter wide embankment models were analyzed in the parameter study.

A few alternations of the element mesh had to be done to be able to create the HEX-model (see section 3.1.7) with a 6 meters wide embankment. This was due to an unknown error occurring when running a MATLAB script for creating the infinite boundary. As it turned out from the convergence study (see section 3.2.2), the meshing technique plays a rather insignificant role as long as the element size is kept constant. Therefore, the models were still able to be compared to each other even with the use of slightly different meshing techniques.

The height of the bridge depends on what is intended to pass under it. A railway bridge overpassing a railway track needs typically to be higher than one overpassing a road. To stick to the aim to represent a real bridge, the height of the portal frame bridge in Dagstorp, mentioned earlier, was chosen, and no comparison between different bridge

heights was made. The height of the embankment was set to the same as the bridge wall, 5 meters.

Inclination of slopes

A usual value for the inclination of embankment slopes of Swedish railways is 1:1.5, so this value was chosen in this study. An idea was to vary the inclination in the parameter study to see its influence on the wave propagation, but this had to stand aside due to lack of time.

Wing walls

The main use of a bridge wall is to resist the soil pressure of the slopes, but the wing wall also have the side effect of increasing the bending moment of the bridge wall. Depending on the type of slopes, the wing walls of a bridge, connected and stretching from the sides of the bridge wall, can have different shapes. In this thesis, two types of bridge walls have been modeled: One without wing walls, and one with wing walls bent in an angle of 45° backwards, as can be seen in Figure 3.2. Another type of wing wall, that was not modeled in this thesis but is worth mentioning, is one that stretch at a right angle from the bridge wall, parallel to the railway tracks. This type would induce higher stiffness of the bridge wall which could be beneficial for the bridge-soil interaction.

Depth of foundation

As mentioned above, only the big models included a bridge foundation. The dimensions of the foundation were based on a typical portal-frame bridge and was not varied throughout the study. The foundation was a shallow slab-foundation consisting of a concrete plate placed about 2 meters below ground level. In real cases the foundation would be casted upon a layer of compressed sand and gravel, but in this thesis the model was simplified so that the soil beneath the foundation had the same properties as the whole circular ground soil plate.

Depth of ground soil plate

The very last analysis performed within this project, was for the model with both embankment, foundation and a circular soil plate beneath. The first idea was to perform the same parameter tests on the big model as on the small, model. However, limited time and computational resources made it necessary to reduce the analysis so that only different depths and values of the soil stiffness were tested. The depths modeled were 5, 10 and 15 meters.

3.1.2 Material properties

As previously mentioned in section 3.1, the geometry of the models were taken from an existing bridge, situated outside of Lund. The material properties, however, was not taken from the geotechnical survey of the same bridge. Most Skåne soils, including the one beneath the bridge in Dösjebro, are massive layers of clay till, over-consolidated from the last ice age. A soil profile more generally found in Sweden, namely moraine, were instead chosen for the soil plate.

As stated in section 2.3, soil can be modeled as a linear, viscoelastic material for small strains. Using the assumption of small strains implies that a maximum shear modulus may be used. In this thesis, two techniques of modeling the stiffness of the soil in the embankment have been used, and been compared in a parameter study. The first technique is to calculate an average maximum shear modulus for the whole embankment.

Constant, average shear modulus

From equations (2.53), (2.54) and (2.56) it is obvious that the Young's modulus and shear modulus of the soil can be calculated from knowing the P-wave speed, mass density and Poisson's ratio. While the latter two are well known parameters, the wave speed can be harder to obtain reliable values for. The main reason for this is that if the soil is saturated, the P-wave will have the velocity of water. The P-wave speed of water is, as can be seen in Figure 3.4, much higher than that of sand and gravel, why for saturated soils, the stiffness gets highly over exaggerated. The S-wave cannot travel through water, only through the soil's skeleton, and will therefore give the same result regardless of the soil being saturated or not, and is thereby a more reliable material property to use for obtaining the soil stiffness. In this thesis, the S-wave speed for sand and gravel has been used to first calculate the Young's modulus through equations (2.55) and (2.56) and then insert in equations (2.53) and (2.54) to obtain the P-wave speed.

In the parameter study, the lower and upper values for the S-wave speed for frictional soils such as sand and gravel were used for obtaining the largest and smallest average shear modulus. In Figure 3.5 it can be seen that the shear wave velocities of frictional soils span from about 150 m/s to 400 m/s, which with equation (2.55) give a maximum average shear moduli, G_0, between 40.5 MPa and 288 MPa.

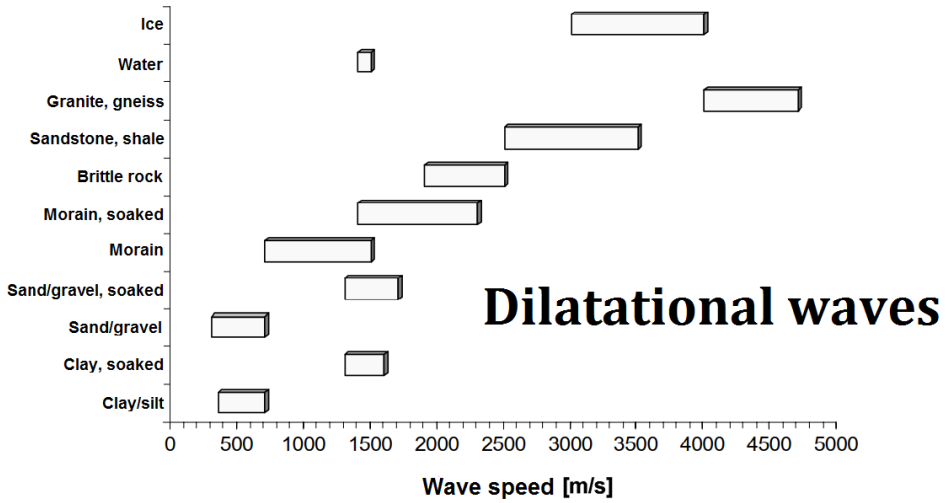

Figure 3.4: P-wave speeds in different mediums. After Bengtsson et al. (2000).

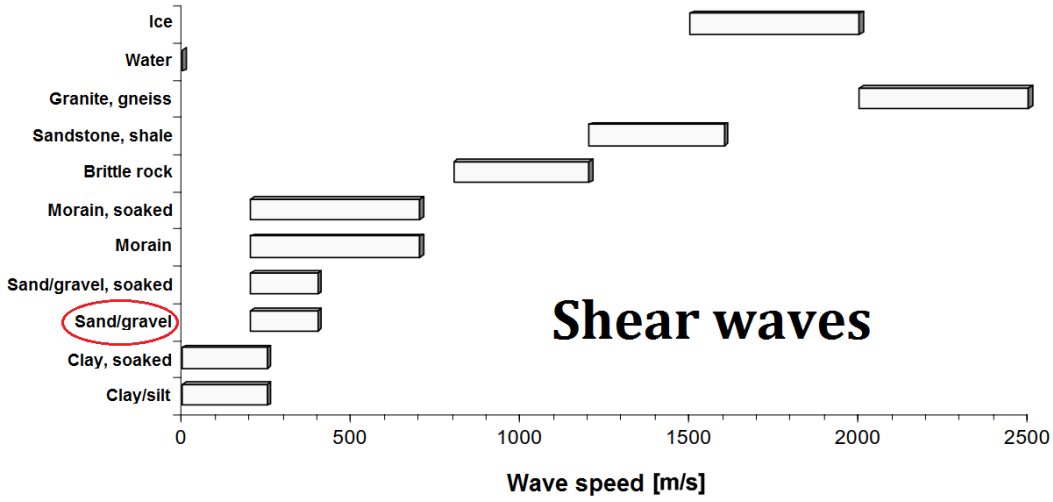

Figure 3.5: Shear wave speeds in different mediums. After Bengtsson et al. (2000).

The second technique for modeling the soil stiffness was to use a shear modulus varying with depth, described below.

Shear modulus varying with depth

A way to empirically describe the shear modulus with depth on the form presented in equation (2.36) is given in SGI-i1 (2008) as:

$$G_0 = \frac{625}{0.3 + 0.7e^2} OCR^k \sqrt{\sigma'_0 \cdot p_a} \tag{3.1}$$

where OCR is the over consolidation ratio, e is the void ratio, p_a the atmospheric pressure set to 100 kPa, σ' the mean effective principal stress and k is a factor

depending on the plasticity index, I_p, ranging from 0 for friction soils to 0.5 for cohesion soils with $I_p > 80$ %.

In the parameter study it is desirable to be able to compare the results with constant, average shear modulus and shear modulus varying with depth. If the formula in equation (3.1) were used, the mean value of the shear modulus in the embankment would differ between the models and a comparison would be rather deceptive. Therefore, a modified formula created by Östlund (2016) was implemented:

$$G_{0,mod} = K_{mod}\sqrt{\sigma'_0} \tag{3.2}$$

Here, the K_{mod} term is chosen as a constant so that the mean value of the shear moduli for a given number of depths become the same as the maximum average shear modulus given in the previous section. The model were divided into 10 layers of equal thickness and each layer were given a shear modulus corresponding to the depth in the middle of the layer. 10 increments were believed to be enough to receive small enough increments in stiffness to avoid spurious waves and fulfill the radiation condition. As it turned out, this assumption were correct (see section 4.1.1).

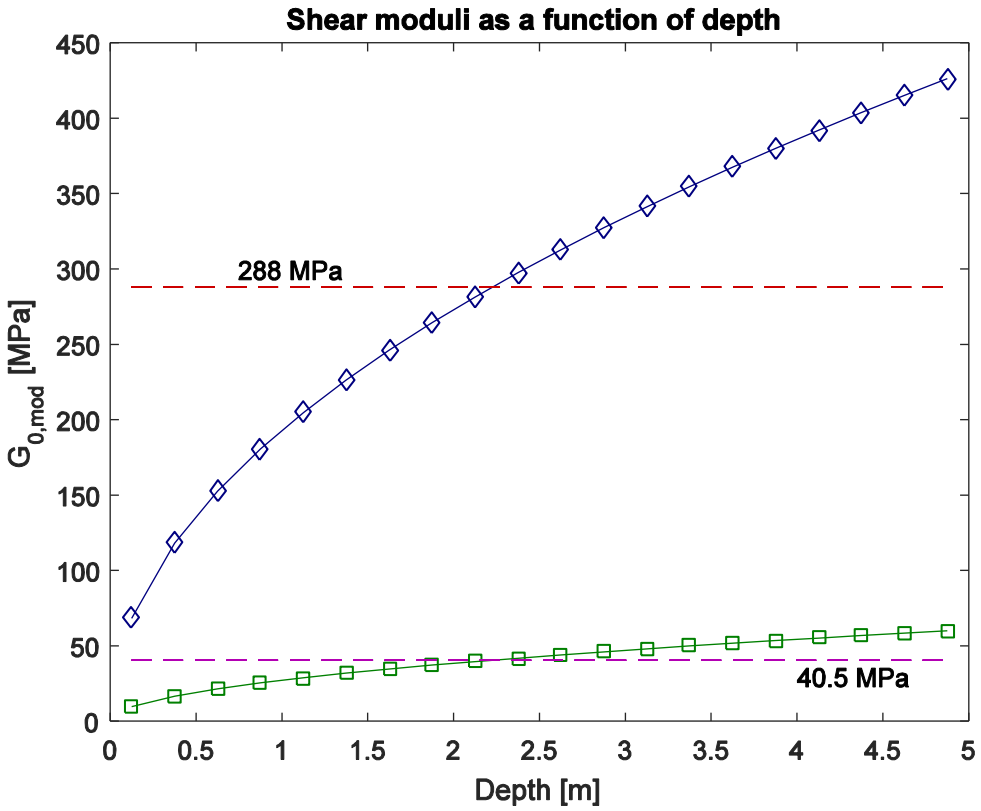

Figure 3.6: Shear modulus as a function of depth. Upper curve: High modulus with mean value of 288 MPa. Lower curve: Low modulus with mean value of 40.5 MPa. Dashed lines are the average shear moduli calculated from the shear wave speeds of 150 and 400 m/s.

Material damping

As described in section 2.3, the damping used in the rate-independent Kelvin model is structural damping. The damping ratio, ξ, is set to 1.5 %, corresponding to a loss factor, η, of 3 %. This is a low value that may affect the results in the way that ripples can occur when plotting the impedance and receptance. The same damping was chosen for both the embankment soil and the ground soil.

Concrete and circular soil plate

The Young's modulus of the concrete was set to 34 GPa, a frequently encountered value for un-cracked concrete. In reality the concrete is less stiff due to small cracks in the bridge and the modulus can have to be more thoroughly investigated for each analysis. The stiffer the concrete is in comparison to the soil, the more evenly the loads applied to the bridge wall will be distributed to the soil. This was why the highest modulus stated above was chosen.

For the circular soil-plate in the big model, the shear modulus was given different constant values, calculated from the shear wave speed as presented above. The values chosen will be presented in section 3.2.4. The damping and mass density of the ground soil were set as the same values as for the embankment soil.

3.1.3 Constraints and boundary conditions

To connect parts with each other, and to get the desired type of interaction between them, different constraints can be used in ABAQUS. The constraints used in the models within this thesis will be described in this section.

TIE constraint

In all models, all parts that were not created through partitions were connected to each other with ABAQUS' TIE constraints, where no sliding or friction were allowed, meaning that the connected nodes have full interaction. For connecting parts of same material, for example the embankment to the soil plate or the bridge wall to the bridge foundation, the TIE constraint should not constitute a very big simplification of the reality. When connecting the bridge wall to the embankment, however, assuming full interaction is a simplification that could affect the results due to friction being ignored. This simplification is necessary primarily for keeping the computational costs down, as allowing friction would demand another material model.

One apprehension when using the TIE-constraint is that it may prevent wave propagation in the embankment. This was proven to not constitute a problem when comparing different models, as will be presented in section 3.2.2.

Coupling constraint

An area of the upper part of the bridge wall, corresponding to the area that would be casted together with the bridge deck in a real bridge, was subjected to a coupling constraint to a reference point (RP). The coupling constraint couples the motion of a collection of nodes on a surface to the motion of the reference node. This allows the application of a point load that affects a whole area.

3.1.4 Loads

The receptance is calculated through equation (2.51), where the numerator, the number 1, is a unity load. A unity load was therefore applied in the model. Six unity loads were created where three was unity forces for the X-, Y- and Z-direction and three was unity moments for bending around each axis. The loads were inserted in the reference point and were thereby coupled to the upper part of the bridge wall. This was to resemble how real loads would influence the bridge wall and emit waves that spread and propagate in the soil.

3.1.5 Boundary conditions

In this section, the boundary conditions used in the models will be described.

Prescribed translations

In both the big and the small models, the translations of the bottom part were prescribed to zero. For the small models, this is equivalent with assuming that the embankment rests on bedrock. This requires that no sliding can occur, which was found reasonable for the comparatively small loads applied to the models. For the big model, the embankment rests on a soil layer of varying thickness, which in its turn rests on bedrock. The outer part of the soil plate and the end of the embankment had so-called infinite boundaries, described next.

Infinite boundary

The technique used for radiation damping, using the standard viscous boundary as described in section 2.5.1, was implemented by using so-called infinite elements in

ABAQUS. The infinite elements are used to discretize an unbounded domain without having to truncate it and thereby fulfill the radiation condition. As previously mentioned, the infinite boundary cannot be considered completely silent but has a huge advantage of reducing the number of elements significantly, and thus giving a reduced computational cost.

The quadratic infinite element that can be viewed in Figure 3.8 is basically a quadratic, 20 node brick element where the outside of the element is removed, resulting in a 12 node brick element with infinite extent. This element is not present in the standard element library of ABAQUS and has to be created separately by changing the topology in the input file. As can be seen in Figure 3.8, the face with node numbers 1-8 is the one that should be connected to the other finite elements. To satisfy this, a MATLAB script was used to change the topology and element names in the ABAQUS input file. The model was then regenerated, now containing the infinite boundary.

Again looking at the elements in Figure 3.8, one can draw the conclusion that the bottom face of the infinite element has the same shape and number of nodes as the faces of the HEX element, but not the TET element, thus making the HEX element compatible and the TET element incompatible with the infinite element. This made it possible to create the infinite part of the HEX-model as a partition of the soil part and assign the sections different element types. In the TET model, the infinite soil instead had to be created as a separate part, and then be tied together with the rest of the embankment using the TIE constraint.

Efficiency of the infinite boundary

In Figure 3.7, the effect of using the infinite boundary is shown. In the figure, the imaginary part of the impedance – corresponding to the dynamic damping and indicating the loss of force and moments in the reference node – is plotted against the frequencies. The dark blue and green lines belong to models with the same elements at the boundary as in the rest of the embankment, i.e. models without an infinite boundary. The purple and orange lines have the infinite elements applied to the embankment boundary.

The ripples that can be seen especially in the blue line, but also at the highest frequencies of the green line, are due to the waves reflecting back into the embankment, resulting in distorted impedance plots. With the infinite boundary, almost no ripples are shown, even for the highest frequencies. The small distortions that still can be seen in the plots with infinite boundary are believed to depend on the Rayleigh waves not being completely mitigated. It can also depend on that the material damping was given

a low value. Less ripples are seen in the plots of the models with the stiffer embankment, even without the infinite boundary. This is because most of the waves have already attenuated when reaching the boundary, due to material damping.

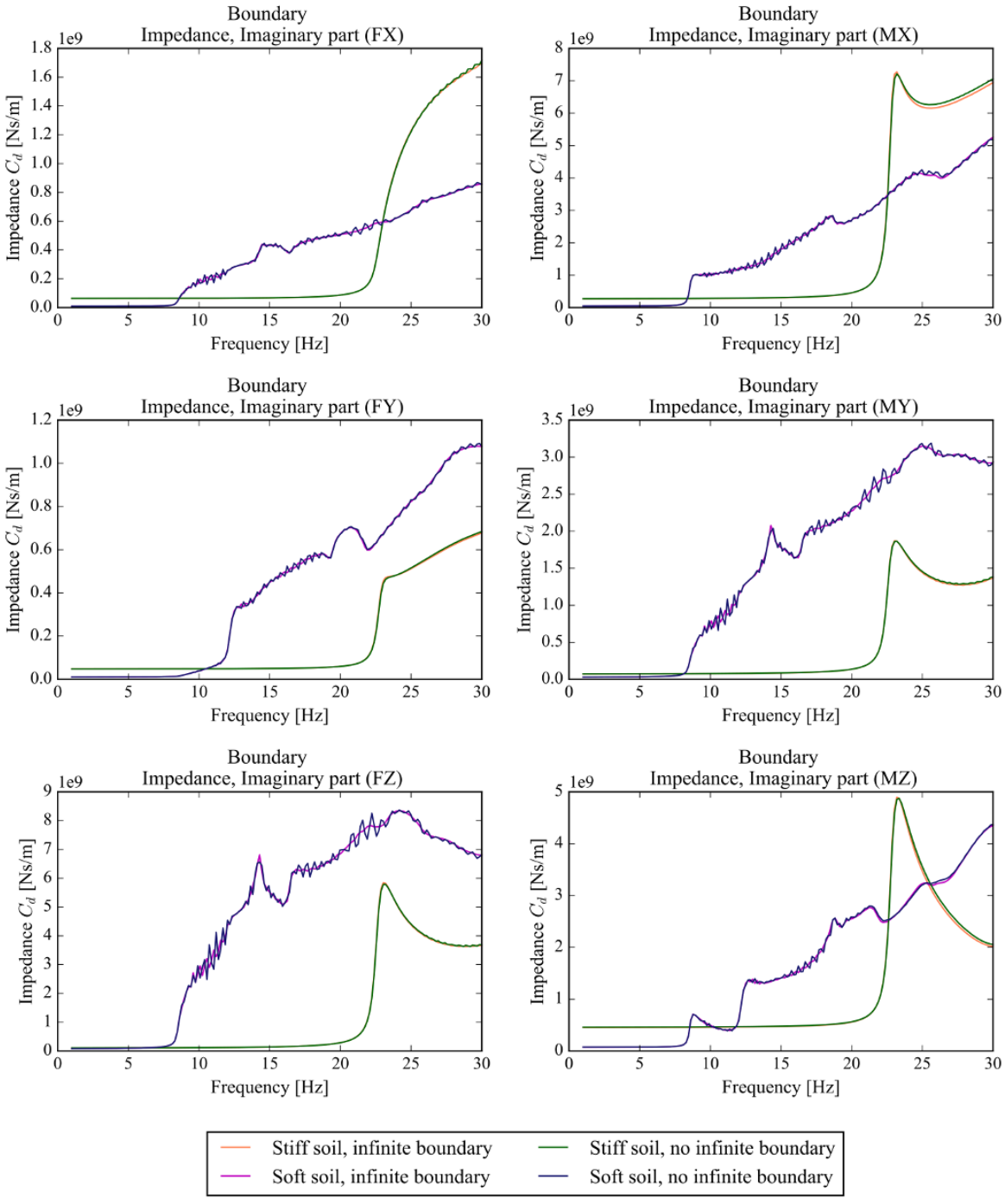

Figure 3.7: Dynamic damping from forces (FX, FY, FZ) and moments (MX, MY, MZ) in the reference node. Models with and without the infinite boundary plotted against each other.

3.1.6 Element size

To fulfill the radiation condition, a small enough mesh of the soil is needed. The shortest wavelength, stemming from the highest frequency of excitation, occurs near the excitation source and is quickly attenuated by the soil material damping. It is therefore possible to reduce computational costs by having a courser mesh density far away from the source, where the shortest wavelengths are attenuated.

The problem related to the element size is called numerical dispersion. Dispersion is a phenomena where waves of different frequencies travel at different speeds. As the S- and P-waves are non-dispersive, they travel at the same speed regardless of the frequency. Numerical dispersion refers to dispersion introduced by the finite mesh size when using, for example, the finite element method or the finite difference method. In FEM, the numerical dispersion occurs due to a mismatch in phase between the exact and the numerical solution. This can be avoided by using a sufficient number of nodes per wavelength.

There are different opinions about how many nodes per wavelength that is sufficient to avoid numerical dispersion. A rule of thumb says that at least eight nodes per wavelength is needed to receive a good enough representation of the wave propagation (Lysmer, 1978). According to Andersen (2006), theory requires that at least four nodes should be used to describe each wave, but that it has been suggested to use more to obtain good results in practice. The same author claims, that in order to achieve satisfactory results, at least 4-5 quadratic elements, or 10-12 linear elements, should be used. This indicates that with use of quadratic elements, fewer nodes per wavelength is sufficient.

The element size of the final models in this thesis was determined from convergence tests that are presented in section 3.2.2.

Apart from the radiation condition, the interface between the concrete and the soil needs to provide a good approximation of the contact stress- and strain distribution. To handle this, smaller elements were assigned to the part closest to the bridge wall.

3.1.7 Mesh technique

In this thesis, different meshing techniques have been used to determine how they affect the results. The soil plate was, due to a geometry making a structured meshing technique complicated to implement, meshed with tetrahedral elements, in ABAQUS called TET elements. TET elements can be used on any geometric shape and are

therefore suitable for both the soil plate and for the wing walls of the bridge. The bridge wall and embankment, however, is of less complicated geometries, and can be meshed with either the WEDGE or the HEX elements of ABAQUS which are wedge shaped and hexahedral (brick) elements, respectively. The different elements used in the models in this thesis, with labels and explanations, are shown in Figure 3.8.

Where possible, reduced integration is used instead of full integration in order to avoid too stiff solutions and to reduce the computational costs. Using quadratic brick elements with reduced integration gives 8 integration points (Gauss points) instead of 27 (Dassault Systèmes, 2012). Out of the elements used in the models in this thesis, only the HEX-elements can be used with reduced integration.

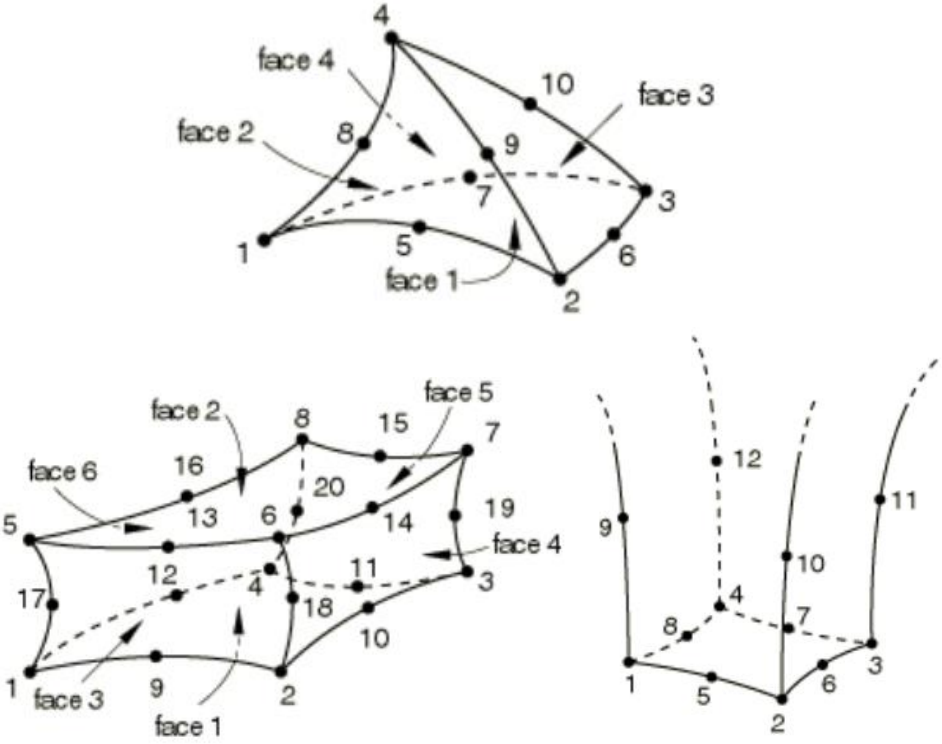

Figure 3.8: Different element shapes used in the ABAQUS model. *Top:* The quadratic tetrahedron (TET) element C3D10 (Continuum 3D 10-node element). *Bottom left:* The quadratic brick (HEX) element C3D20R (Continuum 3D 20-node element with reduced integration). *Bottom right:* The infinite quadratic brick element CIN3D12R (Continuum Infinite 3D 12-node element with reduced integration). From (Dassault Systèmes, 2012).

Apart from the two techniques described in the following paragraphs, tests were carried out on the influence of using a biased mesh. As the shortest waves are believed to attenuate close to the vibration source, a courser mesh might be sufficient a distance away in the model. With a biased mesh, the element size increase with the distance, and the model might be less computationally expensive with preserved accuracy.

A problem that arises when the geometries are complicated in one section of the model but more simple in another, is that it gets impossible to use the same element types throughout the whole model, unless it is meshed with TET elements only. Using only TET elements has the disadvantage that even sections where a structured mesh would be possible have to be meshed with TET elements, and a less structured mesh is obtained. Using different meshing techniques, however, has the disadvantage that many elements, such as the TET and the HEX elements are not compatible with each other due to their shapes. Thus, the model first have to be divided into different parts and meshed separately, and then be connected using the ABAQUS TIE constraint, which allows incompatible regions to be meshed together.

In order to study the influence of different meshing techniques, both of the above described modeling techniques were tested. The division of the model was carried out in two different ways, resulting in two different models which had to be studied separately. Here follows a description of the two models. The soil plate was modeled in the same way, with TET-elements, regardless of the elements used in the embankment.

HEX-model

The HEX-model, illustrated in Figure 3.9, is named from it being divided in one small part containing the bridge wall including wing walls and the embankment up to the end of the wing walls, and one part with the rest of the embankment plus the infinite boundary. The first part is, due to the complicated geometry, meshed with TET elements and the second part with HEX elements, resulting in a model containing mostly HEX elements. The advantage of this model was believed to be that the greater part of the model was given a structured mesh, and thus a lower computational cost.

TET-model

The TET-model is divided in one part with the whole embankment up to the infinite boundary, meshed with TET elements, and the infinite part meshed with HEX elements, resulting in a model with a majority of TET elements, see Figure 3.10. The advantage of this model was believed to be that there were less need for TIE constraints compared to the HEX-model.

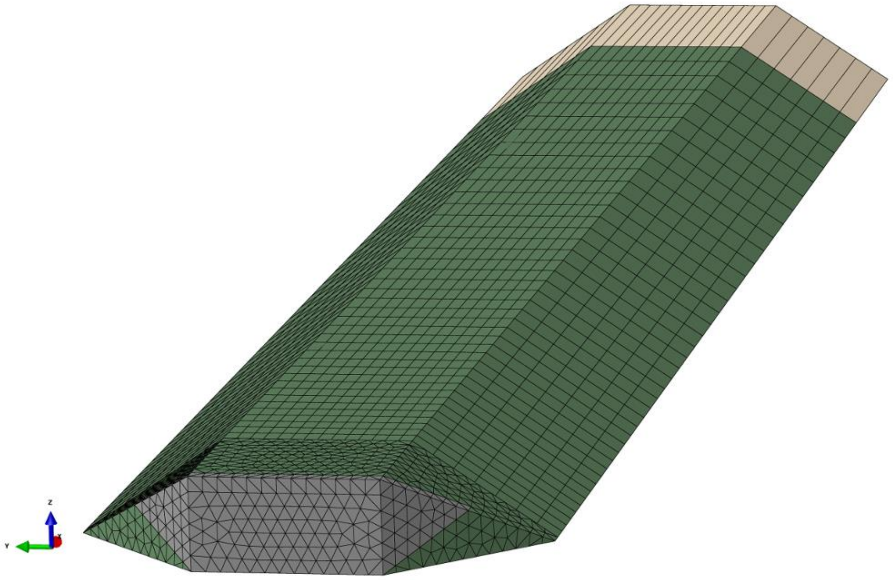

Figure 3.9: The HEX-model, meshed mainly using hexahedral elements. The model is divided in two parts: One with the more complicated geometry of the bridge wall, and one where a structured mesh is possible.

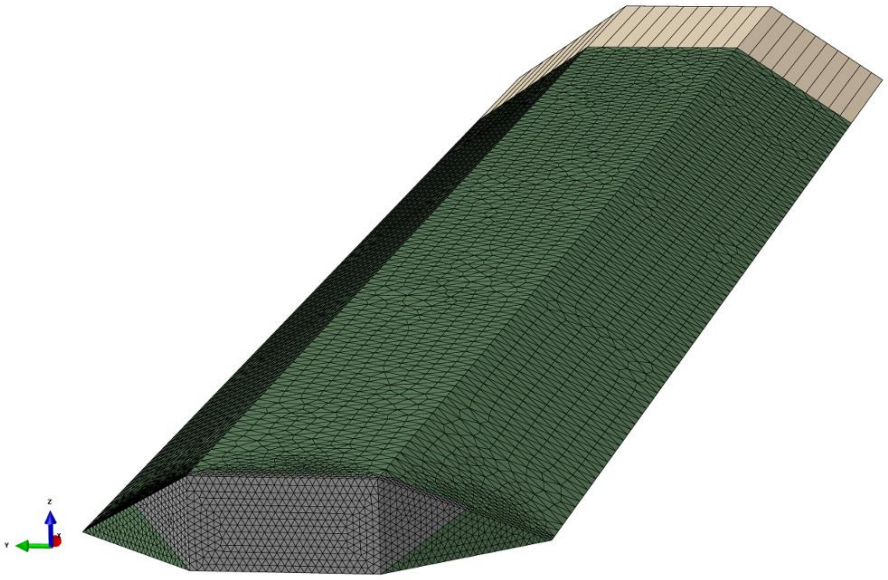

Figure 3.10: The TET-model, meshed mainly with tetrahedral elements. One part is the embankment up to the infinite boundary, and the other part is the infinite boundary that requires a structured mesh.

Bias

In ABAQUS, there is a possibility to use so-called bias functions. These are functions that create a mesh that is finer in one end and courser in the other, with a defined increase in-between. The shortest wavelengths, governing the elements size as described in 3.1.6, attenuate close to the source of vibration. As mentioned, that is why a courser mesh can be used at a distance from the source. In this thesis, linear bias functions were used and compared to models with a constant element size in a convergence study, presented in section 3.2.2.

When running analyses on the biggest models, the ones with embankment and circular soil plate, the number of degrees of freedom, and hence the computational costs, increase rapidly with the depth of the plate. To save costs, one wants to let the elements increase in size both in the radial direction and with the depth. No technique was found working for using a built-in bias function on the rather complicated geometry of the soil plate. Instead, the soil plate geometry was partitioned, where the parts closest to the vibrating source was given a finer mesh than the ones at a far distance, see Figure 3.11. The depth of the plate was divided into two layers, for ensuring that the depth will be divided in at least two elements even at the outer boundaries. To make the mesh finer in the center, each layer was partitioned with a circle, inside which the elements size was set smaller than outside.

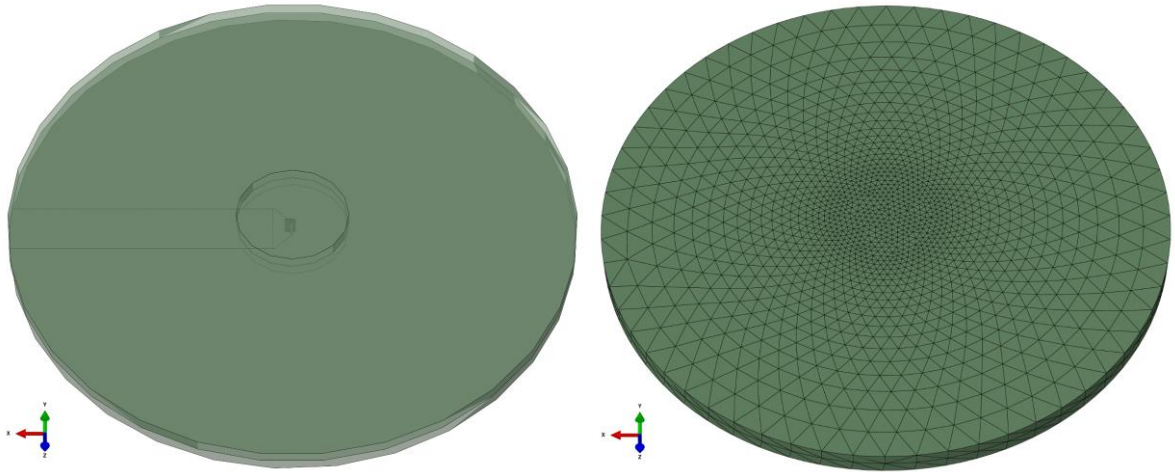

Figure 3.11: Partitions of the ground soil plate, making the mesh finer close to the source of vibration. *Left*: Slightly translucent bottom view where the partition lines are visible as the circle in the middle and the line dividing the depth in two parts. Visible in the middle is the foundation slab, seen from under. *Right:* Mesh of the soil plate created with the partitions, bottom view.

3.2 Method of analysis

As was described in Chapter 2, the impedance functions are obtained by inverting the receptance received from a steady state analysis. In ABAQUS, a steady state analysis of frequencies in a range from 1-30 Hz is carried out, with small enough frequency increments to capture enough details in the curves. In this case, 180 increments were used, i.e. frequency increments of 1/6 Hz. Real-valued unity loads (input) were applied in the reference point coupled to the bridge wall, where also the displacements (output, the receptance) were recorded. The receptance and the real and imaginary parts of the impedance were then plotted against the frequency and constitute the results of this thesis, presented in the next chapter, and in Appendix A. A closer description of the method of computing the receptance and impedance functions is given in the next section.

The analysis was carried out both on a personal computer and on Lunarc (2016a), the center for scientific and technical computing at Lund University, which is more adapted to solve computationally expensive problems and handle large amounts of data. Lunarc stands for *Lund University NIC (Numeric Intensive Computation) Application Research Center* and provides computational resources through supercomputers and computer clusters for academia in Sweden. Lunarc deploys SLURM (*Simple Linux Utility for Resource Management*) for managing the resources of the computers. With SLURM the user can submit jobs from a PC through a job description file, stating resource and wall time requirements, software modules needed (in this case ABAQUS) and input files to run the analyses on. The chosen computer system, either *Erik* or the newly employed *Aurora* will then calculate what is stated in the input file and return output files that can be copied from the Lunarc local directory to the user's PC through a SSH file transfer protocol, SFTP. Aurora is a cluster system of 180 nodes with 2x10 CPU cores and 64 GB of memory per node. A node on the smaller system *Erik* consists of two 8-core CPU's, either 64 or 96 GB memory and offers the usage of GPU's (*Graphics processing units*). More about Lunarc and the job submission methods can be found on the Lunarc Documentation pages (2016b).

3.2.1 Computing receptance and impedance functions

In Figure 3.12, the wave propagation in one of the embankment models for a specific frequency and load component (point load in the axial direction, FX) is shown. The model used is the one with stiff, homogeneous soil, and wing walls included. In the

figure, the waves have attenuated when reaching the boundary, not giving any reflections back to the reference point.

In the load input node (RP, described in section 3.1.3), the displacements and rotations (the receptance) in all 6 degrees of freedom and for all frequency increments were extracted through a Python script. In this script, a tree dimensional matrix (with the dimensions 6x6x180 where each row indicate the load/moment direction, each column indicate the displacement/rotation direction, and the length indicate the frequency) were created, and thus containing all the components of the receptance. As the components in the diagonal of the matrix (i.e. longitudinal displacement for load in the longitudinal direction, bending around the vertical axis for a moment around the vertical axis, etc.) are big compared to the rest of the components (for example bending around the vertical axis for a load in the transversal direction), only the diagonal vectors are presented and compared to each other in the results chapter. The rest of the vectors in the matrix will contribute to the SSI when applying them to a bridge model as boundary conditions, but would be hard to interpret when only looking at the receptance and impedance functions as in this thesis.

The receptance is made up by complex numbers, but the real and imaginary parts do not contain any useful information separately. Instead the absolute value were calculated, and plotted against the frequencies, yielding the magnitude of the receptance. One could also choose to plot the real part of the receptance, which would look very similar to the curves with the magnitude, as the imaginary part is small.

The impedance were calculated by inverting the receptance. The real and imaginary part of the impedance were then plotted against the frequencies separately, as the real part contains the dynamic stiffness and the imaginary part contains the dynamic damping.

In Figure 3.13, the receptance and the real and imaginary parts of the impedance are plotted for an embankment model. The plots show a characteristic appearance of impedance functions for loading in the vertical direction. At low frequencies, both the receptance and impedance hold constant values. When the loading rate gets closer to its first natural frequency, in this case about 11 Hz, the receptance increases rapidly, as is the nature of the resonance phenomena. At this point, the dynamic stiffness (real part of the impedance) of the system has decreased to zero, and the dynamic damping (imaginary part of the impedance) has increased to a high enough value to dampen the first resonance, still at a very low value.

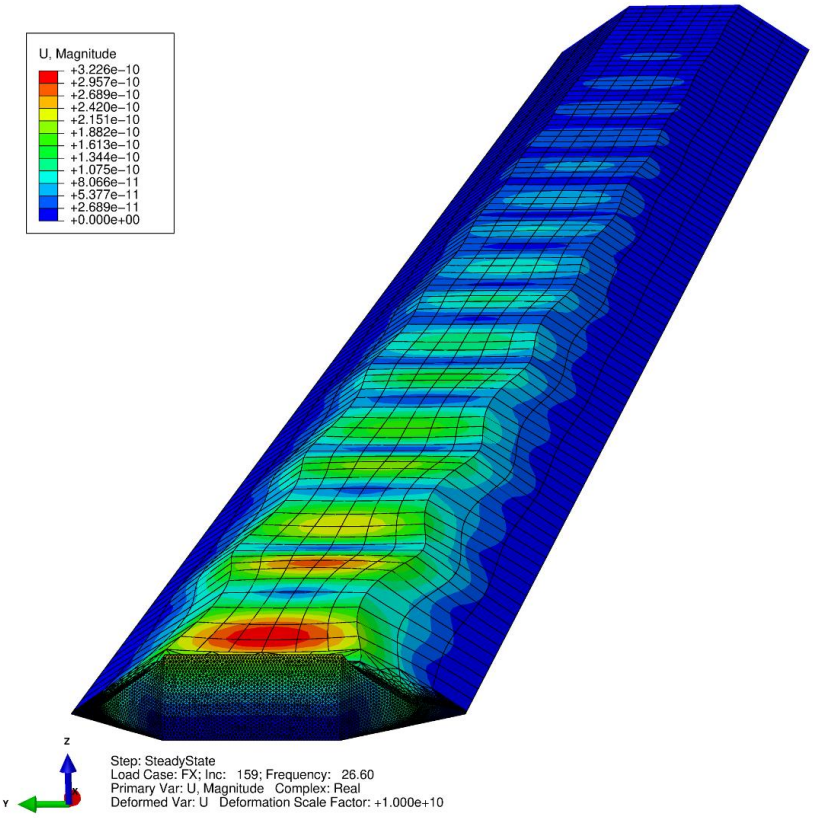

Figure 3.12: Wave propagation in the embankment model.

When the frequency is further increased, the damping is increased towards its highest value, taking place at about 12 Hz, called the anti-resonance frequency.

The receptance undertakes its lowest value at the same frequency. Between the resonance frequency and the anti-resonance frequency, the value of the dynamic stiffness jumps from a large negative value to a large positive value. This is due to the nature of complex numbers, when the real component of the receptance goes from a small negative to a small positive number, passing zero.

The system reaches its second resonance frequency at about 18 Hz. When the frequency is further increased, the dynamic damping increases and the dynamic stiffness decreases.

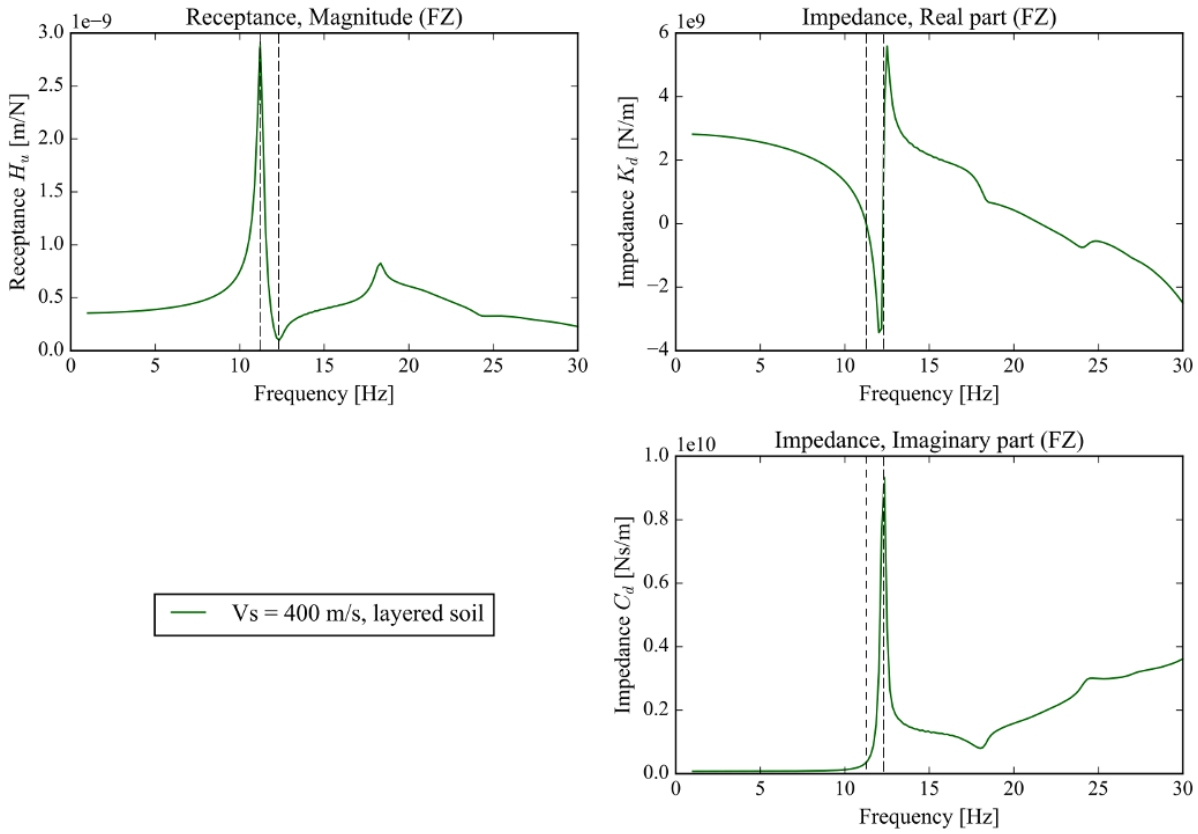

Figure 3.13: The frequency response function, receptance, and the complex components of its inverse, the real and imaginary parts of the impedance. Dashed lines indicate the first resonance and anti-resonance frequencies.

3.2.2 Convergence study

To ensure that the model quality is sufficient in order to fulfill the radiation condition, it is important to perform convergence tests. As mentioned in section 2.1, the convergence criterion means that the numeric solution should converge towards the exact, analytical solution when increasing the number of elements. In this thesis, where the exact solution is not available, the convergence criterion will instead be considered to be fulfilled when the solution no longer shows any difference due to a change in element size, meshing technique, geometry, etc. The increase of elements will either be from a decrease in mesh size or an increase of the size of the model.

The convergence study was performed on both the HEX- and the TET-model with the properties stated earlier in this chapter and summarized in Table 1.

Table 1: Properties of bridge-embankment model. Constant values and default values of properties to be determined in convergence study.

Constant properties		
$\mathbf{h_{emb}}$	5	[m]
$\mathbf{w_{emb}}$	12	[m]
$\mathbf{v_s}$	150	[m/s]
Inclination of slopes	1 : 1.5	
Wing walls	Yes	
Default values to be varied in convergence study		
Mesh size embankment	$\lambda_{min}/_4$	[m]
Mesh size bridge wall	$wallthickness/_2$	[m]
Length embankment	$\lambda_{max}/_4$	[m]

Length of embankment

The length of the embankment plays an important role according to theory, as an increase of the length can both help to better fulfill the radiation condition, and to decrease the relative element size, i.e. the size of the elements in relation to the size of the whole model. The latter one is, however, believed to be less important in the models in this project, as the element size will be more dependent on the shortest wave length, which will be constant when varying the length of the model.

As can be seen in Figure 3.14, the length of the embankment plays an important role for the model quality. The ripples in the receptance curves stems from wave reflections on the infinite boundary and decreases with increased length. Full convergence was not achieved even with the longest embankment which was much longer than the theoretical length believed to be sufficient. This held true both for the HEX- and the TET-model. Between the lengths of $\lambda_{max}/2$ and $\lambda_{max}/4+80$ meters, however, very small deviations were observed, so the former length was considered sufficient. The remaining ripples were believed to depend on the mesh size, which was studied in a subsequent convergence test.

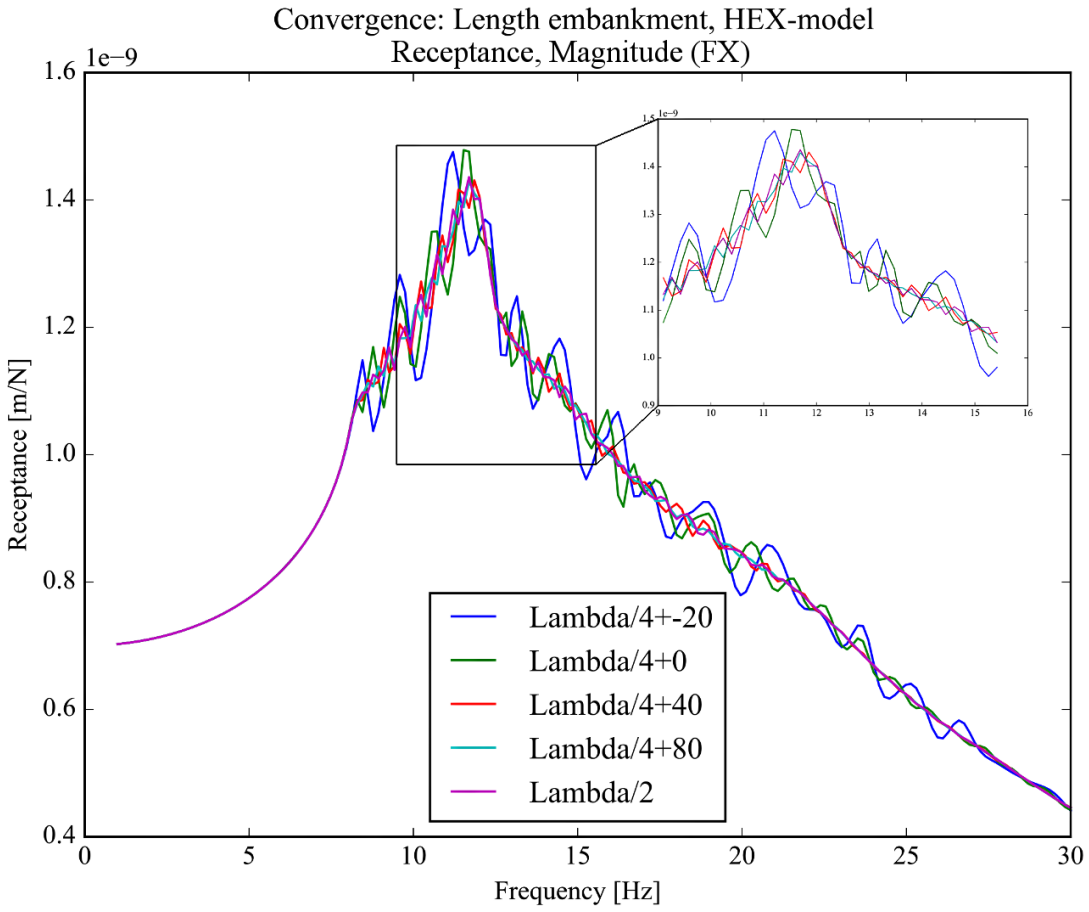

Figure 3.14: Magnitude of the receptance in the x-direction (longitudinal) for a load in the same direction (FX). The importance of the length of the model is illustrated by the disturbances in the receptance curves that are larger for shorter models.

Element size

Several tests of convergence were performed to determine a sufficient element size throughout the model. The first one was to determine the mesh size of the embankment soil. Here, the importance laid in capturing the wave motion, governed by the shortest wave length. In Figure 3.15, the impedances are presented for a model with all parameters except the element size kept constant.

The first diagram shows the model where mainly HEX elements are used, and the second shows the model with TET-elements. For both models, the elements size seem to be insignificant at lower frequencies. This is because the lower frequencies yield longer wave lengths, and thereby no need for a fine mesh.

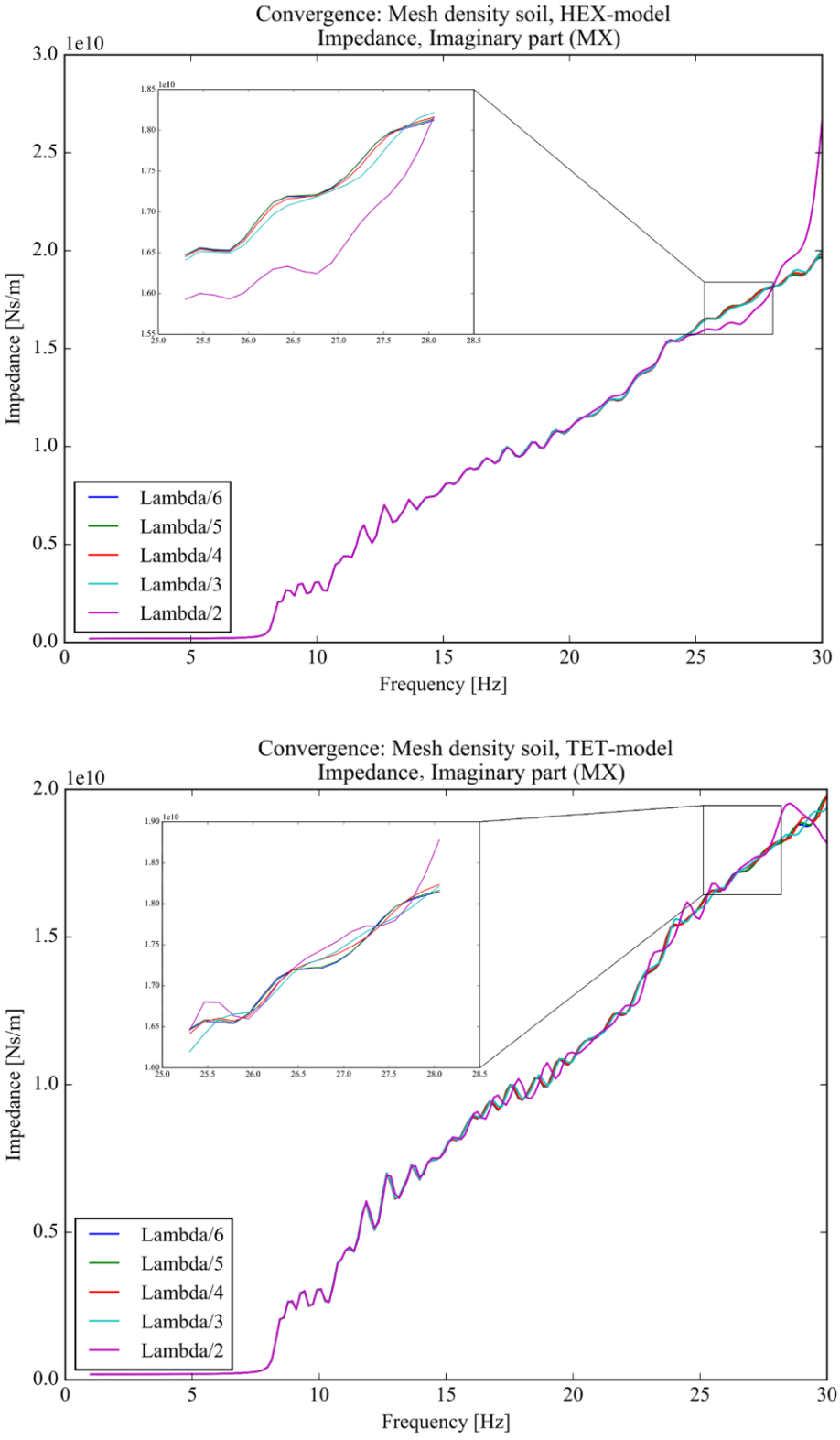

Figure 3.15: Importance of element size shown through a convergence test of the imaginary part of the impedance. Top: HEX-elements. The lines are considered to converge at a fourth of the shortest wave length. Bottom: TET-elements. A finer mesh seems to be needed when using the TET-elements.

At high frequencies, however, deviations can be seen in the curves with element sizes of $\lambda/2$ and $\lambda/3$, and for the TET-model even $\lambda/4$. The reason for this that the HEX-elements introduce more nodes to the model, reducing the numerical dispersion. The fact that the TET-models show deviations for a finer mesh than the HEX-model indicates that the HEX-model is advantageous to use to save computational costs. This is further confirmed by the fact that the models with TET-elements took longer to compute than the models with HEX-elements of the same size. The HEX-elements have the advantage of enabling reduced integration, which reduces the computational time.

Mesh technique

Some different techniques for creating the elements mesh were tried in this study. As was concluded by the convergence test above, four elements per wave length were sufficient for capturing the wave motions in the soil. A finer mesh is however believed to be needed closer to the bridge wall to be able to capture the strains in this area. In Figure 3.16, some different techniques used for meshing the model are illustrated, and in Figure 3.17, the real part of the impedance is plotted for said techniques with different elements sizes and bias relations. In the latter figure, t stands for the wall thickness and indicates the element size in the part closest to the bridge wall, and *Lambda* is the shortest wave length. The first four curves do not deviate at any frequency, why the conclusion is drawn that an element size of half the wall thickness in sufficient. It can also be concluded that the HEX- and TET- models do not differ from each other, which means that the TIE-constraint does not prevent the waves from propagating in the embankment, as was suggested in section 3.1.3. Because the same results were received regardless of using the TET- or the HEX-model, and the HEX-elements converged at a courser mesh, as was concluded in the last convergence study, the models in the parameter study was chosen to be meshed with HEX-elements.

It can be observed that the usage of bias functions does not affect the precision of the results significantly. This is likely to have its explanation in the attenuation of the smallest wavelengths close to the source of vibration and thus the lesser need for a fine mesh at a certain distance from the source.

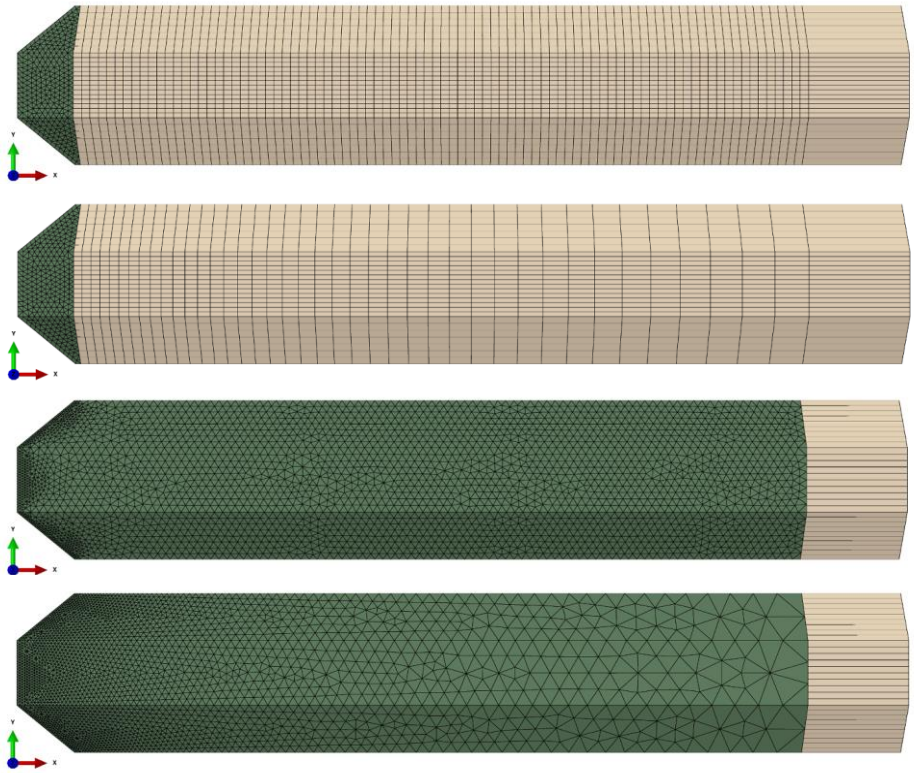

Figure 3.16: Meshing techniques. Green parts are TET-elements and beige are HEX-elements. *First*: HEX-model with constant mesh in bridge part (green) and soil part (beige). *Second*: HEX-model with a bias relation of 1:4. *Third*: TET-model with constant mesh. *Fourth*: TET-model, bias ratio of 1:4.

A tendency for distortion of the curves can however be observed when using large bias ratios (orange and light green curves in Figure 3.17). This could either be due to the elements growing too large for being able to capture the waves at the end of the model, or the linear bias function being unsuitable for the wave attenuation. It is possible that the waves attenuate in a non-linear fashion, and the elements increasing in size too close to the source. How large bias ratio that can be used, and what bias function is best suited, without reduction of precision, must therefore be further investigated.

An interesting observation is that the curve belonging to the TET-model with a bias ratio of 1:3 (purple line) shows larger deviation from the rest of the curves than the same bias ratio in the HEX-model. This further confirms that the HEX-model is a better choice in this study.

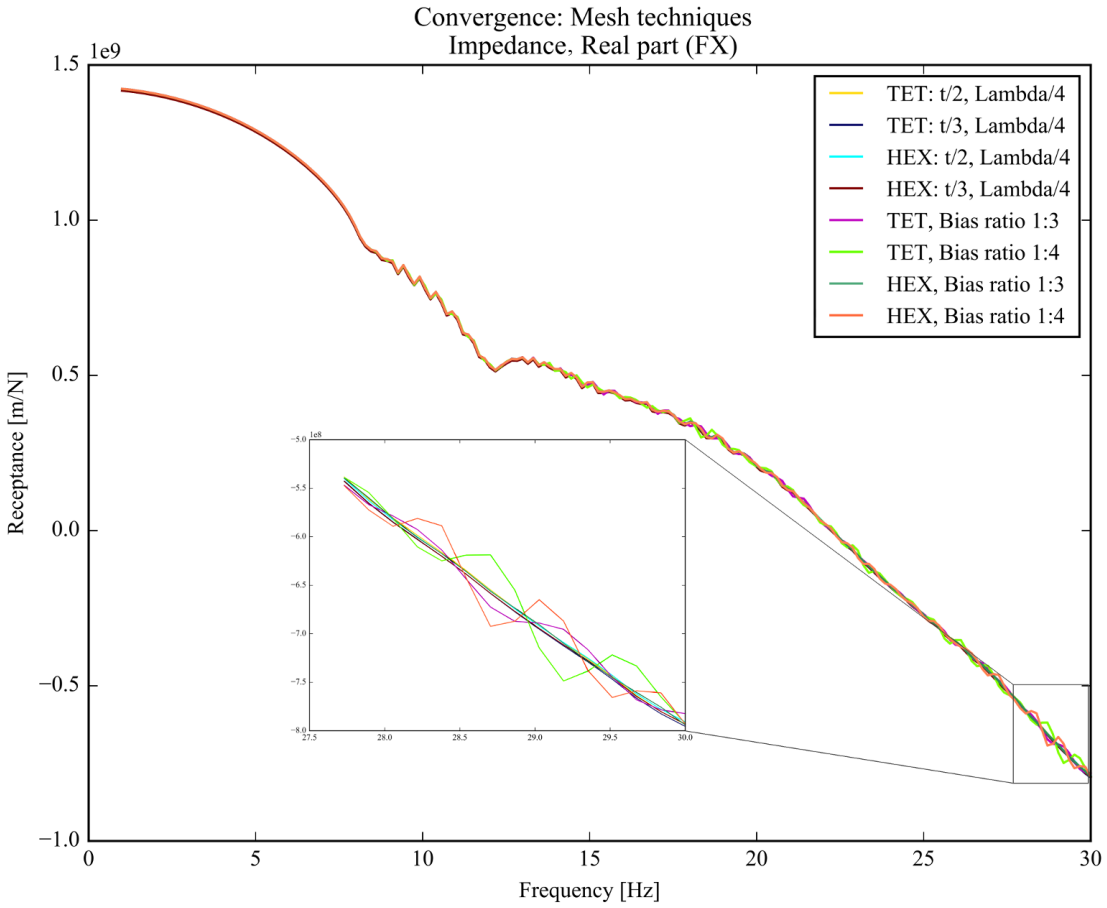

Figure 3.17: Impedances with different meshing techniques. Only deviations show, except for the highest frequencies for TET-elements with a bias ratio of 1:3 and 1:4 (light green and purple lines) and HEX-elements with a bias ratio of 1:4 (orange line).

Non-dimensional impedance functions

A way of checking if convergence is reached is to compare the impedances of models with different shear modulus. To do this, the plots need to be re-scaled as they otherwise would show different values at different frequencies and be hard to compare. A re-scaling is possible due to the linear nature of the calculations, and results in non-dimensional functions of impedance and receptance. Convergence is reached if the re-scaled plots coincide, otherwise the models must be refined in some of the aspects mentioned in the previous convergence studies.

In Figure 3.18, the receptance and impedances are plotted for two embankment models with the same geometrical features but with different shear moduli. As can be seen, the curves do not completely coincide when plotting the imaginary part of the impedance. The damping seems slightly underestimated for the stiff embankment, or overestimated for the soft one. The model used in this study was one that was

subsequently removed from the thesis, based on the fact that it did not constitute a very realistic representation of a real portal frame bridge. The model had a 5 meters high bridge wall and embankment, resting on a 5 meter extra soil layer (not to be confused with the soil plate of the big model), more resembling an end-frame bridge.

The ripples that can be seen on the purple line are probably due to the radiation condition not being completely fulfilled for the soft soil. The lines do no completely coincide at 0 Hz, i.e. for the static case. A possible explanation for this is that the mesh of the bridge wall and the soil in contact with it, is not fine enough to capture the stress concentrations in the interface between the bridge wall and the soil, where the stiffness decreases abruptly.

An interesting, and somewhat unsettling discovery was that the models with embankment directly on bedrock did not show the same tendency to converge as the embankments on 5 meters of intermediate soil, which is illustrated in Figure 3.19. This was surprising, as the previous convergence studies were carried out on these exact models and gave satisfactory results. The damping seems to be right, as the curves plotted for the dimensionless dynamic damping (middle right plot) converged. The stiffness, however, is either overestimated for the soft embankment, or underestimated for the stiff model, when plotting the dimensionless curves. This convergence test was carried out on the model with 6 meters wide embankment, homogeneous soil and wing walls included, but gave similar results for all models with embankment on bedrock.

The lack of convergence were, after several trial-and-error attempts, found to be due to the soil-concrete interface. In the soft embankment, the relation between the Young's modulus of the soil and that of the concrete were 1:365, which could be considered infinite. For the stiff embankment, however, the relation was only 1:51, which apparently could not be considered infinite.

To gain convergence, all parameters except the stiffness had to be kept constant, and with different stiffness relations, this was not the case. When trying to increase the concrete stiffness so that the relation became the same as for the soft soil, convergence were reached, see Figure 3.20. The plotted lines go together perfectly, indicating that both models behave in the same fashion.

The discovery that convergence could be reached by increasing the concrete stiffness reassured that the models were of good quality, even when using the lower stiffness values. It also indicates that the stiffness of the concrete is more important when having a high stiffness in the soil. This will be further addressed in the discussion in Chapter 5. To not use any un-realistic material values, the Young's modulus of 34 GPa were used for all models in the subsequent parameter study.

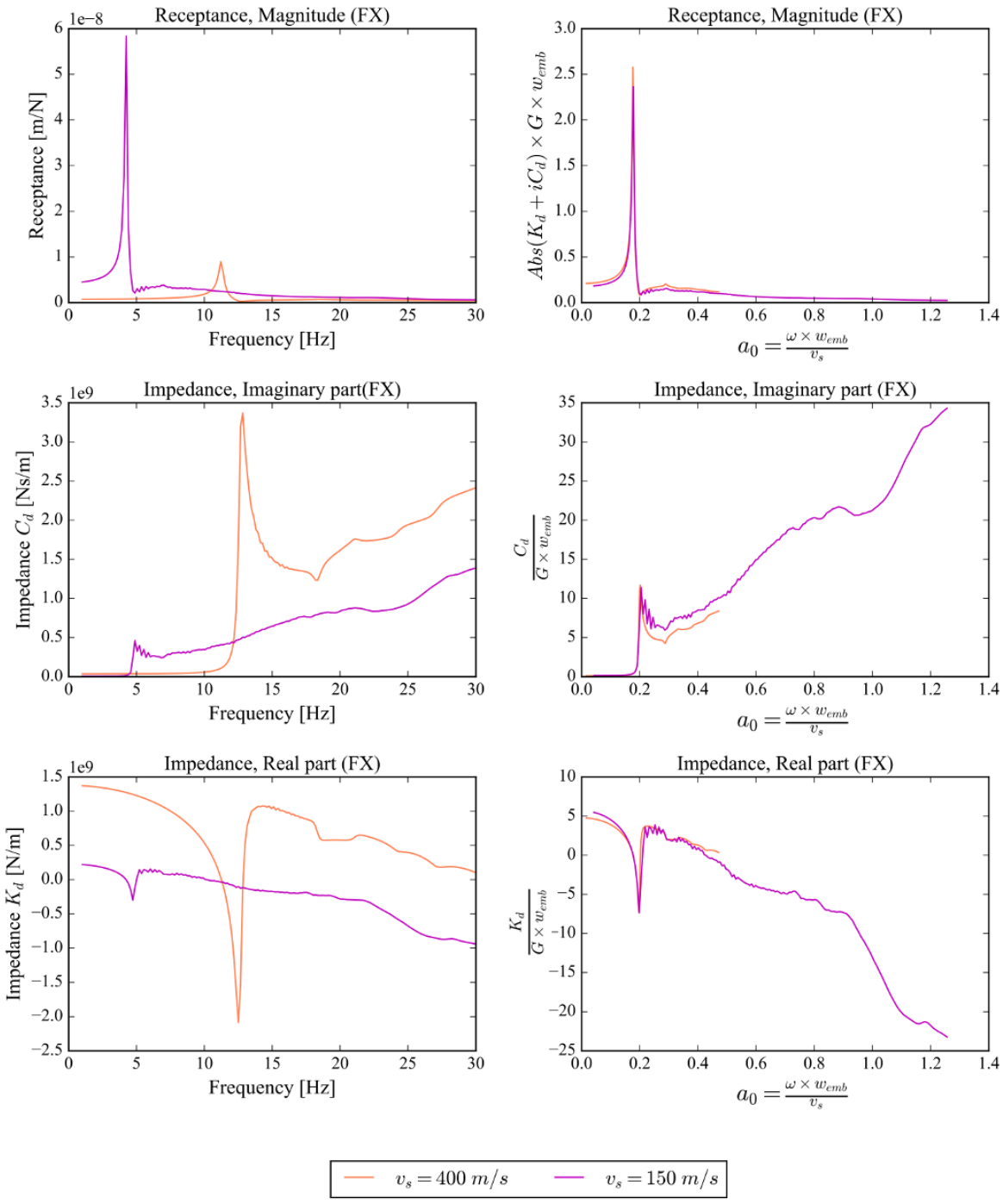

Figure 3.18: Receptance and impedance for soft and stiff embankment models for checking convergence. To the left is the real response and to the right is the non-dimensional plots, re-shaped from the plots to the left.

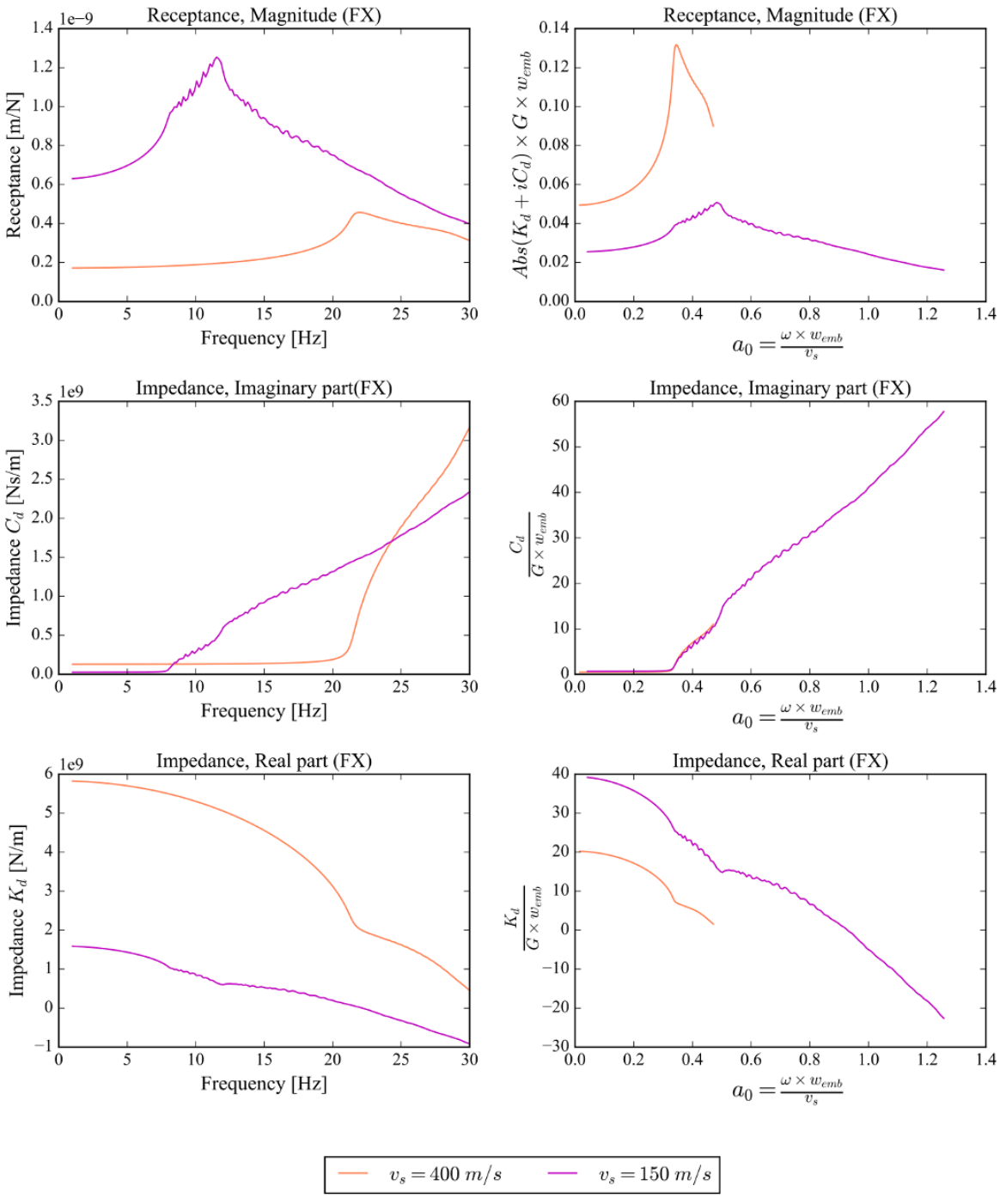

Figure 3.19: The same type of convergence test as shown in the previous figure. This figure shows that the model with soft embankment on bedrock does not seem to converge with the one with stiff soil.

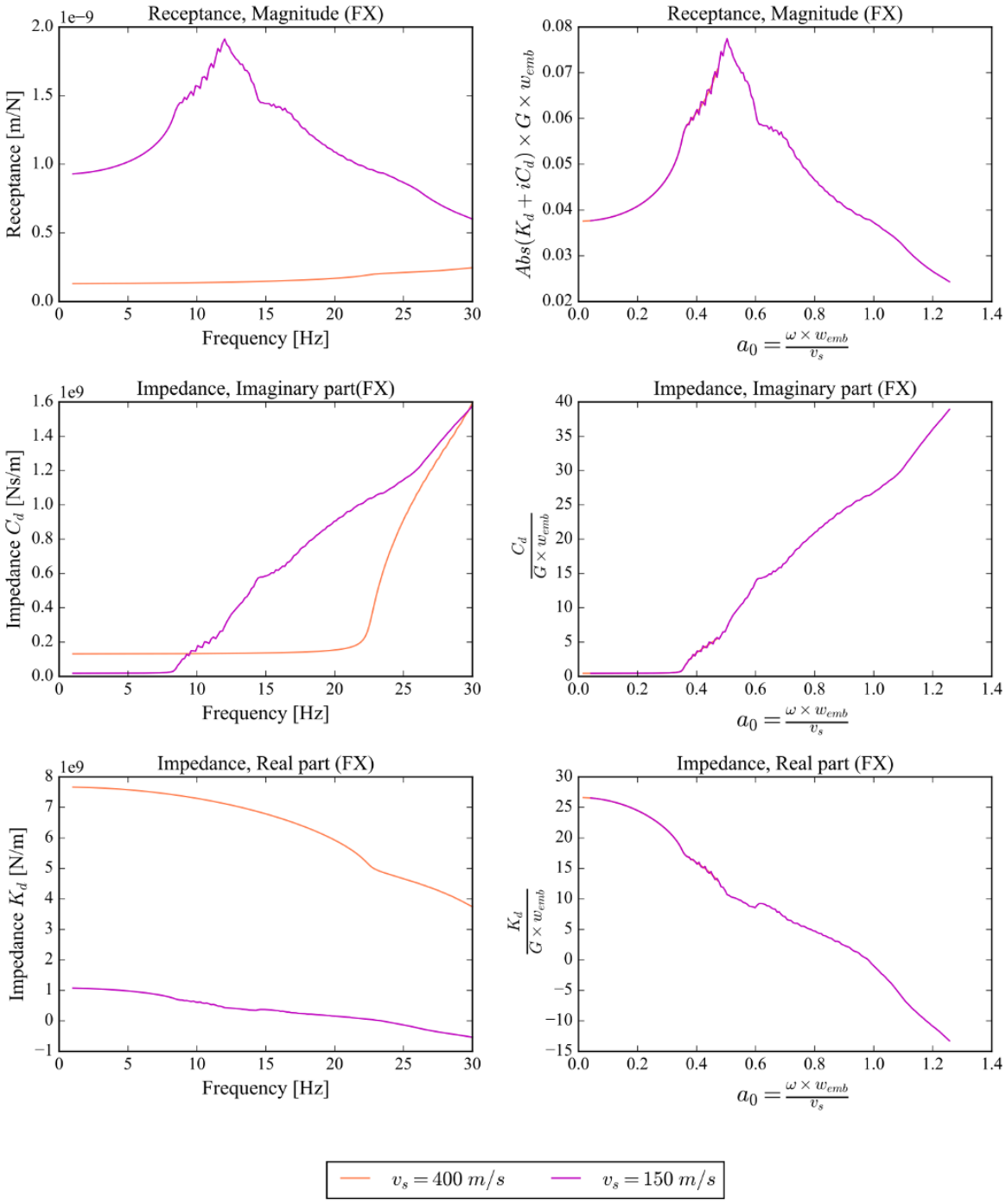

Figure 3.20: Convergence test on the same model as in the previous figure, but here with an increased stiffness in the concrete in the model with stiff soil. In the diagrams to the right, the orange and purple lines coincide, indicating that convergence is reached by giving the same stiffness ratio between the concrete and the soil for both models.

3.2.3 Final models

The models used for calculating the impedance functions for a soil-bridge interface are illustrated in Figure 3.21. The mesh is finer close to the source of vibration, and increases in size towards the infinite boundary.

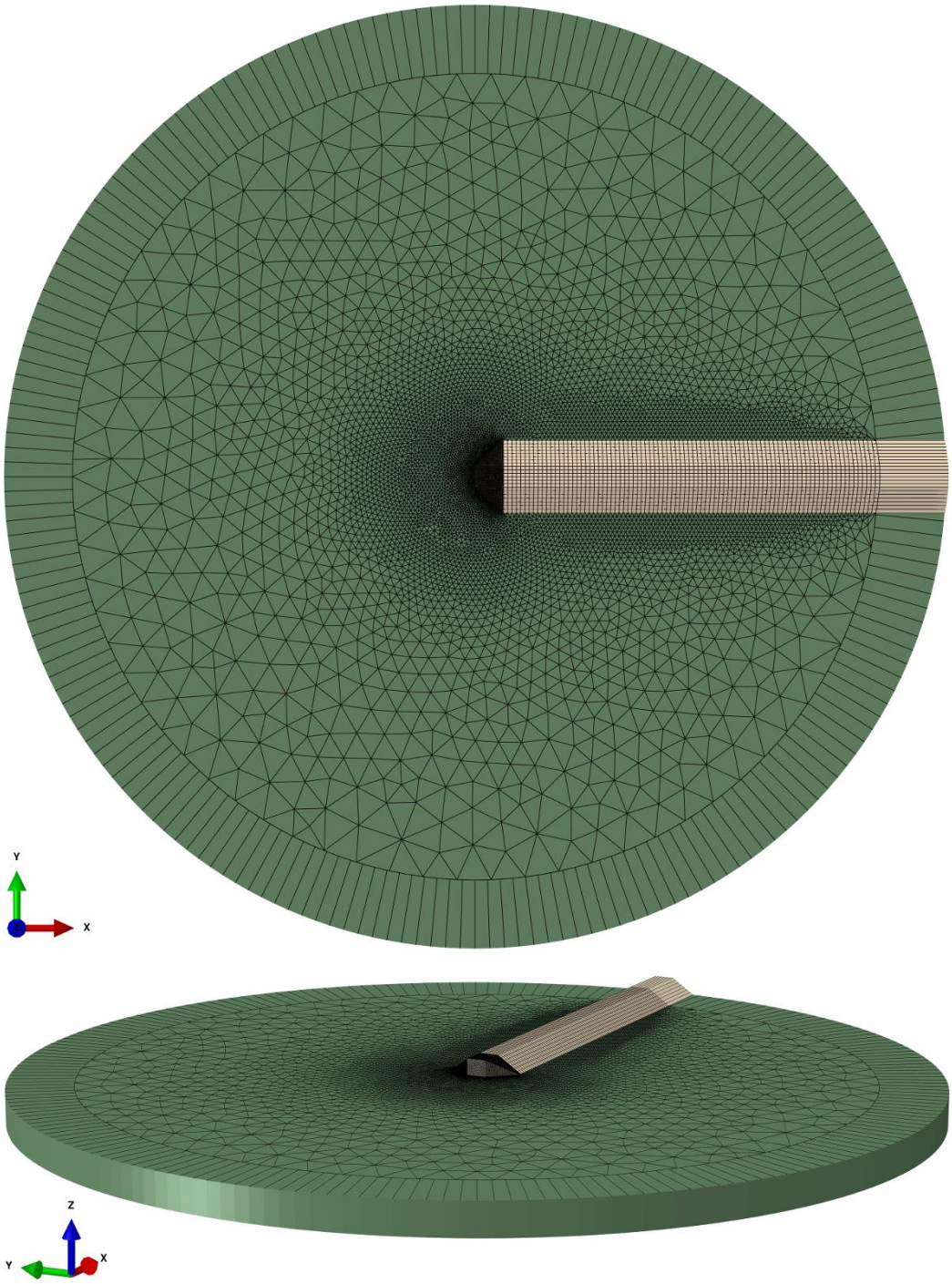

Figure 3.21: One of the big models used in the parameter study. The infinite extent of the boundary elements are represented by the absence of exterior edges in the ground soil plate.

As will be explained in the next section, the embankment resting on the soil plate were analyzed separately, to reduce the time consumption for the parameter study.

The length of the embankment, and thereby the radius of the soil plate were set to $\lambda_{max}/2$. For the stiff soil with a shear wave speed of 400 m/s, this meant a length of 312 meters, and for the soft soil with a shear wave speed of 150 m/s, 117 meters. These lengths were measured up to where the infinite boundary started. The element sizes of $\lambda_{min}/4$ meant about 1.2 meters for the soft soil and 3.2 meters for the stiff soil. This resulted in a large amount of d.o.f's, about $3.4x10^5$ for the models with only embankment, and $1.6x10^6$ for the models with embankment and ground soil plate.

3.2.4 Parameter study

The influence of different factors was studied through a parameter screening. The parameter screening was carried out as a two-level factorial test where each variable factor was investigated in only two levels. All combinations of the levels of the factors were investigated, resulting in 2^n tests. Each test was carried out on four embankment models with varying level of detail, giving a total of $4x2^n$ tests. The factors varied in the parameter screening were:

- Width of embankment and bridge wall: 6 or 12 meters
- Shear wave speed: 150 or 400 m/s

The levels of detail, illustrated in Figure 3.22, were:

- Homogeneous soil in embankment, no wing walls.
- Homogeneous soil in embankment, wing walls included.
- Soil stiffness increasing with depth, no wing walls
- Soil stiffness increasing with depth, wing walls included

Hence, the total number of tests on the small models were: $4x2^2=16$.

Apart from the two-level factorial test on the small models, further tests were performed on the big model. These were carried out in a similar manner, but with less variations of the model's level of detail. The main aim was to determine the influence of the depth of the soil plate, why three different values were given, 5, 10 and 15 meters. The second variable was the stiffness of the soil, where the most interesting way of comparing the models were considered to be to vary the relation between the embankment soil stiffness and the ground soil stiffness. These tests were carried out

with the soft-soil embankment with a shear modulus of 40.5 MPa. It was also desirable to also include the stiff-soil embankments, but these models became too big even for the super computers of Lunarc.

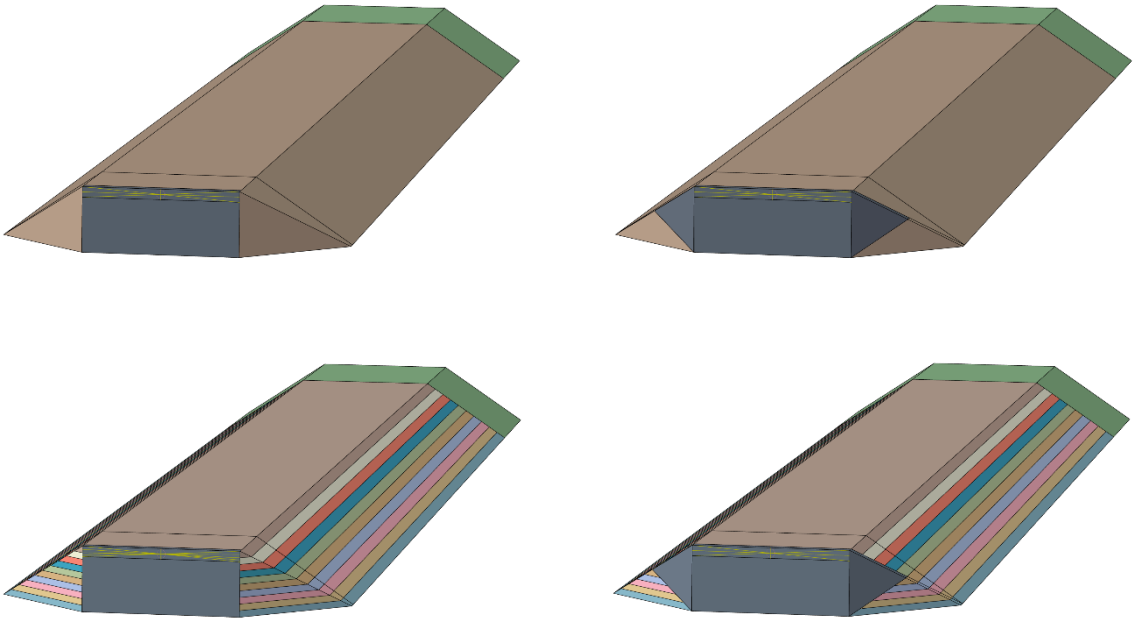

Figure 3.22: Variation of detail levels. *Top left:* Homogeneous soil, no wing walls. *Top right*: Homogeneous soil, wing walls included. *Bottom left:* Layered soil, no wing walls. *Bottom right:* Layered soil, wing walls included.

In the models, the embankment shear modulus (G_{emb}) were set to a constant value of 40.5 MPa, corresponding to the lower shear wave speed of 150 m/s. The ground soil was given three different values of the shear modulus (G_{ground}): $G_{ground}=G_{emb}/4$, $G_{ground}=G_{emb}$ and $G_{ground}=G_{emb}$ x 4. These values stems from choosing shear wave speeds of half of, same as, and double the shear wave speed of the embankment soil. The lower value could represent a clay, and the higher ones moraine, according to Figure 3.5.

With the two parameters varying between three values, the total number of tests for the big model were: $3^2=9$.

Chapter 4

Results

In this chapter, some of the impedance functions calculated in the parameter study will be presented and analyzed. The data is presented in the form of diagrams of the real and imaginary parts of the impedance. The parameter study resulted in 21 figures, each with 6 plots of impedances and receptance and it is obvious that not all of them can be presented here. Instead, the importance of each individual parameter will be presented. The rest of the computed impedance functions can be found in Appendix A.

4.1 Parameter study

In this section, the parameters that showed to affect the impedance of the models will be presented. The figures presented are the ones that showed the most characteristic deviations when the parameters or levels of detail were changed.

4.1.1 Detail level

Whether including the wing walls or not, or using constant or varying soil stiffness, showed to give differences in the impedance and receptance. The model used in Figure 4.1 and Figure 4.2 is presented as Model-4 in appendix A, where also the receptance can be viewed. In the figures, the real and imaginary parts of the impedance, corresponding to stiffness and damping are shown. It is from those figures clear that modeling a layered or constant shear modulus do not have the same influence as including wing walls or not.

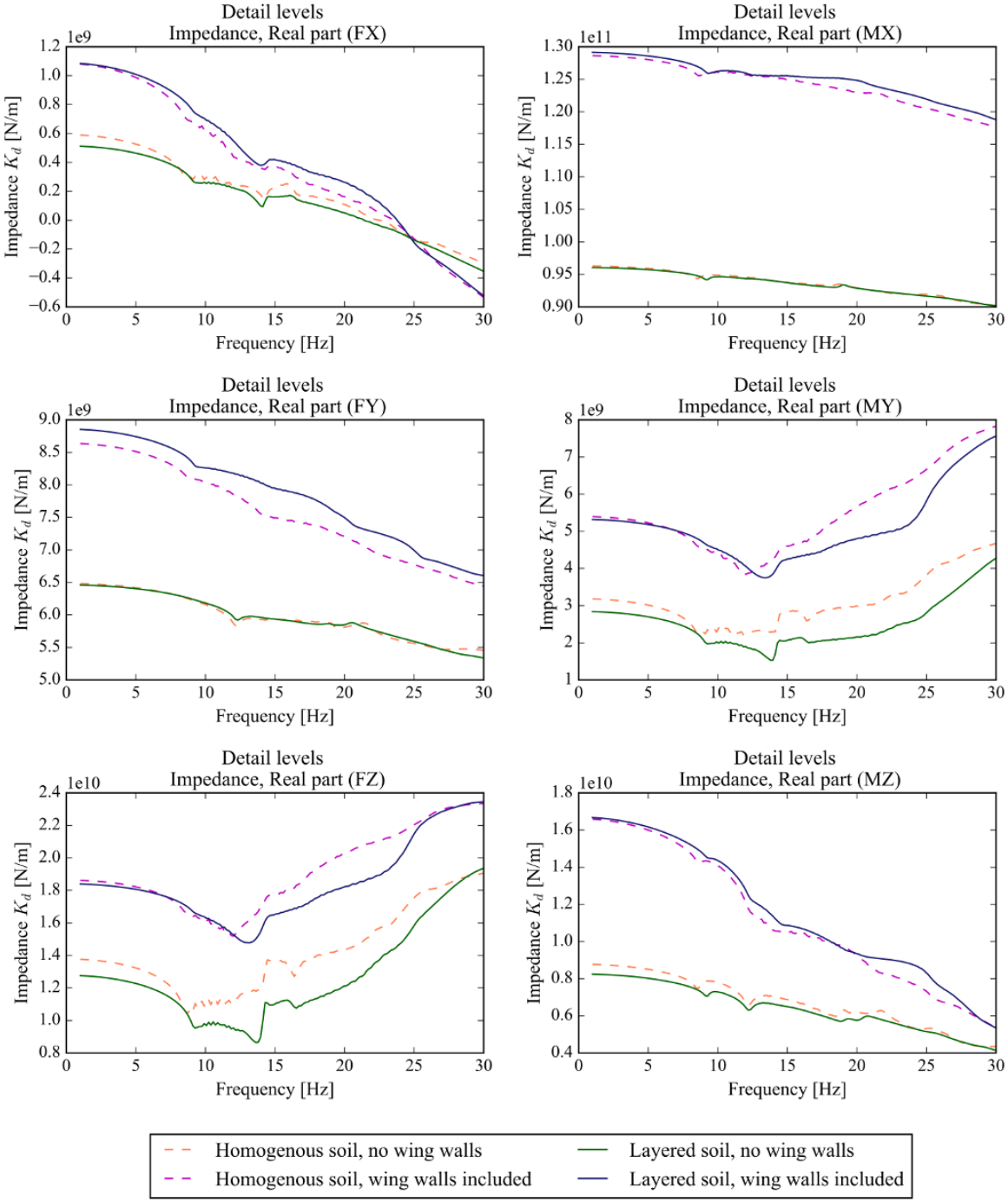

Figure 4.1: Variation in dynamic stiffness due to levels of detail. Dashed lines indicate models with a homogeneous soil profile. Model used: Soft soil and 6 meters wide embankment.

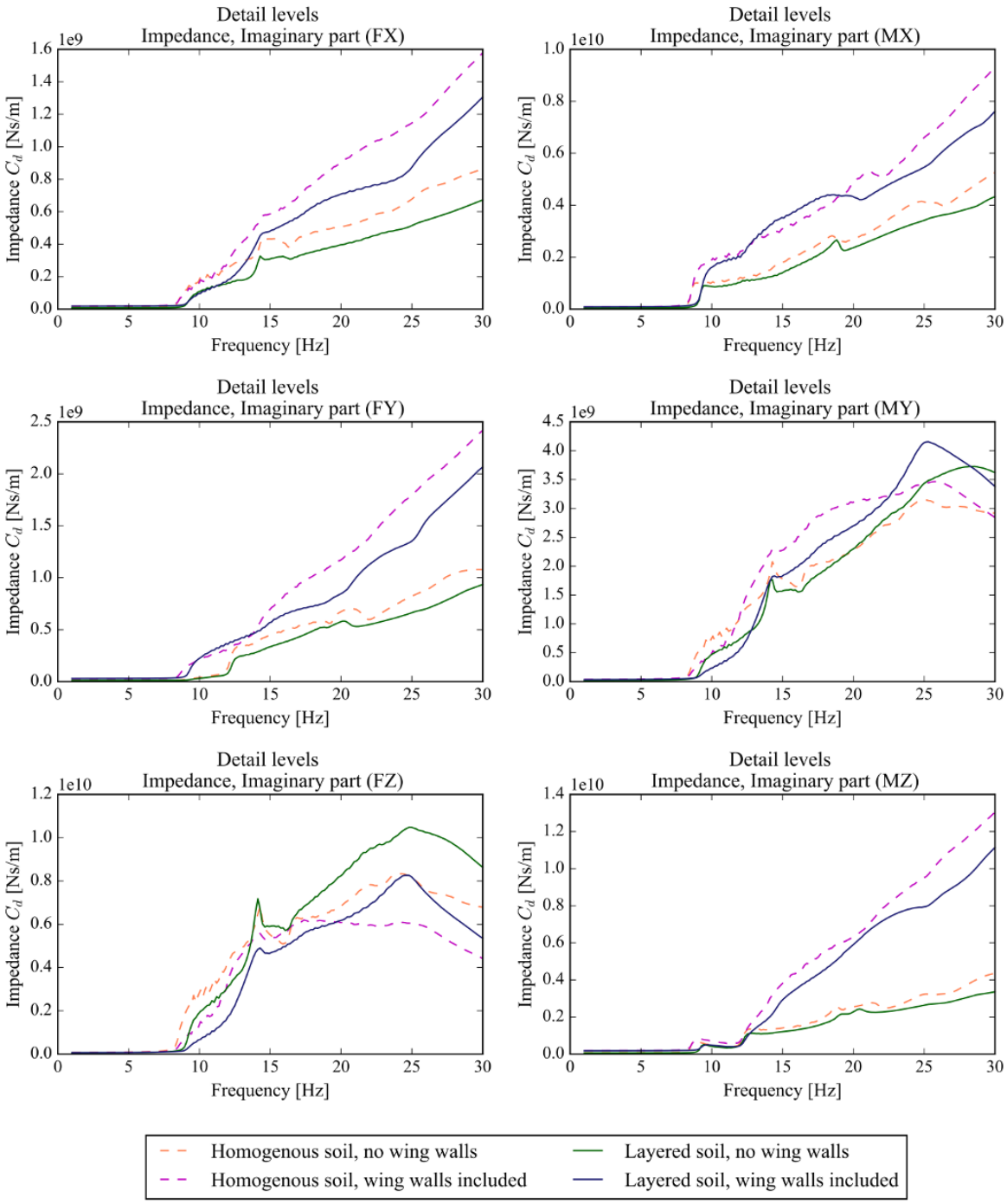

Figure 4.2: Variation in dynamic damping due to levels of detail. Dashed lines indicate models with a homogeneous soil profile.

The homogeneous soil profile induced more ripple to the impedance curves than the layered soil profile. This could be due to the more drastic change in stiffness between the soil and the bedrock in the homogeneous models. The layered soil had higher stiffness close to the bedrock and hence less spurious waves were induced. The layered soil had 10 layers of soil with increasing stiffness. As mentioned in section 2.5.1, this

change in stiffness could induce spurious waves, but apparently the increments were small enough to avoid this phenomena.

The stiffness increase when including the wing walls. This holds true for all directions for this specific model, but as will be apparent in Appendix A, some exceptions exist. For most directions, also the damping increase when including the wing walls. The exceptions in this model were the vertical direction (FZ) and for some frequencies also in bending around the transversal axis (MY). The increased stiffness is believed to depend on the increased bending moment of the bridge wall when wing walls are applied.

From the figures, it is hard to say whether a layered soil profile will give better results on the bridge accelerations. It can, however, be assumed that the layered soil gives a more realistic representation of the stiffness of the embankment. The fact that there are discrepancies between the layered and homogeneous soil profiles, indicates that the method of modeling the soil stiffness is important.

4.1.2 Width of embankment

In Figure 4.3, the imaginary part of the impedance for models with 6 and 12 meters wide embankments are presented. It seems like whether having a one- or two-tracked embankment effects the dynamic damping in the way that the two tracked induces more damping to the structure at high frequencies (compare purple and blue or orange and green lines). The width also seems to affect the resonance frequency.

In Figure 4.1, the largest differences are seen when comparing the models with wing walls with the ones without. In Figure 4.3, it seems like the width of the embankment can be even more considerable, as the curves belonging to different widths deviate more from each other than the curves belonging to the different detail levels. The clearest differences are, not surprising, shown when both the width and the level of detail are varied. It is notable that the inclusion of wing walls in the narrow embankment model seem to induce more dynamic damping in the transversal direction (FY), than in the other directions.

From Figure 4.4 it is clear that the two-tracked embankment induces more dynamic stiffness to the structure than the one-tracked embankment, which is not surprising as the static stiffness of the bridge wall increase with the width. One exception exists, and that is that when including wing walls in the narrow embankment, the dynamic stiffness in the longitudinal direction (FX) is highly affected, making the stiffness higher than in the wider tracked embankment without wing walls.

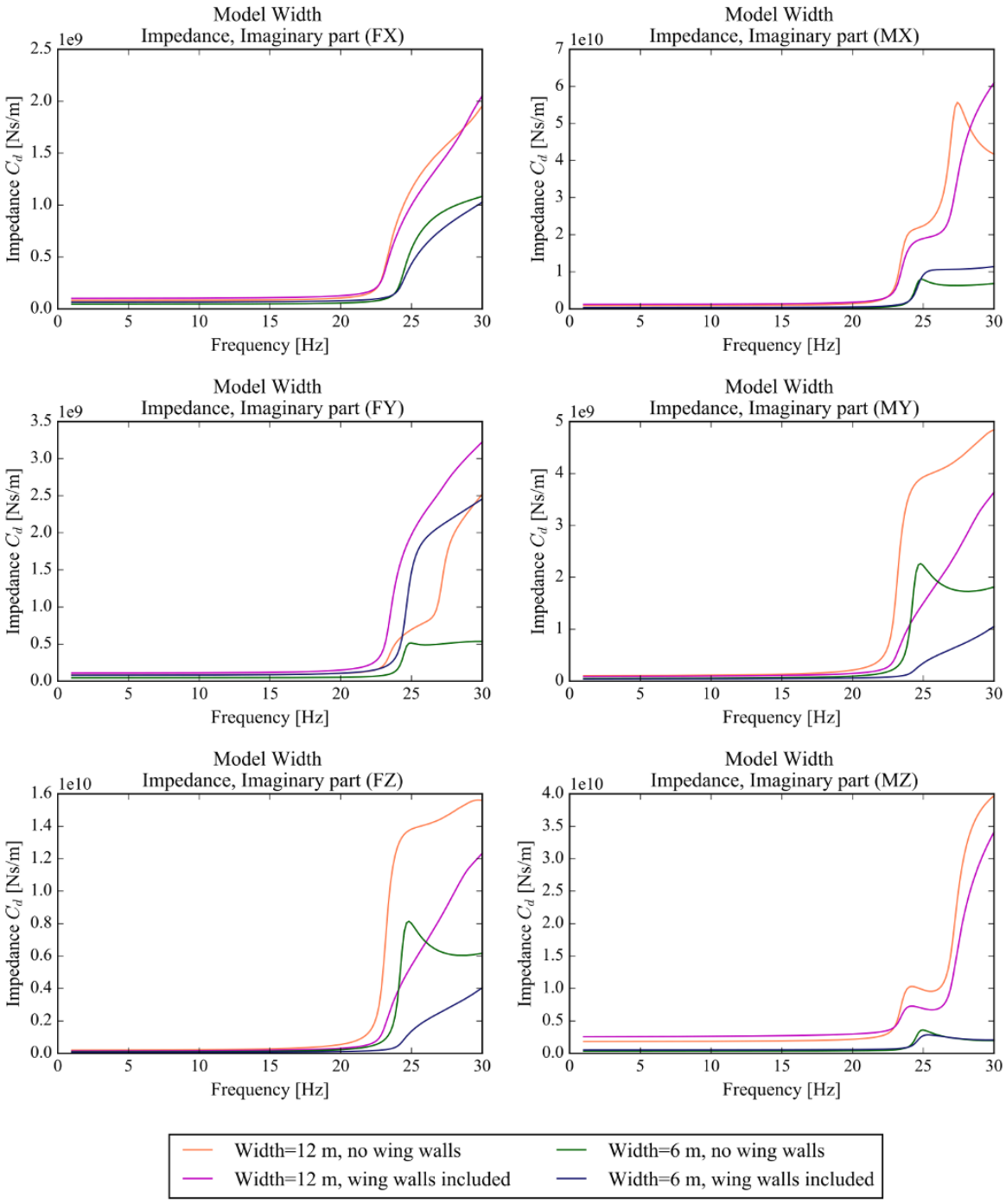

Figure 4.3: Dynamic damping for models of varying width and levels of detail.

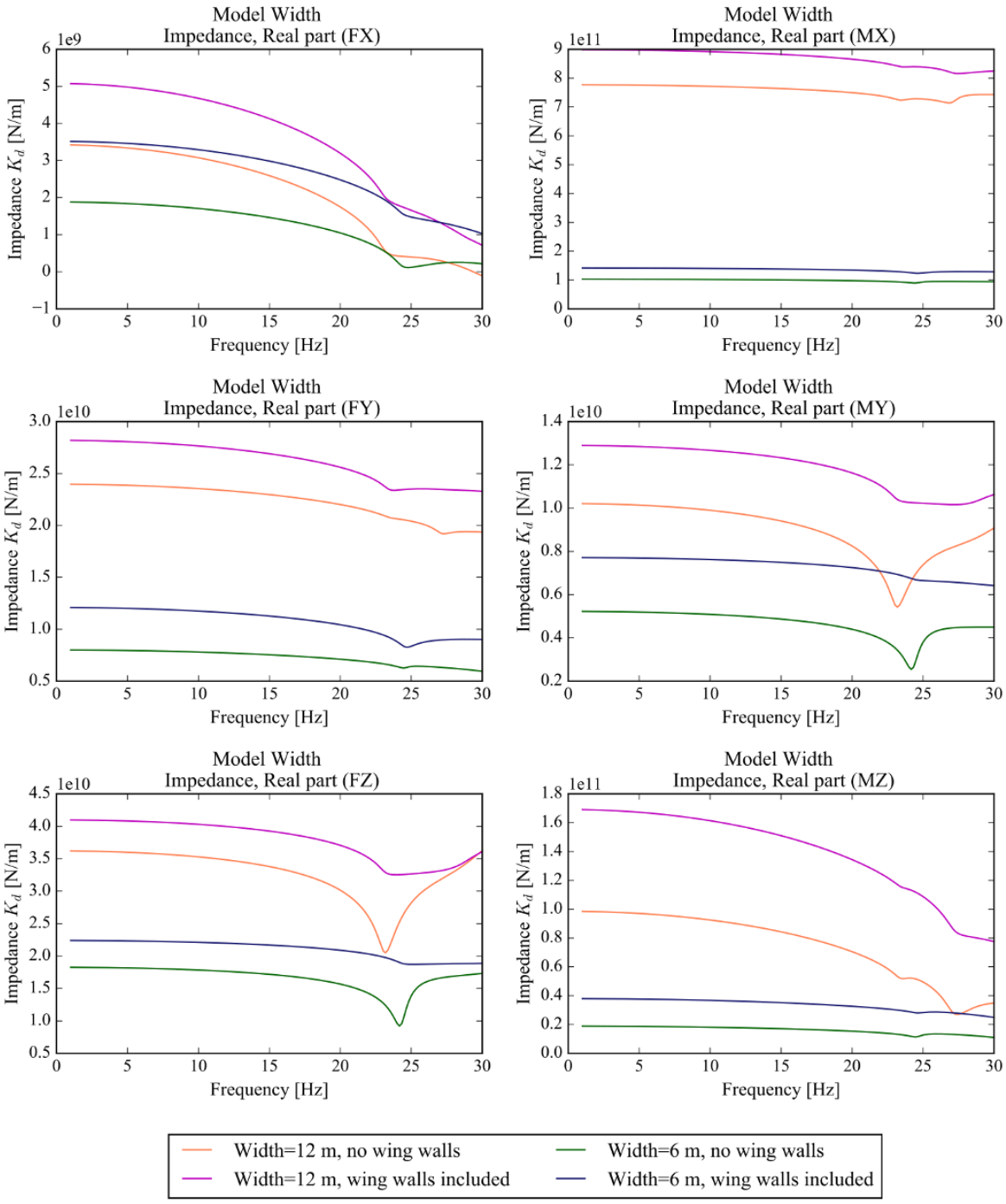

Figure 4.4: Dynamic stiffness for models of varying width and levels of detail.

4.1.3 Stiffness

The effects that the soil stiffness can have on the impedance will be presented in this section, first for the small models with embankment only, and then for the big models with embankment and soil plate. The models with included wing walls were used for these comparisons.

Embankment stiffness

In Figures 4.5 and 4.6, the real and imaginary parts of the impedance are plotted for embankment models of varying stiffness and methods of modeling the shear modulus, homogeneous or constant.

The first natural frequency differs quite much between the soft and the stiff soil. For the soft soil, resonance would occur at slower train speeds. Only looking at the impedances is however not enough, to say that modeling the soil softer than what is expected, always is conservative. The natural frequencies and mode shapes of the bridge are important, and must be investigated with applied impedance functions before such conclusions can be drawn.

One can again see that the way of modeling the soil stiffness – homogeneous or layered – has influence on the impedance and receptance. For both the stiff and the soft soil, there are differences in the resonance frequency depending on whether the soil is homogeneous or layered. The differences seem larger on the stiffer models.

The differences in resonance frequencies indicates the importance of well-known material parameters when taking dynamic effects on a bridge into account. Here, two extreme values of the embankment soil shear modulus have been compared, and shown to induce large differences in frequencies of resonance.

In especially the plots of the softer soil, ripples occurred. This can be due to the radiation condition not being completely fulfilled for the shorter model (shorter wave lengths in softer soil). Some of the Rayleigh waves could still bounce back into the model.

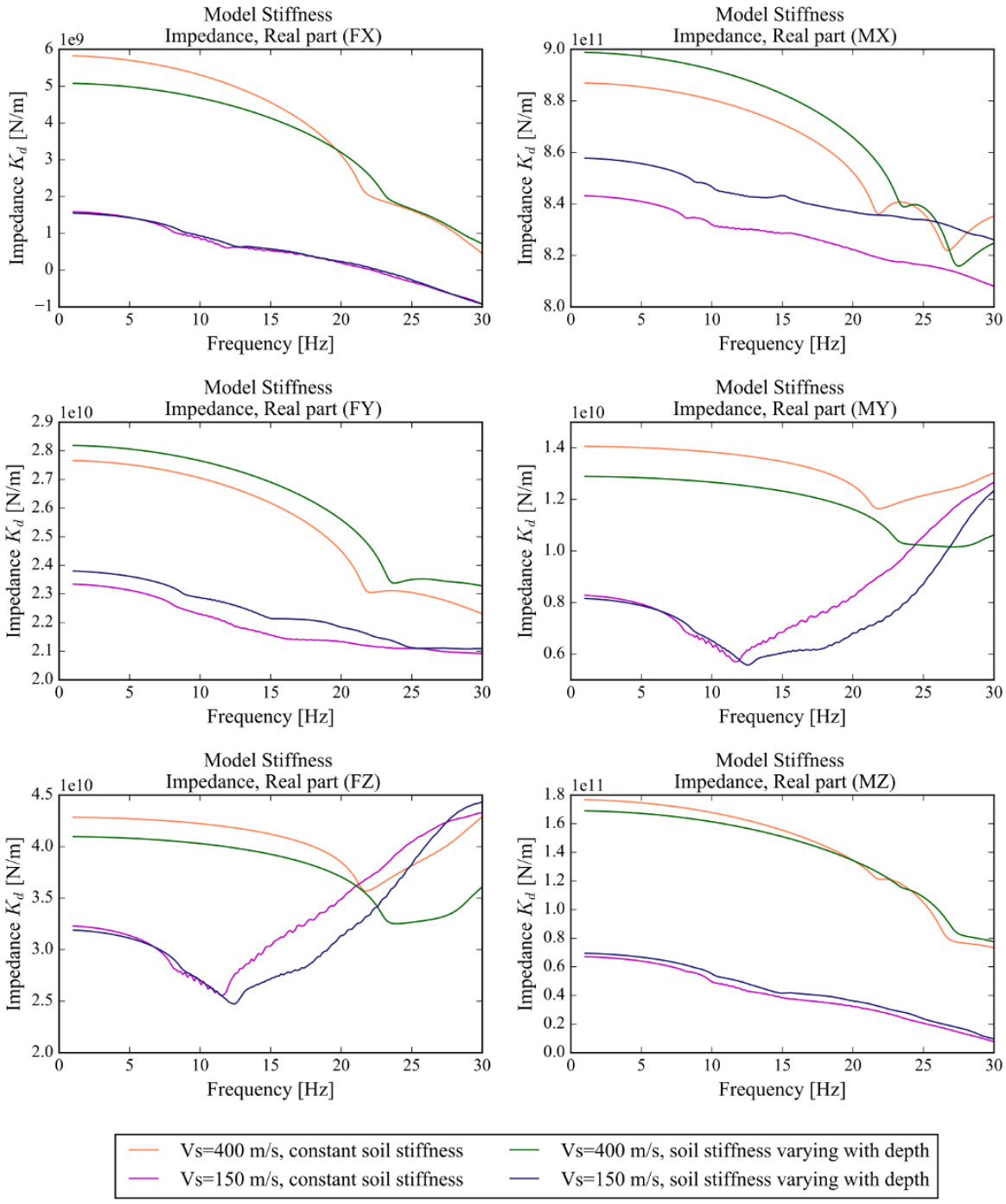

Figure 4.5: Dynamic stiffness for embankment models with varying stiffness and level of detail.

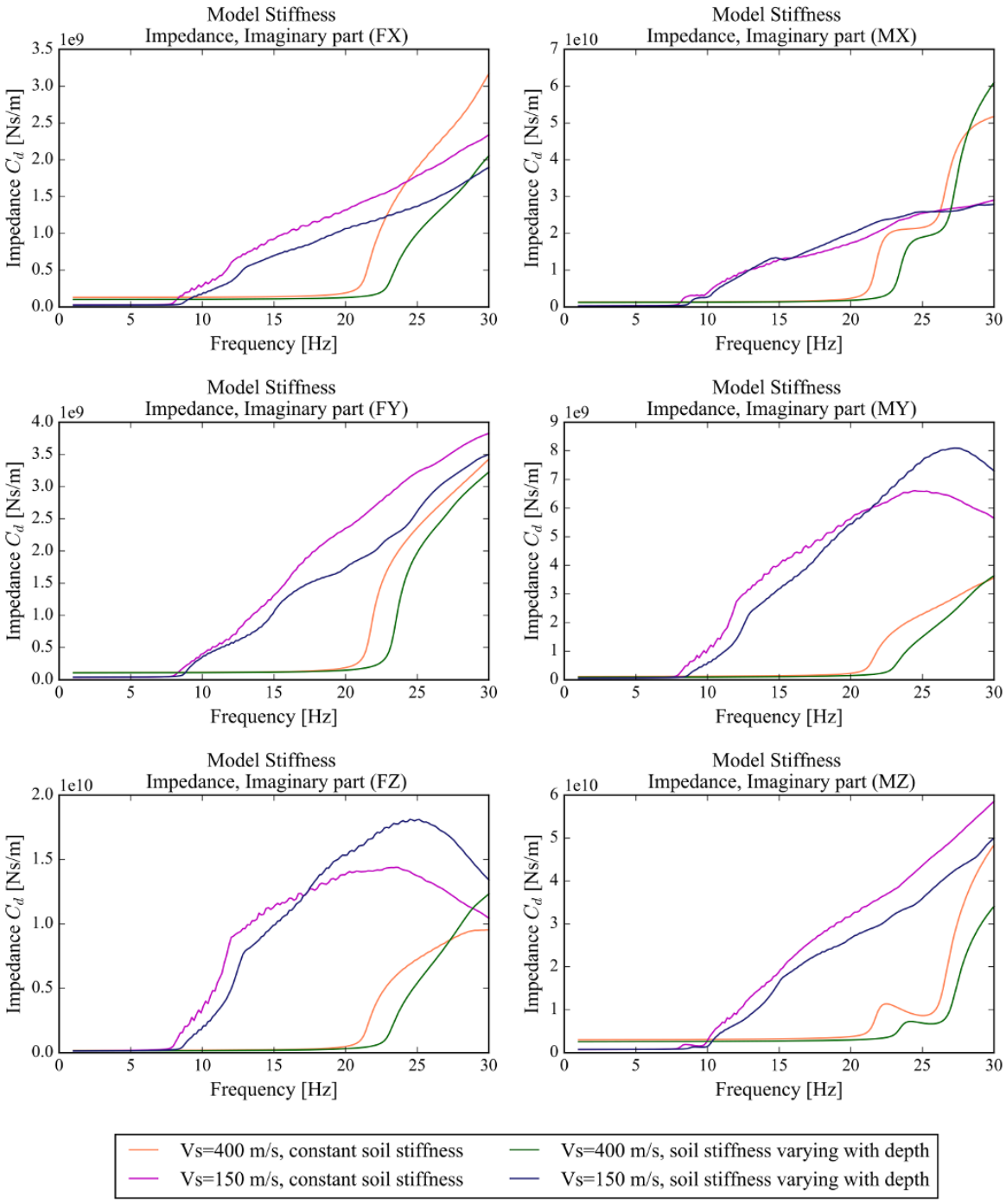

Figure 4.6: Dynamic damping for embankment models with varying stiffness and level of detail.

Ground stiffness

In figures 4.7 – 4.9, the receptance and the real and imaginary parts of the impedance are plotted for four different models: The embankment with prescribed translations in the bottom face, and three embankments on 5 meters deep ground soil plates of various stiffness. The embankment has a constant shear modulus of 40.5 MPa (v_s=150 m/s)

and the ground soil has a modulus corresponding to the values of half, same as, and double the shear wave speed of the embankment. The embankment with prescribed translations corresponds to an embankment on infinitely stiff bedrock.

A clear pattern can be seen in the real part impedance plots, being the dynamic stiffness increase with increased static ground stiffness G_0. An equally clear pattern cannot be seen in the imaginary part impedance plots. It can, however, be seen that the dynamic damping tend to decrease with increased static ground stiffness. In all plots, it seem as if the first natural frequency might differ with about 3 Hz when only comparing the models with ground soil plate.

When looking at the receptance for the FY-, FZ- and MX-directions, there seems to be an error in the plots for the embankment on bedrock, as the receptance seems constant for all frequencies. This is not the case, but a consequence of the receptance being many times smaller for this model compared to the others. The reason for this gets clear when looking at the dynamic stiffness in Figure 4.8, where the stiffness for the embankment on bedrock is several times higher than for the rest of the models. This indicates that there is a big difference between having a fixed foundation as the one on bedrock, and a foundation embedded in soil. This has previously been concluded by Ülker-Kaustell (2009). The differences are not as large when looking at the directions that induces bending in the weak direction of the bridge wall (FX and MY), which is more governed by the stiffness of the bridge wall.

In Appendix A, one can compare the impedance and receptance for the soil plates with the tree depths of 5, 10 and 15 meters. It is there observable that, the depth of the ground soil influence the dynamic stiffness somewhat, in the way that the stiffness decreases from the shallowest to the deepest soil plate. For some directions, these effects were scarcely visible, and for some directions, quite clear.

When increasing the ground stiffness, the solutions for the dynamic stiffness and damping seem to converge towards the infinitely stiff solution, reassuring the quality of both the small and the big models. This is visible in, for example, the real part of the impedance in the MY- and MZ-directions.

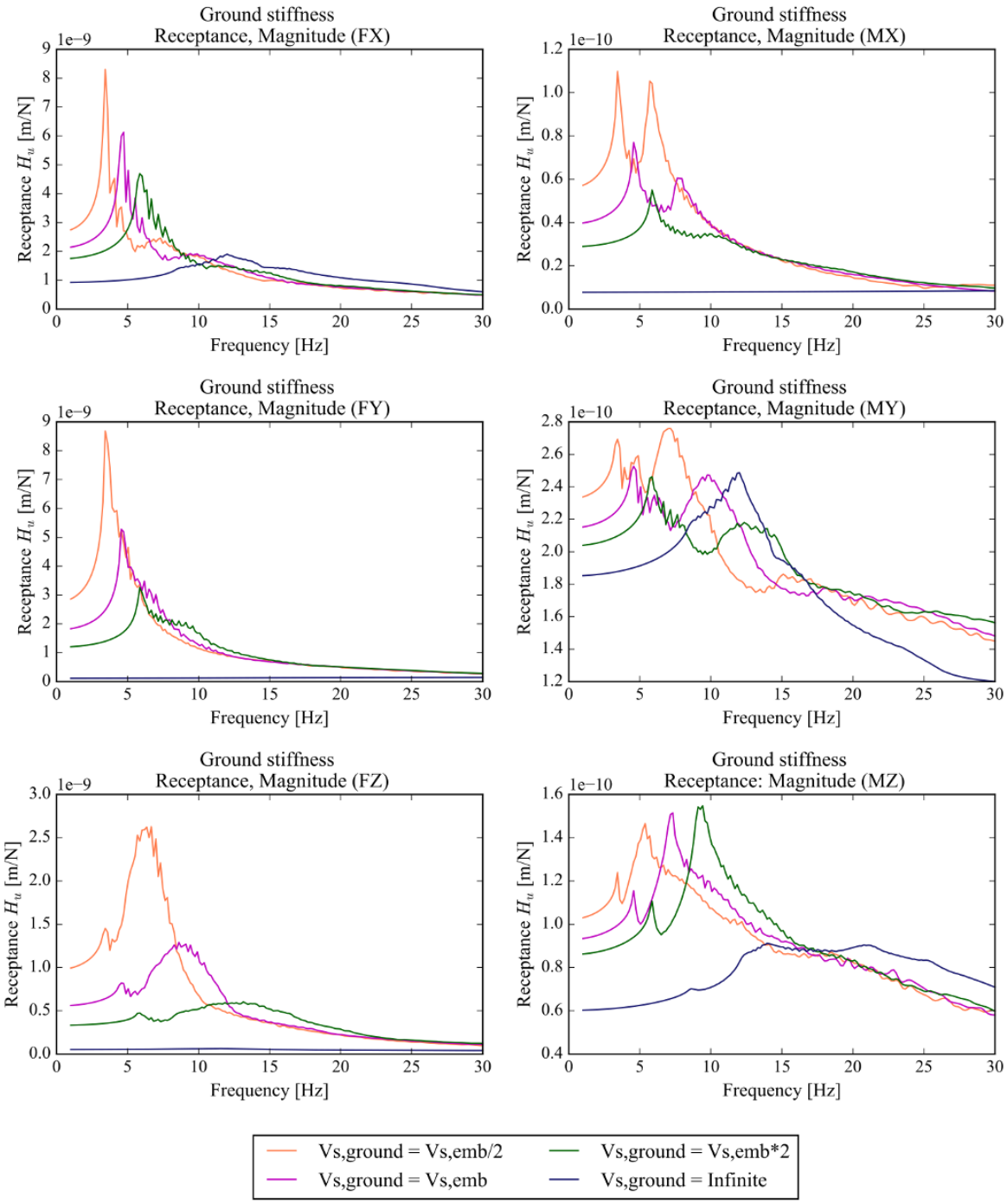

Figure 4.7: Receptance for the big models with varying ground soil stiffness and constant embankment soil stiffness.

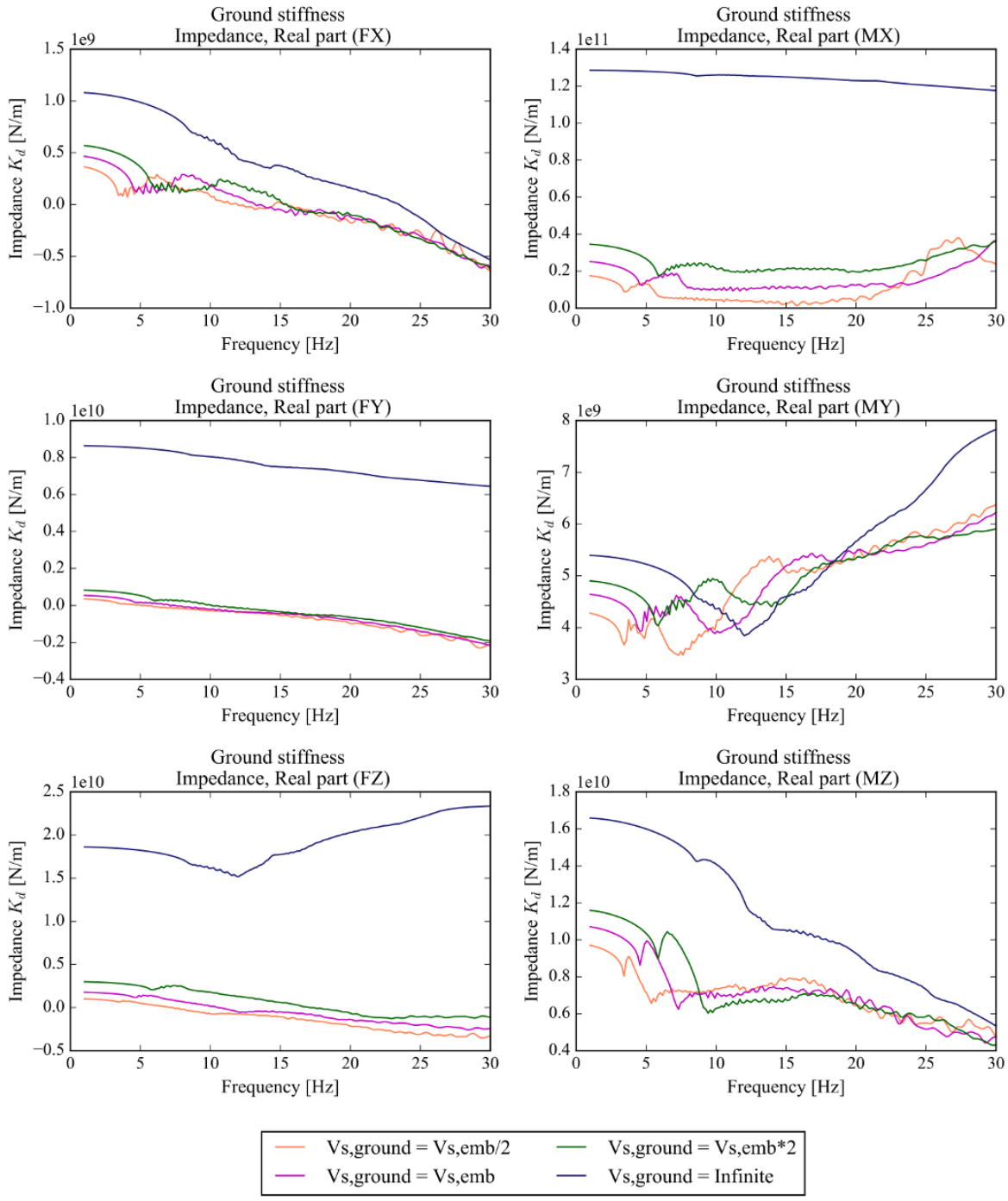

Figure 4.8: Dynamic stiffness for the big models with varying ground soil stiffness and constant embankment soil stiffness.

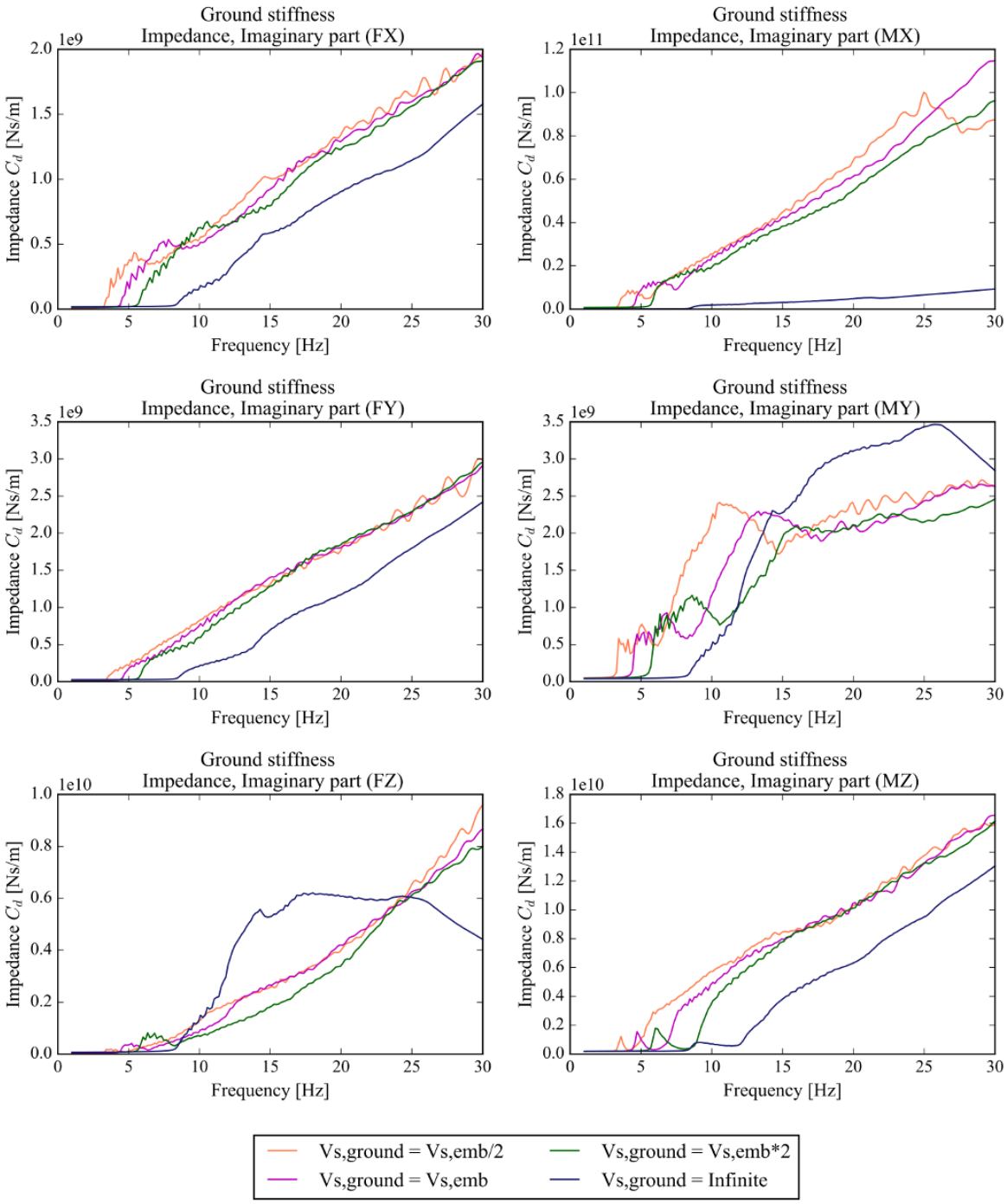

Figure 4.9: Dynamic damping for the big models with varying ground soil stiffness and constant embankment soil stiffness.

4.1.4 Depth of the model

In Figure 4.10, the receptance and impedances in the FX-directions are plotted for embankment models on 5, 10, and 15 meters of ground soil. The soil stiffness is constant, and set to the same as in the embankment. When increasing the depth, the

static stiffness of the ground soil decrease. This affects the dynamic damping in the same way. As in the previous comparison, when keeping the depth constant and increasing the shear modulus of the ground soil, the dynamic damping does not seem to be as affected as the dynamic stiffness. The resonance frequency seem to behave in the same manner as when increasing the shear modulus of the ground soil: deeper soil layer yields less stiffness and thereby a lower resonance frequency. The amplitude of the receptance at resonance frequency seems, however, to increase with the stiffness of the ground soil. This is opposite the behavior in the previous comparison, again making it complicated to draw any conclusions on how a bridge would respond in terms of vibration amplitudes due to the ground conditions.

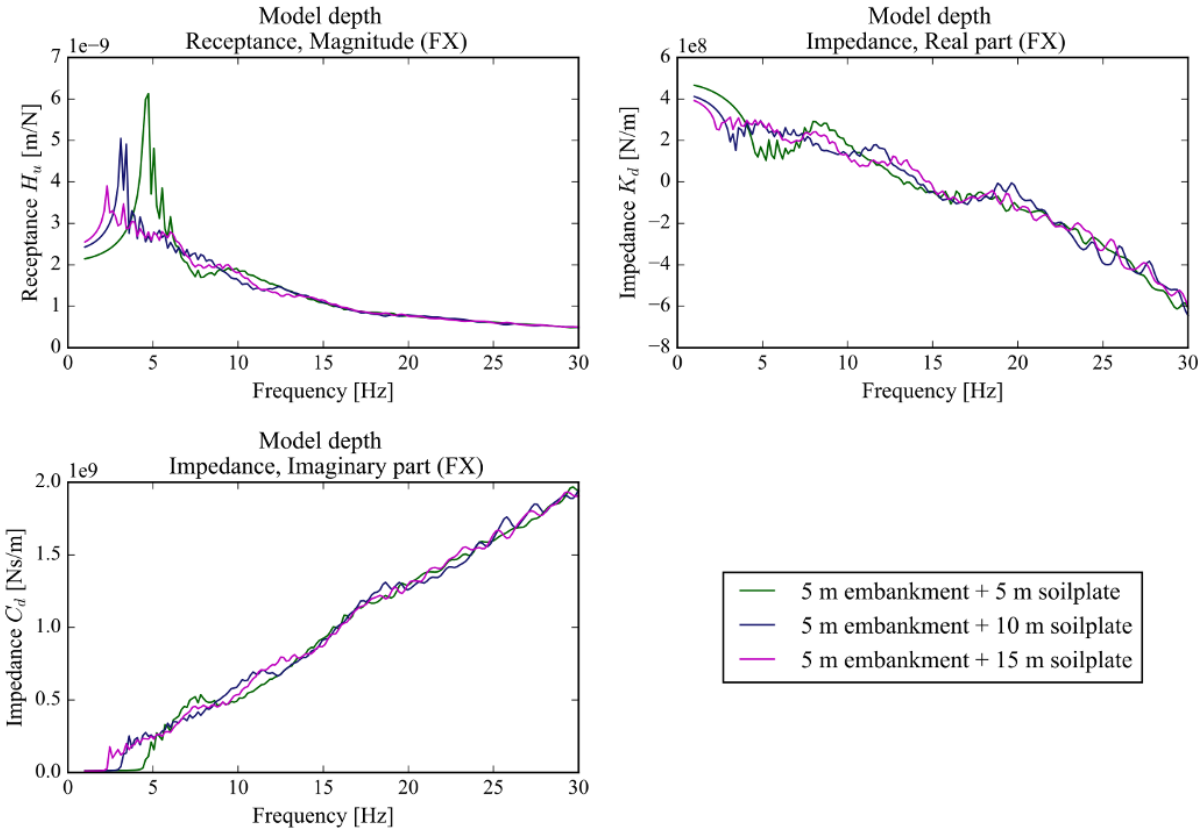

Figure 4.10: Receptance, real part impedance and imaginary part impedance for three models with embankment and circular soil plate.

Chapter 5

Discussion and further research

In this chapter, conclusions drawn from the work with this thesis are presented and discussed. The main aim of the thesis was to perform a parameter study on embankment models, whose quality were assured through convergence tests. This work was intended to provide a platform for future research by studying the effects which different modeling techniques can have. The results related to this aim are the impedance functions presented in Appendix A with the comparisons made in the previous chapter.

5.1 Conclusions

As stated in the previous chapter, only looking at the impedances in one direction at a time is not sufficient to draw conclusions about the bridge response to high-speed traffic. There are many assumptions made regarding material parameters, and possible errors in the models that need to be investigated. Further studies also need to be performed where the impedance functions are included in a bridge model, to see the real effects from all components combined. These models need further validation by comparing them to measurements. This model will in its turn rise new insecurities, for example the influence of the train-bridge interaction and possible errors in the bridge model. However, the impedance functions can give indications on how the bridge's accelerations would be affected by including SSI.

The main conclusions drawn from the work with this thesis will here be presented in list form, divided between the convergence study and the parameter study.

Convergence study

- For the embankment models in this thesis, HEX elements were shown to be beneficial compared to TET elements. The former ones tended to converge at a courser element size and allowed a larger bias ratio. The TIE constraint that had to be used in the soil to connect TET and HEX elements did not show to affect the wave propagation. Computational costs can therefore be reduced by using a structured mesh.
- The infinite boundary can effectively reduce the wave reflections at the boundary.
- A very large modeling domain is needed to reduce Rayleigh wave reflections.
- A large number of degrees of freedom are needed to model a shallow foundation embedded in soil. The number of d.o.f's in the model with embankment and ground soil plate in this thesis were $1.6\text{x}10^6$.

Parameter study

- Reconance frequencies are highly dependent on the embankment and ground soil stiffness.
- SSI contribute to the damping and stiffness of a structure. The damping increases after the first resonance frequency for all models tested in this thesis.
- A careful estimation of the shear modulus seems important to calculate the impedance functions with proper accuracy. Discrepancies were shown between the models with constant shear modulus and models with shear modulus increasing with depth.
- Wing walls yield more dynamic stiffness – and for most directions also more dynamic damping – to the structure.
- A two-tracked embankment seem to induce more dynamic stiffness and damping to a structure than a one-tracked.
- The dynamic stiffness is highly influenced by the ground conditions. The dynamic stiffness increase with the static stiffness of the soil, and decrease with the depth of the ground soil plate.
- The dynamic damping tend to decrease with increased ground soil stiffness.
- The foundation embedded in soil cannot be considered as fixed.

5.2 Discussion

Validity of the results

Several assumptions have been made in the modeling procedure in this thesis. Better understanding of how these assumptions influence the results need to be supplied through further research. The assumption of full interaction between the bridge wall and backfill soil requires that no sliding occur between the two mediums, which in its turn requires that the strains in the interface are sufficiently small. A control measurement on the strains in the volume closest to the bridge wall was not performed in this thesis due to lack of time. Measuring the strain rate is also important to ensure that the chosen material model with the rate-independent Kelvin solid is valid. All assumptions were made based on experiences gained in previous studies, but still need to be checked for the specific models within this thesis.

Due to time constraints, the same convergence tests that were carried out on the small models could not be made on the big models. The mesh of the ground soil plate may have been too course, resulting in more ripples in the impedance plots. The bias, making the elements increase in size towards the infinite boundary, were probably given a too large ratio. However, when plotting models with only embankment on bedrock with models on ground soil plate, the results seemed to converge towards the same solution when increasing the ground soil stiffness, ensuring that the big models were of good quality, if only with too large elements.

Discussion on the conclusions drawn from the study

Using the infinite elements on the model boundary reduced the wave reflections in the models. A very large modeling domain was however still needed to properly reduce the wave reflections that the infinite boundary could not handle. It would have been interesting to compare the effectiveness of the infinite boundary with other methods of discretizing the infinite extent of the embankment, for example the method of using an absorbing region, which has shown to demand a shorter modeling domain and thus reducing the computational cost.

How much influence a small increase in embankment stiffness has for the resonance frequencies could not be shown, as no values between the softest and the stiffest soil were tested. It was however indicated that the resonance frequency would increase even for a small increase in static stiffness. The resonance frequencies in the bridge-soil

structure depend on all geometry- and material parameters combined, and trustworthy predictions would demand a massive work with validating the models.

It was concluded that the shallow foundation could not be considered as fixed when embedded in soil, as the impedances in directions most vulnerable of the foundation's boundary conditions showed large deviations between the embankment on bedrock and embankment on ground soil plate. The movements of the foundation in the ground soil was, however, probably overestimated as the foundation was modeled without fill material.

5.3 Further research

To draw general conclusions that can give advice on how to best design the future high-speed railway bridges with SSI included, extensive research is needed.

Validation

The first step for research following the work in this thesis would be to validate the models used. An effort for doing this that was not included in this thesis due to time limits, is to check the strains in the embankment. The material model used is only valid up to a certain strain rate, and exceeding these limits could lead to unreliable results.

An effort for validating the conclusions drawn from analyzing the impedance plots, would be to apply the functions to bridge models and compare the response from the train load models HSLMA1-10 according to Eurocode. The effects from the soil's dynamic stiffness and damping can then be viewed in terms of acceleration amplitudes in the bridge deck, and be compared to the response without SSI.

The accelerations in the bridge deck then need to be compared to controlled measurements on a real bridge. Field measurements of the soil conditions in the actual embankment and ground beneath the bridge need to be conducted, and applied in updated SSI models. Otherwise, a bridge with soil parameters as close to the ones used in this thesis need to be found, and used to validate against.

Continued parameter screening

The effects of SSI need to be investigated on more soil types, assumptions and geometries. The shear modulus may be modeled dependent on depth according to different empirical formulae than the one used in this thesis. Comparing these methods with each other can give important understanding on the importance of a properly

modeled shear modulus. The assumption of full interaction between the bridge wall and the embankment can be investigated by comparing with models including different amount of friction in the interface.

As the stiffness of the concrete wall showed to be of great importance, a study on the influence that the geometrical entities of the wall can have, should be conducted. Established methods for increasing the bending stiffness of a wall, for example with wing walls parallel to the railway tracks, or with buttresses behind the bridge wall, can be optimized for the specific purpose of decreasing the vibrations in the bridge deck. If the vibrations of the bridge can be reduced by increasing the stiffness of the bridge wall, this could be a simple effort to design future bridges to hold for high speed railway traffic. A parameter screening is therefore suggested, where the impedances are compared for various types of bridge wall geometries.

Furthermore, the transition zones close to the bridge wall need to be investigated. Usually, stiffer filling material is placed in a volume close to the bridge wall to make the transition between the concrete and soil less contrasted. This was not considered in this thesis, but as the stiffness of the concrete wall showed to have a large influence, one can expect the transition zones to have too.

In the future, it is desired that the methodology used in this thesis will lead to a more realistic, yet conservative method for including SSI when analyzing the dynamics of bridges according to building codes.

References

Andersen, L. V. (2006). *Linear Elastodynamic Analysis - DCE Lecture Notes No. 3.* Aalborg: Department of Civil Enginering, Aalborg University.

Andersson, A., & Karoumi, R. (2015). Dynamics of railway bridges, analysis and verification by field tests. *EVACES'15, 6th International Conference On Experimental Vibration Analysis For Civil Engineering Structures, Vol. 24*, pp. 01001-p.1 - 01001-p.12. Zurich.

BaTMan. (2015). *BaTMan - Bridge and Tunnel Management.* Retrieved from https://batman.trafikverket.se/

Bengtsson, P.-E., Larsson, R., Moritz, L., & Möller, B. (2000). *Geodynamik i Praktiken.* Linköping: Statens Geotekniska Institut.

Chopra, A. K. (2014). *Dynamics of Structures - Theory and Applications to Earthquake Engineering* (4th ed.). Prentice Hall.

Cooley, J., & Tukey, J. (1965). An Algorithm for the Machine Calculation of Complex Fourier Series. In *Mathematics of Computation 19* (pp. 297-301).

Dassault Systèmes. (2012). *Abaqus Analysis 6.12 User's Manual.* Simulia Inc.

Gazetas, G. (1991). In *Foundation Engineering handbook* (2nd ed., pp. 553-593). New York: Van Nostrand Reinhold.

Hardin, B., & Drnevich, V. (1972). Shear modulus and damping in soils: Design equations and curves. *Journal of the Soil Mechanics and Foundations Division, 98*(7), 667-692.

Hewlett-Packard. (2000). *The Fundamentals of Signal Analysis - Application Note 243.* Agilient Technologies.

Ishihara, K. (1996). *Soil Bahaviour in Earthquake Geotechnics.* Oxford: Oxford University Press.

Kausel, E. (2005). *Fundamental Solutions in Elastodynamics.* New York: Cambridge University Press.

Lunarc. (2016a). *Lund University - Lunarc.* Retrieved from http://www.lunarc.lu.se/

Lunarc. (2016b). *Lunarc Documentation pages.* Retrieved from http://lunarc-documentation.readthedocs.io/en/latest/

Lysmer, J. (1978). *Analytical Procedure in Soil Dynamics.* Earthquake Engineering Research Center, University of California.

Lysmer, J., & Kuhlemeyer, R. L. (1969). Finite dynamic model for infinite media. *Journal of the Engineering Mechanics Division, 95*(4).

Ottosen, N., & Petersson, H. (1992). *Inroduction to the Finite Element Method.* Harlow: Prentice Hall.

SGI-i1. (2008). *Jords Egenskaper.* Linköping: Swedish Geotechnical Institute.

SS-EN 1990. (2002). *Eurocode - Basis of Structural Design.*

SS-EN 1991-2. (2003). *Eurocode 1: Actions on structures - Part 2: Traffic loads on bridges.*

Takemiya, H., & Bian, X. (2007). Shinkansen high-speed train induced ground vibrations in view of viaduct-ground interaction. *Soil Dynamics and Earthquake Engineering 27*, 506-520.

TRVK Bro. (2011). *TRVK Bro 11.* ISBN 978-91-7467-153-7.

Ülker-Kaustell, M. (2009). *Some aspects of the dynamic soil-structure interaction of a portal frame bridge.* Royal Institute of Technology (KTH). TRITA-BKN. Licentiate Thesis 102.

Zhang, J.-M., Shamoto, Y., & Tokimatsu, K. (1998). Evaluation of Earth Pressure Under Any Lateral Deformation. *Soils and Foundations, 38*(1), 15-33.

Zienkiewicz, O. C., & Taylor, R. L. (2000). *Finite Element Method: Volume 1 - The Basis* (5th ed.). Oxford: Butterworth-Heineman.

Östlund, J. (2016). *Soil-structure Interaction of End-frames for High-speed Railway Bridges.* Royal Institute of Technology (KTH). TRITA-BKN. Master's thesis 484.

Appendix A
- Impedance functions

Presented in this appendix are the diagrams with receptance and impedance that are the results from the parameter study performed in this thesis. In Table A. 1, the geometrical and material properties of each model in the parameter study are described, along with references to the corresponding figures. The first four models are the ones with an embankment on bedrock, where the diagrams for each model number are presented for the four levels of detail. The last three models are the ones with embankment and ground soil plate with varying ground stiffness and depth.

Table A. 1: Parameters of each model in the parameter study. Each model number refers to three figures with diagrams for receptance, real part of the impedance and imaginary part of the impedance, including all 6 load components.

Small models	$\mathbf{v_s}$ **[m/s]**	$\mathbf{w_{emb}}$ **[m]**	$\mathbf{H_{emb}}$ **[m]**	**Figures**
Model number				
1	400	12	5	A.1 - A.3
2	150	12	5	A.4 - A.6
3	400	6	5	A.7 - A.9
4	150	6	5	A.10 - A.12
Big models	$\mathbf{v_s}$ **embankment [m/s]**	$\mathbf{v_s}$ **ground soil [m/s]**	$\mathbf{H_{soilplate}}$ **[m]**	**Figures**
Model number				
5	150	75/150/300	5	A.13 - A.15
6	150	75/150/300	10	A.16 - A.18
7	150	75/150/300	15	A.19 - A.21

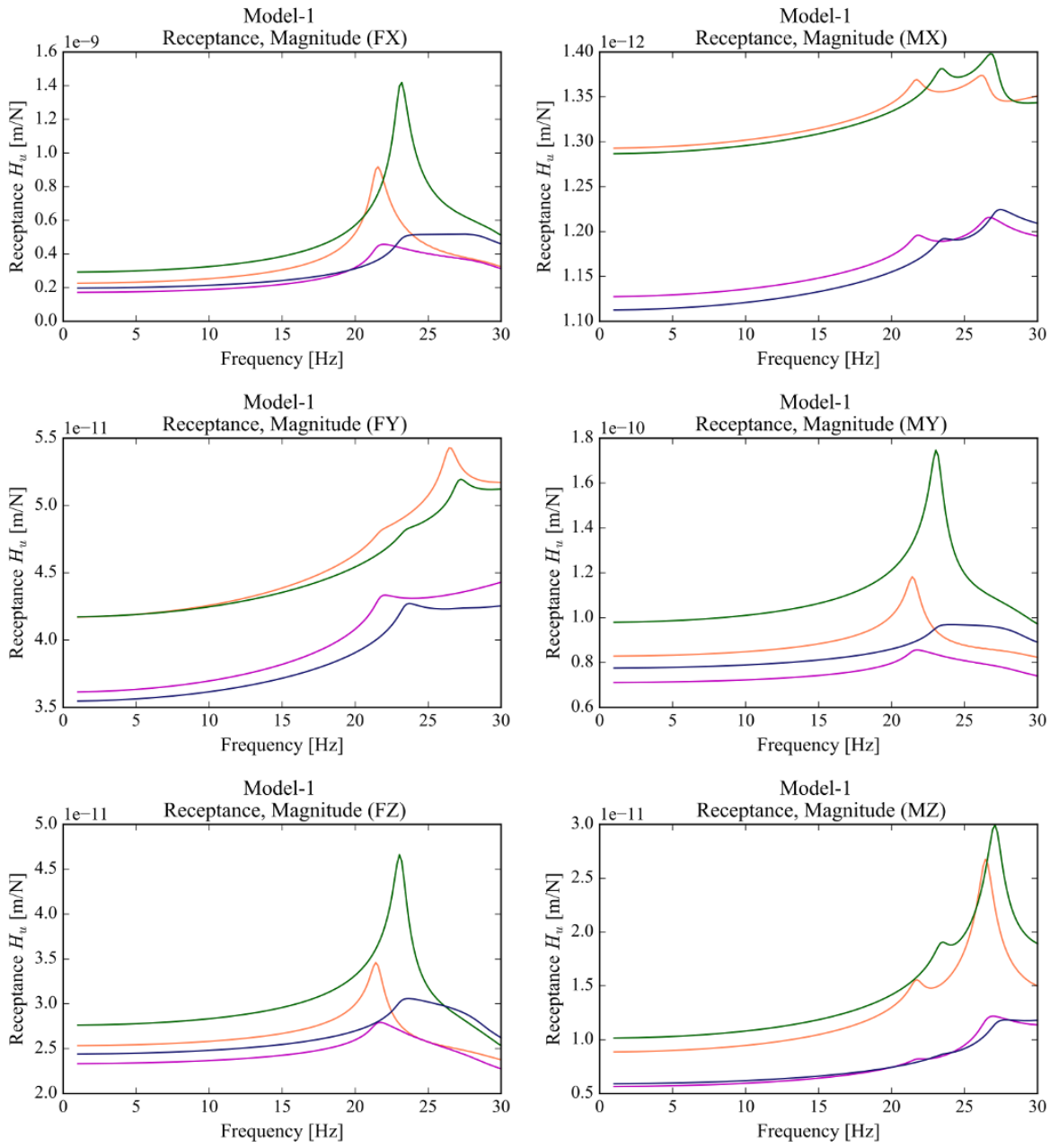
Model-1
Receptance, Magnitude (FX)
1e−9
Receptance H_u [m/N]
Frequency [Hz]
Model-1
Receptance, Magnitude (MX)
1e−12
Receptance H_u [m/N]
Frequency [Hz]
Model-1
Receptance, Magnitude (FY)
1e−11
Receptance H_u [m/N]
Frequency [Hz]
Model-1
Receptance, Magnitude (MY)
1e−10
Receptance H_u [m/N]
Frequency [Hz]
Model-1
Receptance, Magnitude (FZ)
1e−11
Receptance H_u [m/N]
Frequency [Hz]
Model-1
Receptance, Magnitude (MZ)
1e−11
Receptance H_u [m/N]
Frequency [Hz]
Homogenous soil, no wing walls
Homogenous soil, wing walls included
Layered soil, no wing walls
Layered soil, wing walls included

Figure A. 1

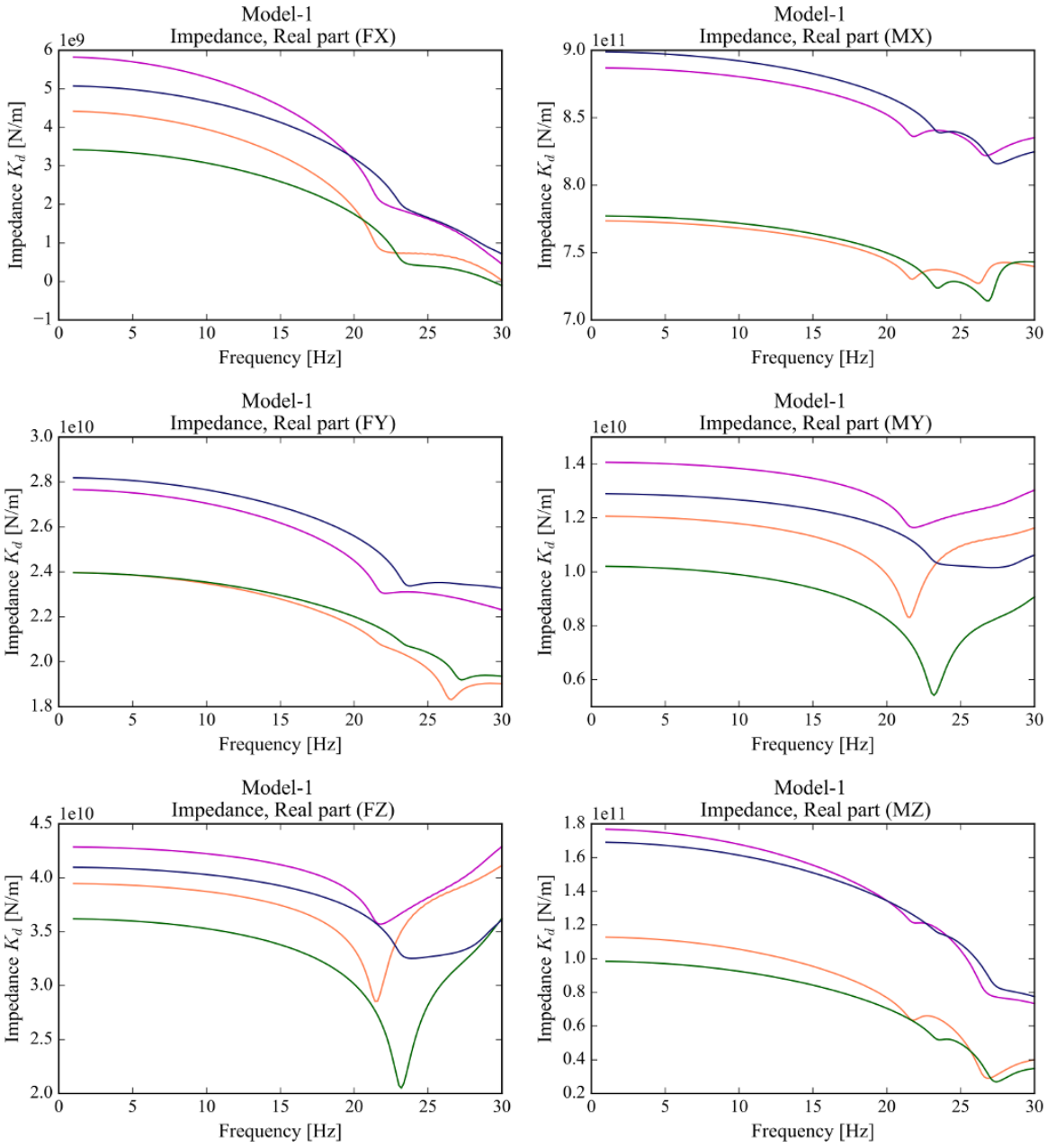
Model-1
Impedance, Real part (FX)
1e9
Impedance K_d [N/m]
Frequency [Hz]
Model-1
Impedance, Real part (MX)
1e11
Impedance K_d [N/m]
Frequency [Hz]
Model-1
Impedance, Real part (FY)
1e10
Impedance K_d [N/m]
Frequency [Hz]
Model-1
Impedance, Real part (MY)
1e10
Impedance K_d [N/m]
Frequency [Hz]
Model-1
Impedance, Real part (FZ)
1e10
Impedance K_d [N/m]
Frequency [Hz]
Model-1
Impedance, Real part (MZ)
1e11
Impedance K_d [N/m]
Frequency [Hz]
Homogenous soil, no wing walls
Homogenous soil, wing walls included
Layered soil, no wing walls
Layered soil, wing walls included

Figure A. 2

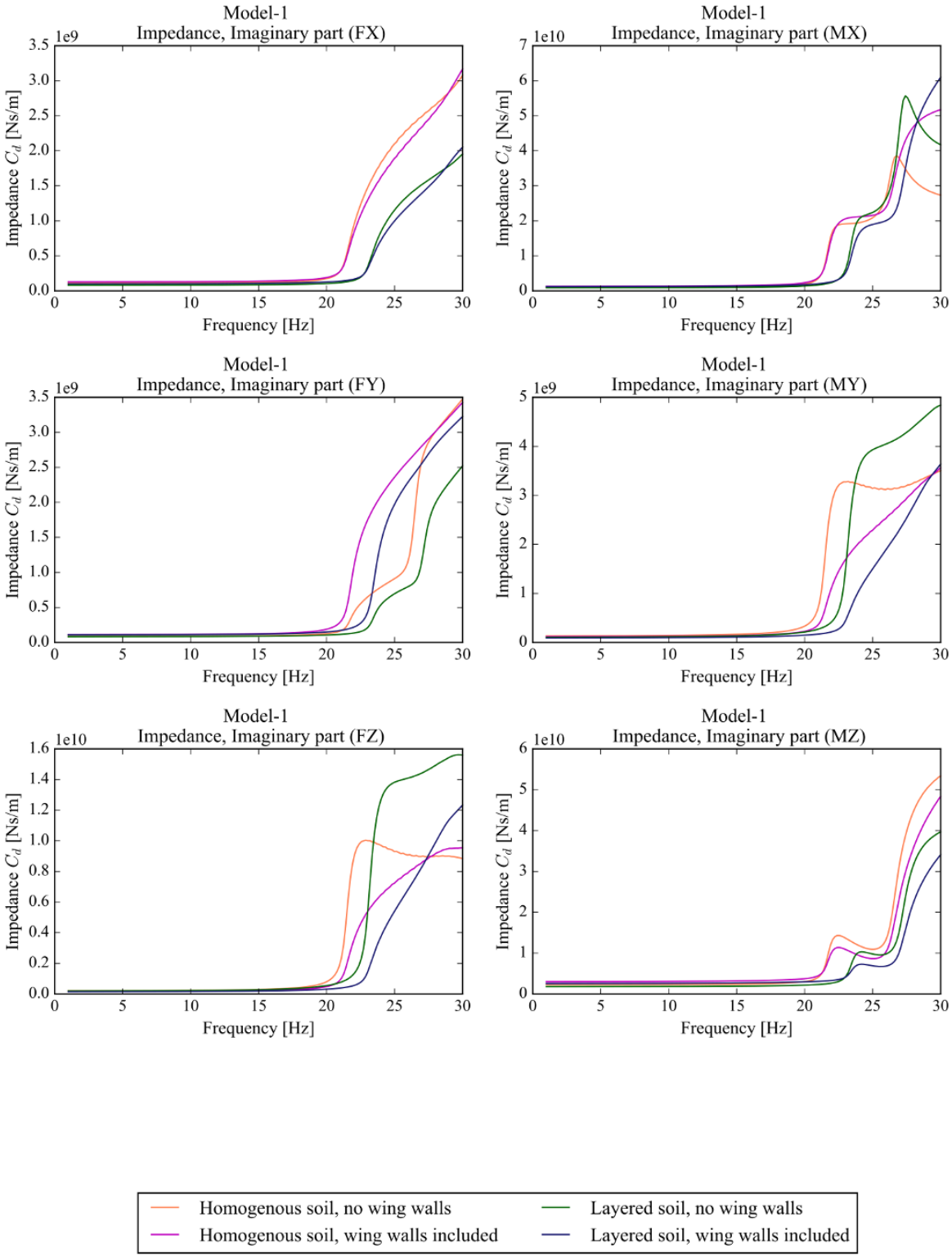
Model-1
Impedance, Imaginary part (FX)
1e9
Impedance C_d [Ns/m]
Frequency [Hz]
Model-1
Impedance, Imaginary part (MX)
1e10
Impedance C_d [Ns/m]
Frequency [Hz]
Model-1
Impedance, Imaginary part (FY)
1e9
Impedance C_d [Ns/m]
Frequency [Hz]
Model-1
Impedance, Imaginary part (MY)
1e9
Impedance C_d [Ns/m]
Frequency [Hz]
Model-1
Impedance, Imaginary part (FZ)
1e10
Impedance C_d [Ns/m]
Frequency [Hz]
Model-1
Impedance, Imaginary part (MZ)
1e10
Impedance C_d [Ns/m]
Frequency [Hz]
Homogenous soil, no wing walls
Homogenous soil, wing walls included
Layered soil, no wing walls
Layered soil, wing walls included

Figure A. 3

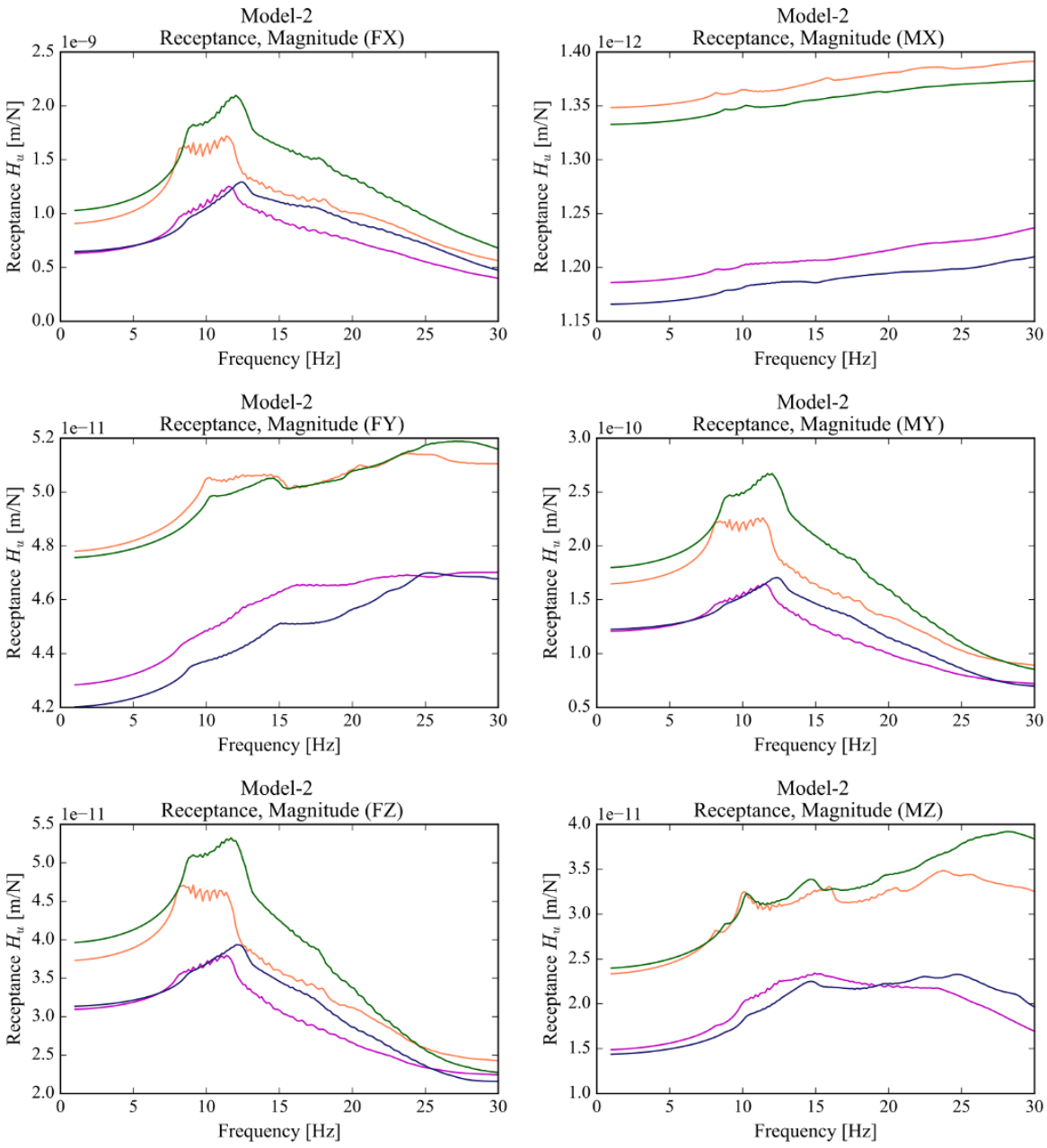
Model-2
Receptance, Magnitude (FX)
1e−9
Receptance H_u [m/N]
Frequency [Hz]
Model-2
Receptance, Magnitude (MX)
1e−12
Receptance H_u [m/N]
Frequency [Hz]
Model-2
Receptance, Magnitude (FY)
1e−11
Receptance H_u [m/N]
Frequency [Hz]
Model-2
Receptance, Magnitude (MY)
1e−10
Receptance H_u [m/N]
Frequency [Hz]
Model-2
Receptance, Magnitude (FZ)
1e−11
Receptance H_u [m/N]
Frequency [Hz]
Model-2
Receptance, Magnitude (MZ)
1e−11
Receptance H_u [m/N]
Frequency [Hz]
Homogenous soil, no wing walls
Homogenous soil, wing walls included
Layered soil, no wing walls
Layered soil, wing walls included

Figure A. 4

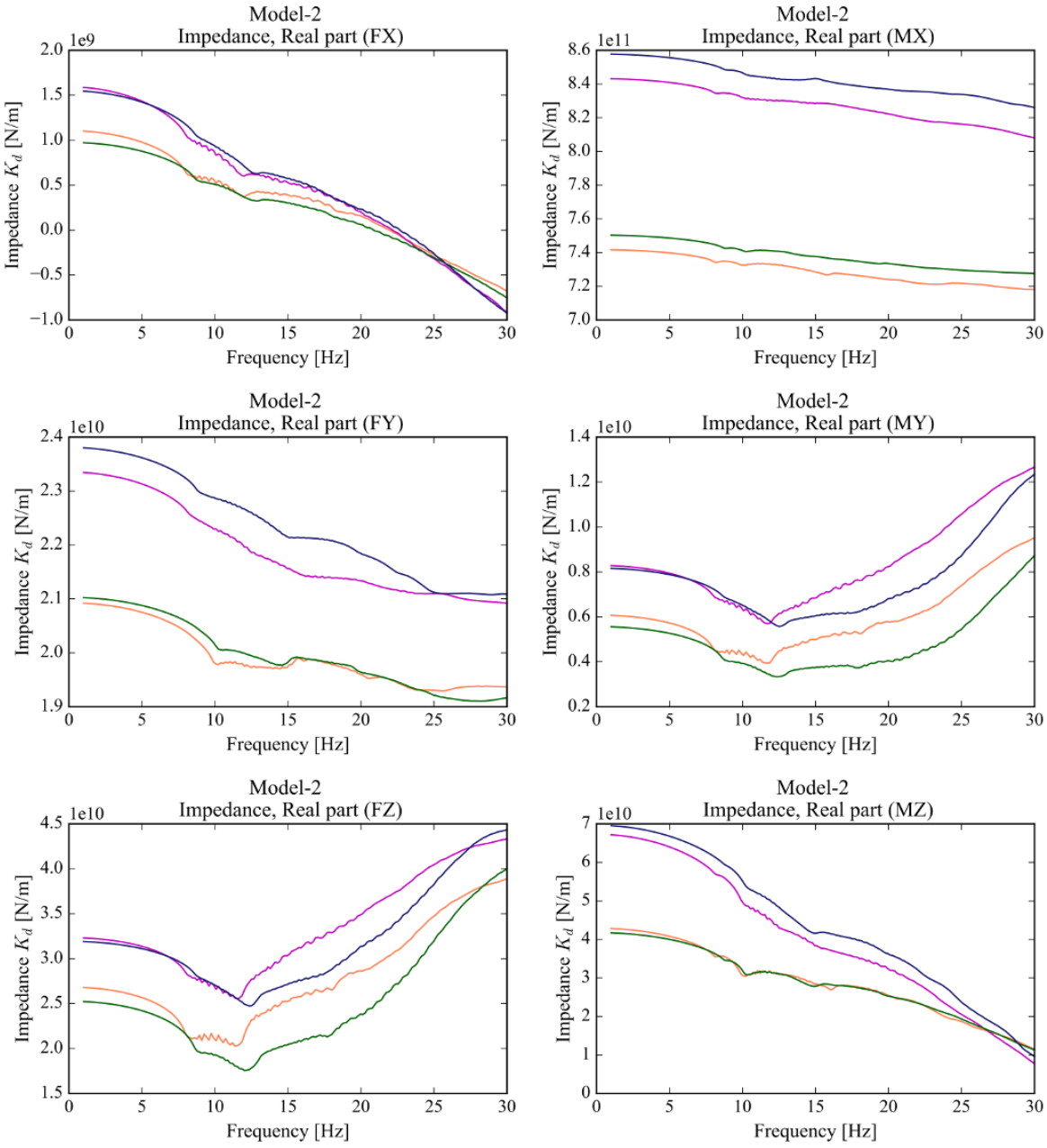
Model-2
Impedance, Real part (FX)
1e9
Impedance K_d [N/m]
Frequency [Hz]
Model-2
Impedance, Real part (MX)
1e11
Impedance K_d [N/m]
Frequency [Hz]
Model-2
Impedance, Real part (FY)
1e10
Impedance K_d [N/m]
Frequency [Hz]
Model-2
Impedance, Real part (MY)
1e10
Impedance K_d [N/m]
Frequency [Hz]
Model-2
Impedance, Real part (FZ)
1e10
Impedance K_d [N/m]
Frequency [Hz]
Model-2
Impedance, Real part (MZ)
1e10
Impedance K_d [N/m]
Frequency [Hz]
Homogenous soil, no wing walls
Homogenous soil, wing walls included
Layered soil, no wing walls
Layered soil, wing walls included

Figure A. 5

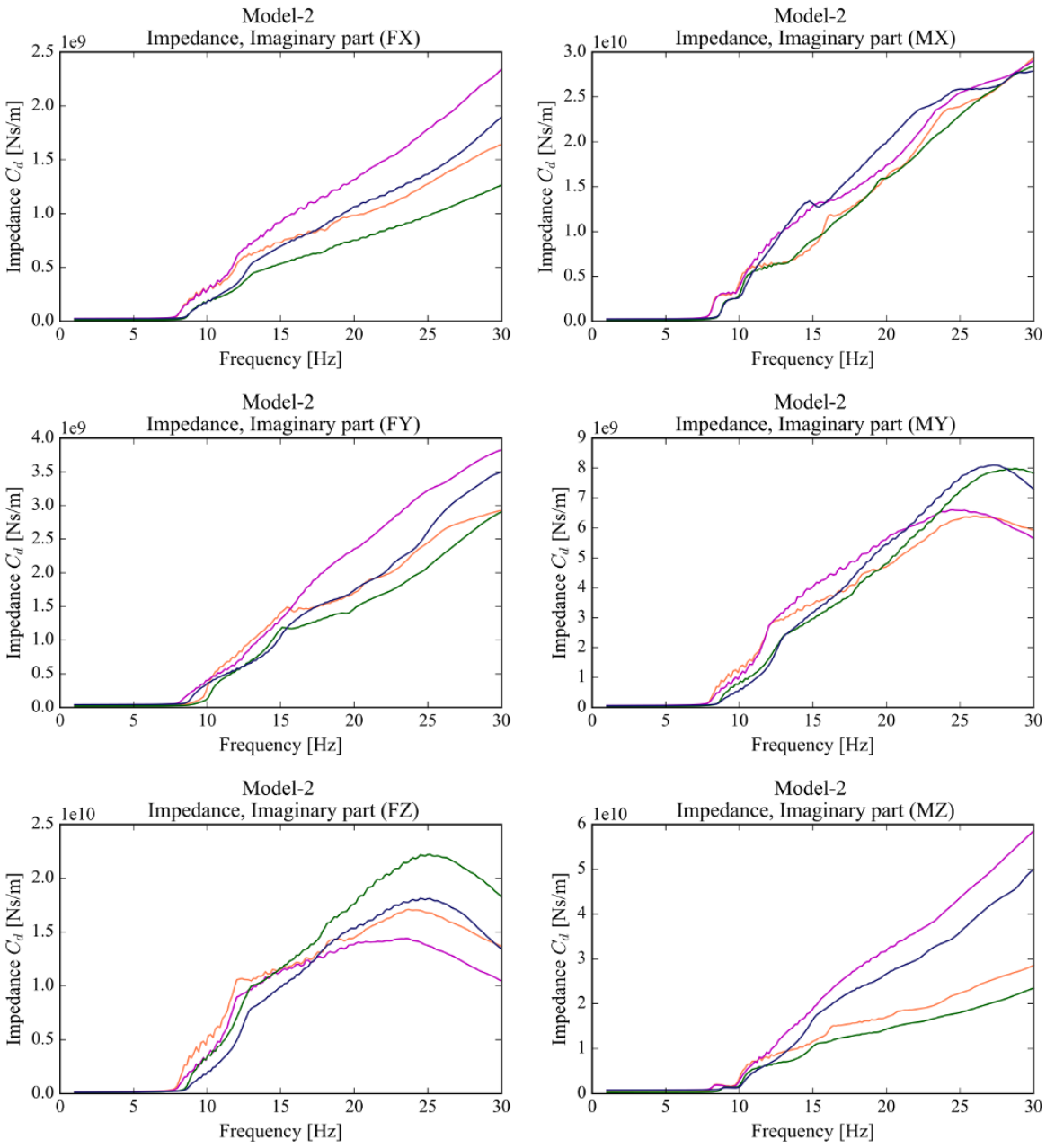
Model-2
Impedance, Imaginary part (FX)
1e9
Impedance C_d [Ns/m]
Frequency [Hz]
Model-2
Impedance, Imaginary part (MX)
1e10
Impedance C_d [Ns/m]
Frequency [Hz]
Model-2
Impedance, Imaginary part (FY)
1e9
Impedance C_d [Ns/m]
Frequency [Hz]
Model-2
Impedance, Imaginary part (MY)
1e9
Impedance C_d [Ns/m]
Frequency [Hz]
Model-2
Impedance, Imaginary part (FZ)
1e10
Impedance C_d [Ns/m]
Frequency [Hz]
Model-2
Impedance, Imaginary part (MZ)
1e10
Impedance C_d [Ns/m]
Frequency [Hz]
Homogenous soil, no wing walls
Homogenous soil, wing walls included
Layered soil, no wing walls
Layered soil, wing walls included

Figure A. 6

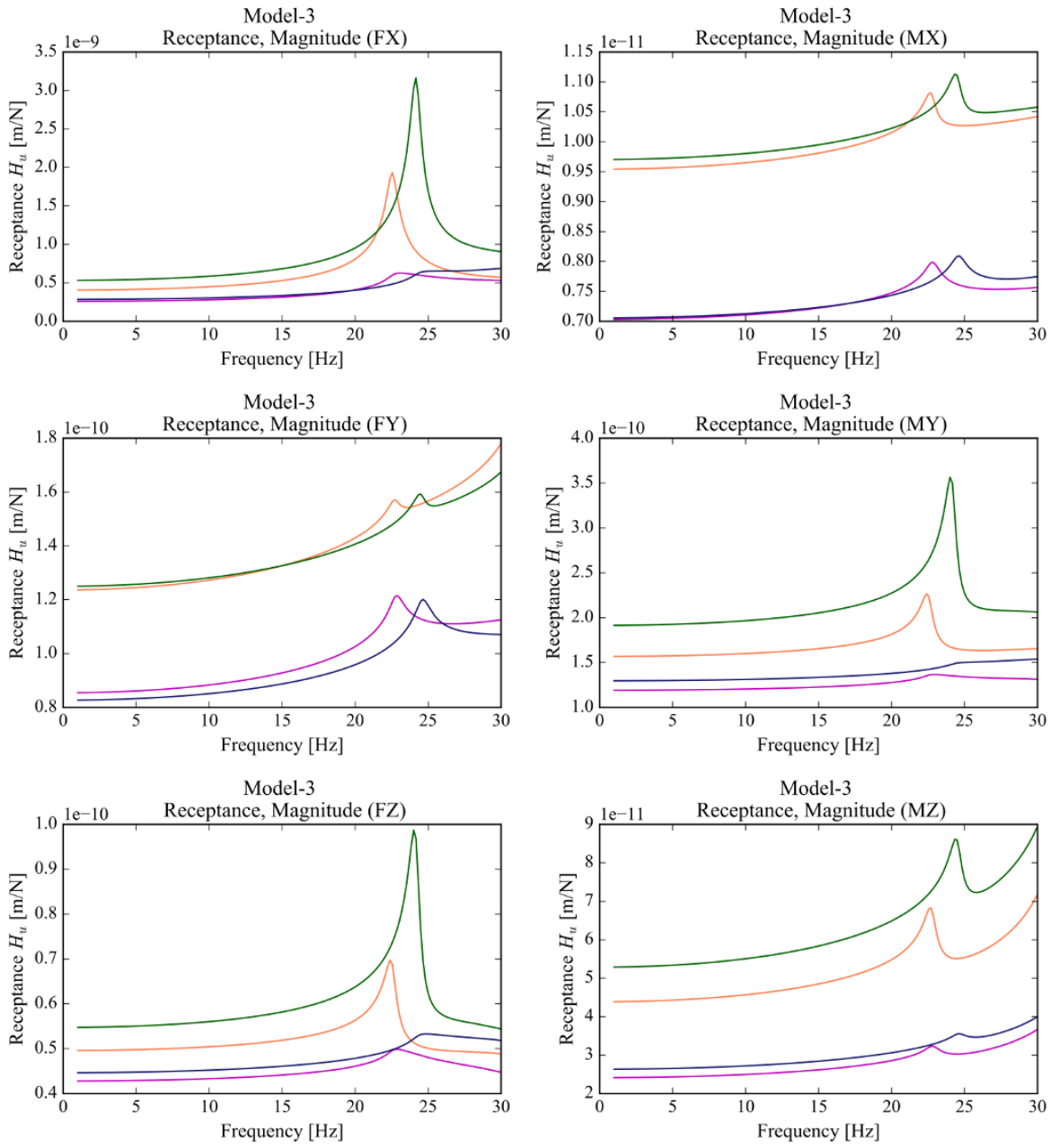
Model-3
Receptance, Magnitude (FX)
1e−9
Receptance H_u [m/N]
Frequency [Hz]
Model-3
Receptance, Magnitude (MX)
1e−11
Receptance H_u [m/N]
Frequency [Hz]
Model-3
Receptance, Magnitude (FY)
1e−10
Receptance H_u [m/N]
Frequency [Hz]
Model-3
Receptance, Magnitude (MY)
1e−10
Receptance H_u [m/N]
Frequency [Hz]
Model-3
Receptance, Magnitude (FZ)
1e−10
Receptance H_u [m/N]
Frequency [Hz]
Model-3
Receptance, Magnitude (MZ)
1e−11
Receptance H_u [m/N]
Frequency [Hz]
Homogenous soil, no wing walls
Homogenous soil, wing walls included
Layered soil, no wing walls
Layered soil, wing walls included

Figure A. 7

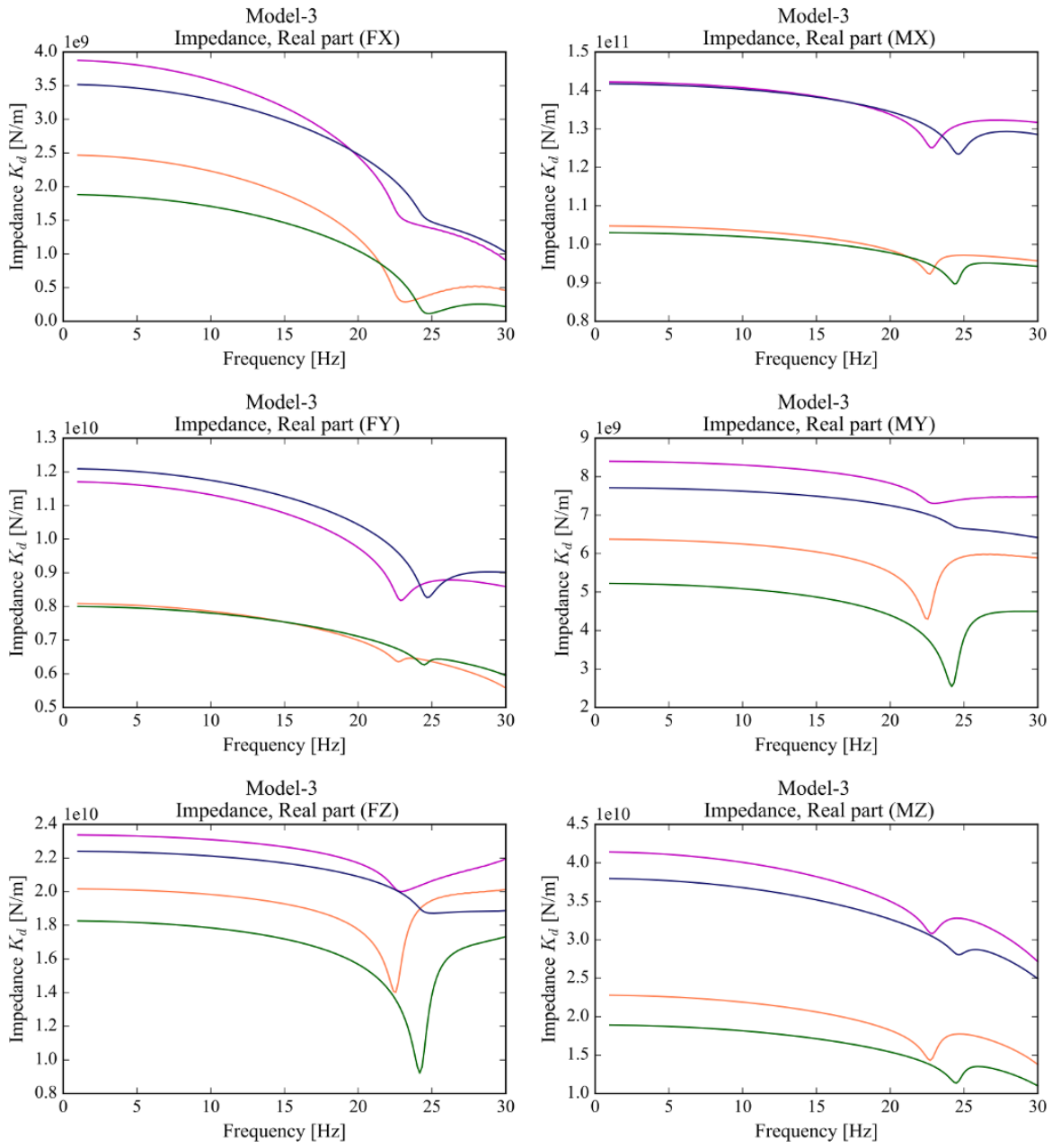
Model-3
Impedance, Real part (FX)
1e9
Impedance K_d [N/m]
Frequency [Hz]
Model-3
Impedance, Real part (MX)
1e11
Impedance K_d [N/m]
Frequency [Hz]
Model-3
Impedance, Real part (FY)
1e10
Impedance K_d [N/m]
Frequency [Hz]
Model-3
Impedance, Real part (MY)
1e9
Impedance K_d [N/m]
Frequency [Hz]
Model-3
Impedance, Real part (FZ)
1e10
Impedance K_d [N/m]
Frequency [Hz]
Model-3
Impedance, Real part (MZ)
1e10
Impedance K_d [N/m]
Frequency [Hz]
Homogenous soil, no wing walls
Homogenous soil, wing walls included
Layered soil, no wing walls
Layered soil, wing walls included

Figure A. 8

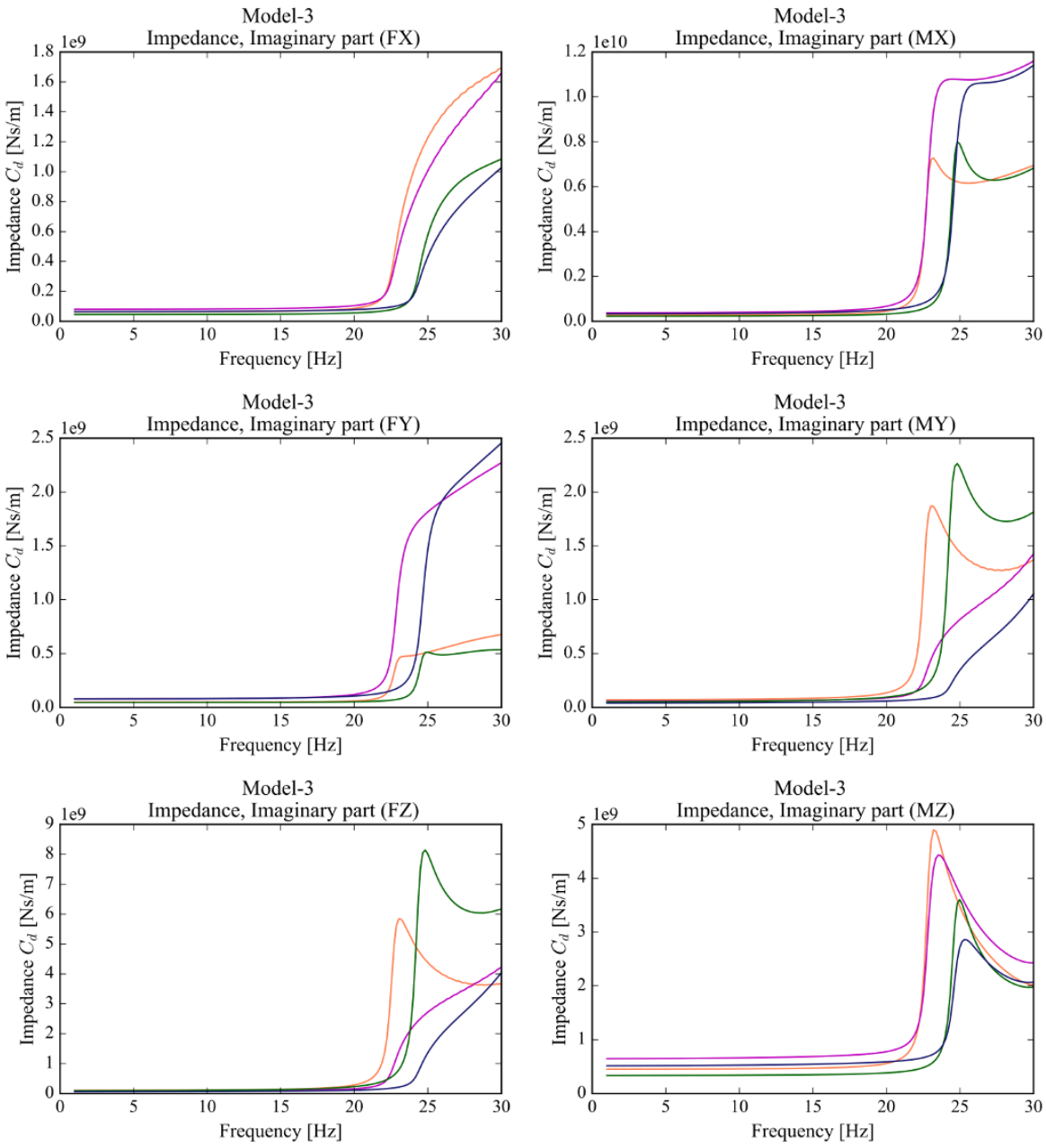
Model-3
Impedance, Imaginary part (FX)
1e9
Impedance C_d [Ns/m]
Frequency [Hz]
Model-3
Impedance, Imaginary part (MX)
1e10
Impedance C_d [Ns/m]
Frequency [Hz]
Model-3
Impedance, Imaginary part (FY)
1e9
Impedance C_d [Ns/m]
Frequency [Hz]
Model-3
Impedance, Imaginary part (MY)
1e9
Impedance C_d [Ns/m]
Frequency [Hz]
Model-3
Impedance, Imaginary part (FZ)
1e9
Impedance C_d [Ns/m]
Frequency [Hz]
Model-3
Impedance, Imaginary part (MZ)
1e9
Impedance C_d [Ns/m]
Frequency [Hz]
Homogenous soil, no wing walls
Homogenous soil, wing walls included
Layered soil, no wing walls
Layered soil, wing walls included

Figure A. 9

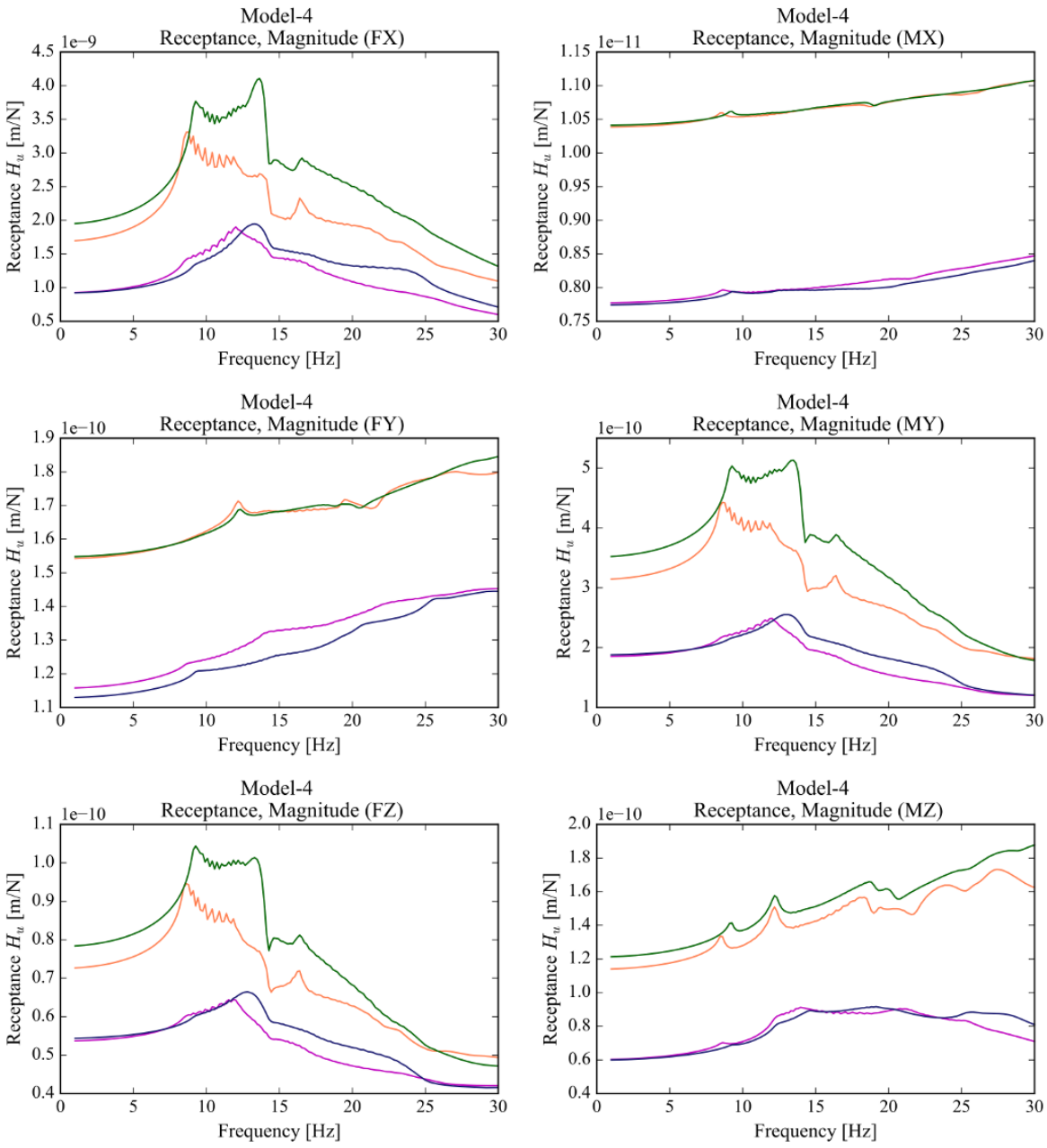
Model-4
Receptance, Magnitude (FX)
1e−9
Receptance H_u [m/N]
Frequency [Hz]
Model-4
Receptance, Magnitude (MX)
1e−11
Receptance H_u [m/N]
Frequency [Hz]
Model-4
Receptance, Magnitude (FY)
1e−10
Receptance H_u [m/N]
Frequency [Hz]
Model-4
Receptance, Magnitude (MY)
1e−10
Receptance H_u [m/N]
Frequency [Hz]
Model-4
Receptance, Magnitude (FZ)
1e−10
Receptance H_u [m/N]
Frequency [Hz]
Model-4
Receptance, Magnitude (MZ)
1e−10
Receptance H_u [m/N]
Frequency [Hz]
Homogenous soil, no wing walls
Homogenous soil, wing walls included
Layered soil, no wing walls
Layered soil, wing walls included

Figure A. 10

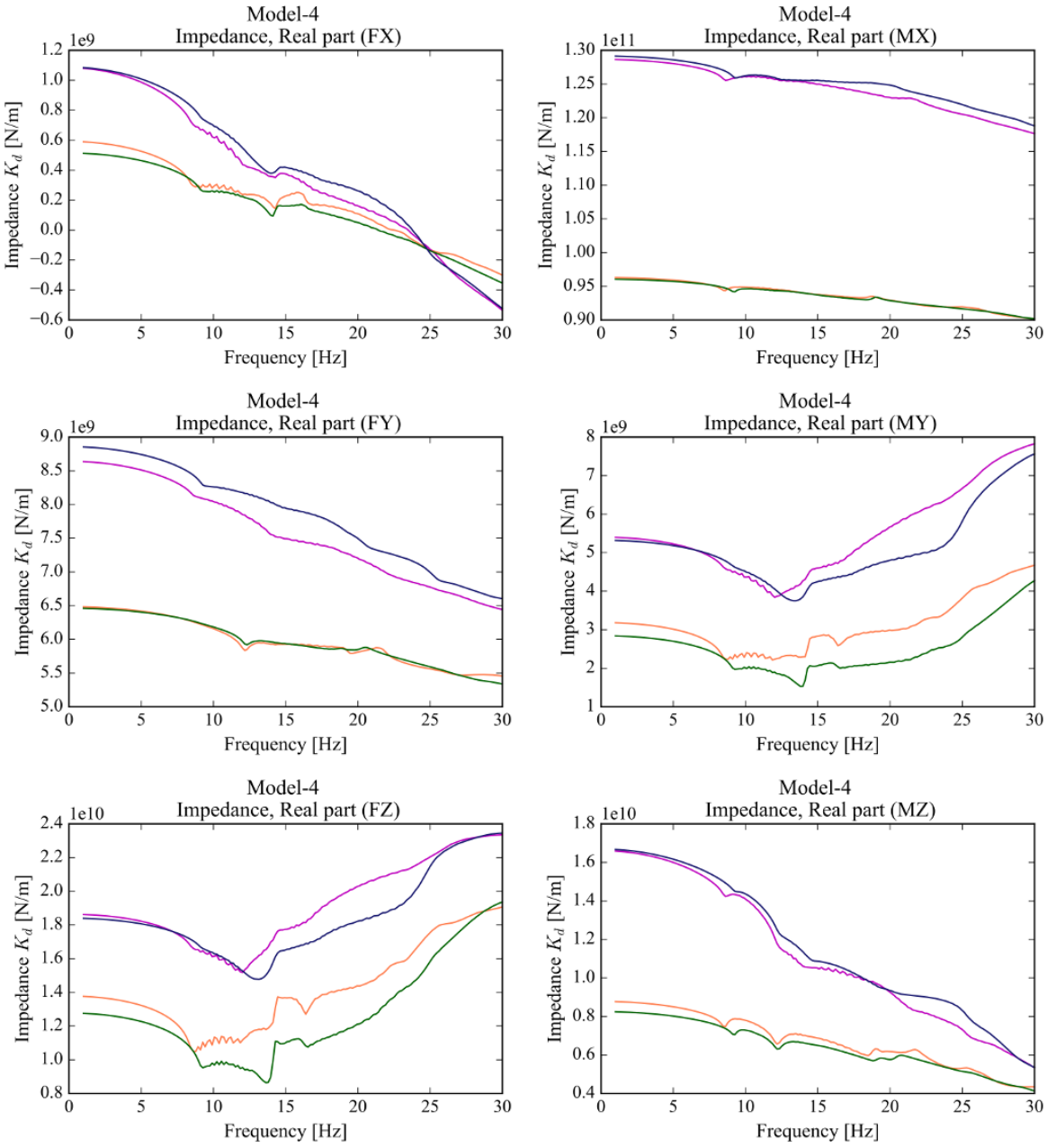
Model-4
Impedance, Real part (FX)
1e9
Impedance K_d [N/m]
Frequency [Hz]
Model-4
Impedance, Real part (MX)
1e11
Impedance K_d [N/m]
Frequency [Hz]
Model-4
Impedance, Real part (FY)
1e9
Impedance K_d [N/m]
Frequency [Hz]
Model-4
Impedance, Real part (MY)
1e9
Impedance K_d [N/m]
Frequency [Hz]
Model-4
Impedance, Real part (FZ)
1e10
Impedance K_d [N/m]
Frequency [Hz]
Model-4
Impedance, Real part (MZ)
1e10
Impedance K_d [N/m]
Frequency [Hz]
Homogenous soil, no wing walls
Homogenous soil, wing walls included
Layered soil, no wing walls
Layered soil, wing walls included

Figure A. 11

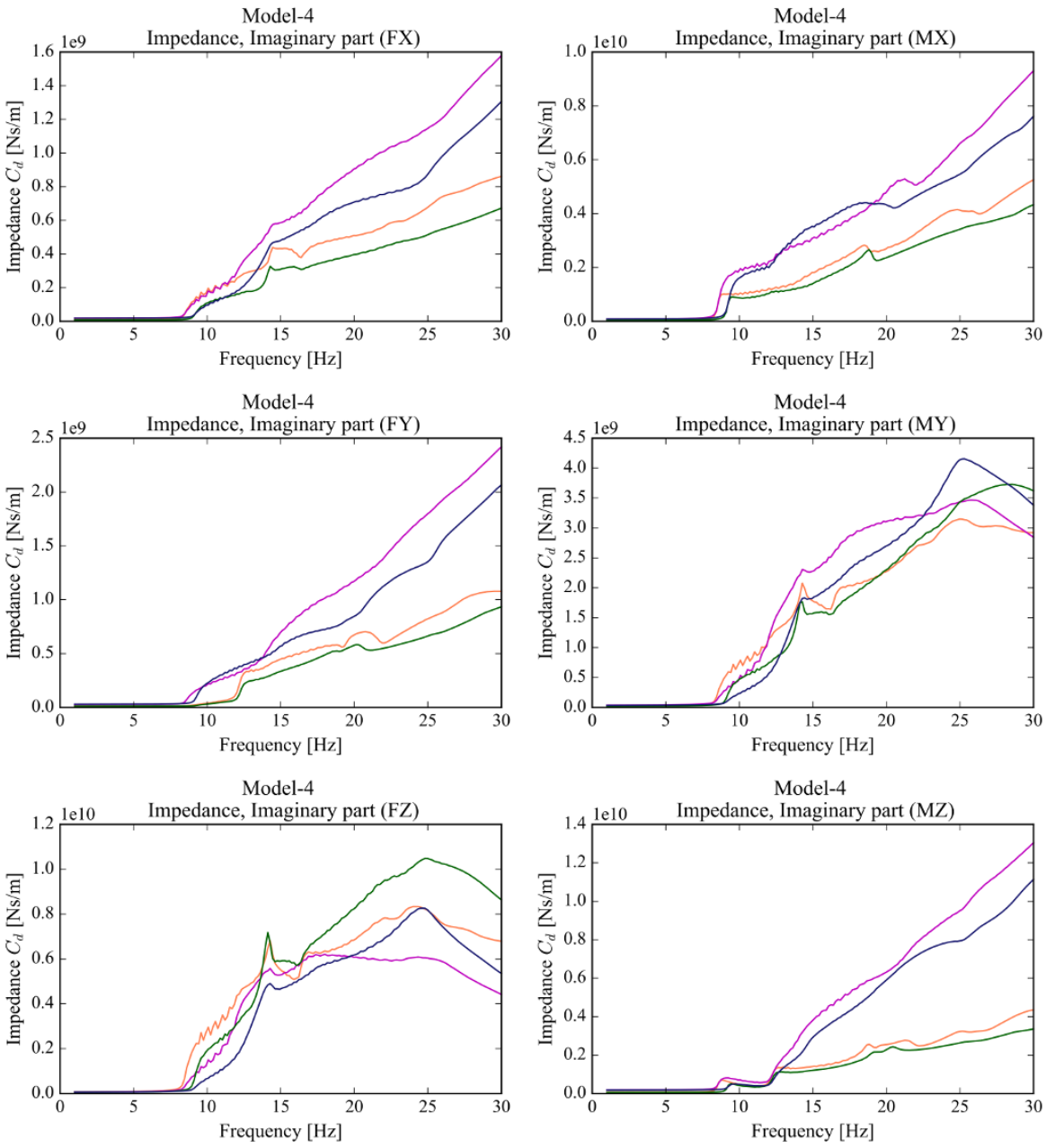
Model-4
Impedance, Imaginary part (FX)
1e9
Impedance C_d [Ns/m]
Frequency [Hz]
Model-4
Impedance, Imaginary part (MX)
1e10
Impedance C_d [Ns/m]
Frequency [Hz]
Model-4
Impedance, Imaginary part (FY)
1e9
Impedance C_d [Ns/m]
Frequency [Hz]
Model-4
Impedance, Imaginary part (MY)
1e9
Impedance C_d [Ns/m]
Frequency [Hz]
Model-4
Impedance, Imaginary part (FZ)
1e10
Impedance C_d [Ns/m]
Frequency [Hz]
Model-4
Impedance, Imaginary part (MZ)
1e10
Impedance C_d [Ns/m]
Frequency [Hz]
Homogenous soil, no wing walls
Homogenous soil, wing walls included
Layered soil, no wing walls
Layered soil, wing walls included

Figure A. 12

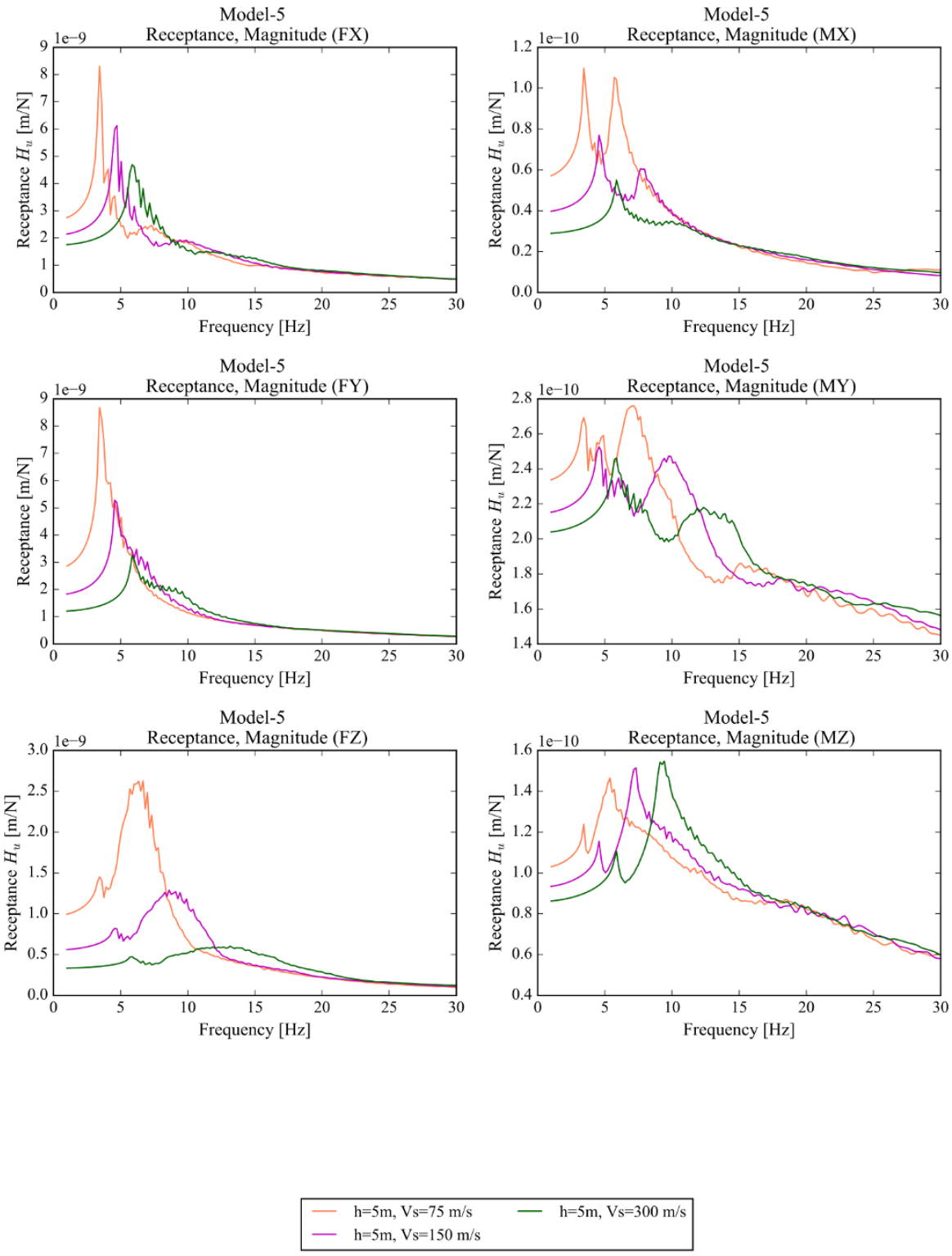
Model-5
Receptance, Magnitude (FX)
1e−9
Receptance H_u [m/N]
Frequency [Hz]
Model-5
Receptance, Magnitude (MX)
1e−10
Receptance H_u [m/N]
Frequency [Hz]
Model-5
Receptance, Magnitude (FY)
1e−9
Receptance [m/N]
Frequency [Hz]
Model-5
Receptance, Magnitude (MY)
1e−10
Receptance H_u [m/N]
Frequency [Hz]
Model-5
Receptance, Magnitude (FZ)
1e−9
Receptance H_u [m/N]
Frequency [Hz]
Model-5
Receptance, Magnitude (MZ)
1e−10
Receptance H_u [m/N]
Frequency [Hz]
h=5m, Vs=75 m/s
h=5m, Vs=150 m/s
h=5m, Vs=300 m/s

Figure A. 13

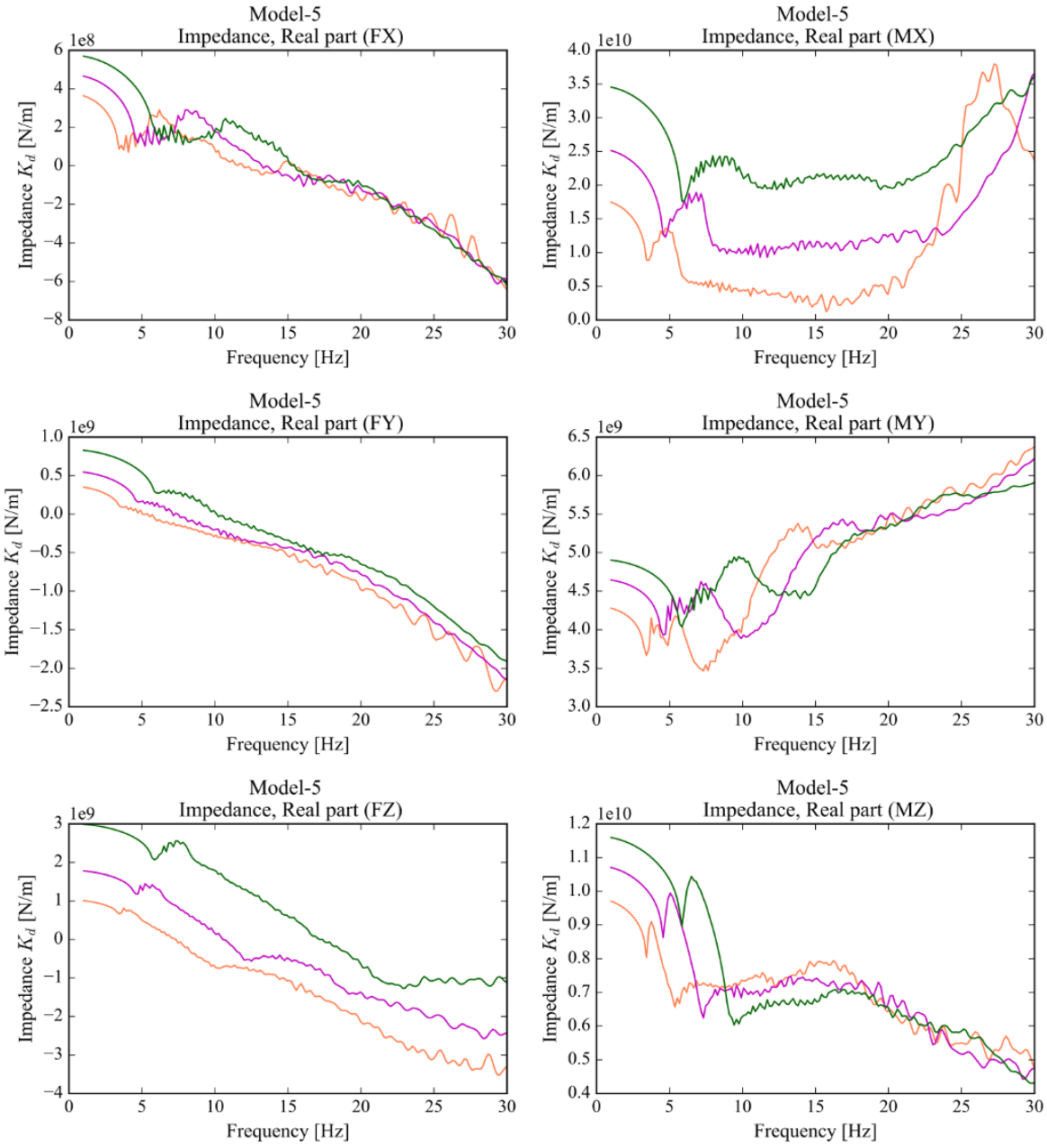
Model-5
Impedance, Real part (FX)
1e8
Impedance K_d [N/m]
Frequency [Hz]
Model-5
Impedance, Real part (MX)
1e10
Impedance K_d [N/m]
Frequency [Hz]
Model-5
Impedance, Real part (FY)
1e9
Impedance K_d [N/m]
Frequency [Hz]
Model-5
Impedance, Real part (MY)
1e9
Impedance K_d [N/m]
Frequency [Hz]
Model-5
Impedance, Real part (FZ)
1e9
Impedance K_d [N/m]
Frequency [Hz]
Model-5
Impedance, Real part (MZ)
1e10
Impedance K_d [N/m]
Frequency [Hz]
h=5m, Vs=75 m/s
h=5m, Vs=150 m/s
h=5m, Vs=300 m/s

Figure A. 14

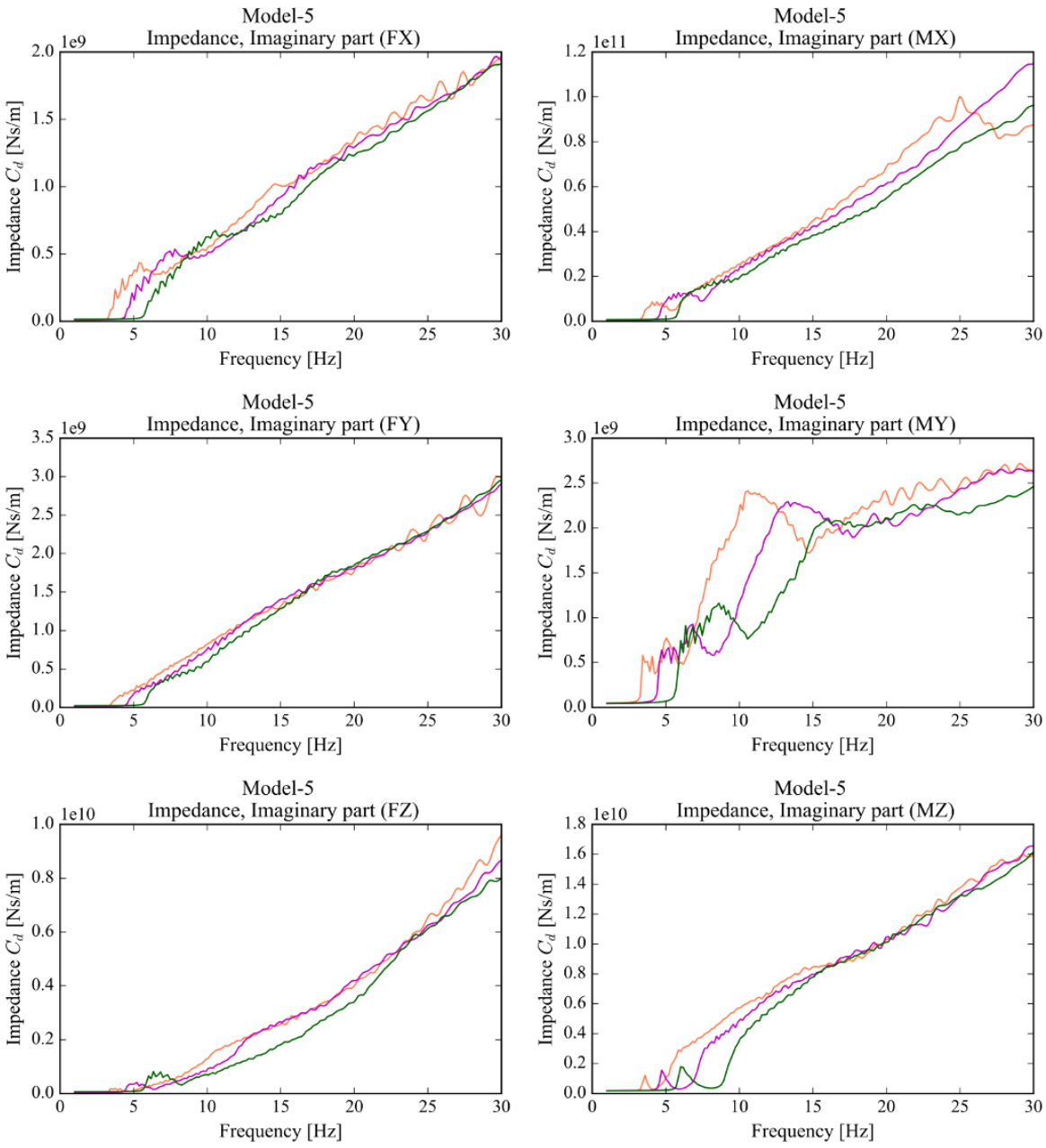
Model-5
Impedance, Imaginary part (FX)
1e9
Impedance C_d [Ns/m]
Frequency [Hz]
Model-5
Impedance, Imaginary part (MX)
1e11
Impedance C_d [Ns/m]
Frequency [Hz]
Model-5
Impedance, Imaginary part (FY)
1e9
Impedance C_d [Ns/m]
Frequency [Hz]
Model-5
Impedance, Imaginary part (MY)
1e9
Impedance C_d [Ns/m]
Frequency [Hz]
Model-5
Impedance, Imaginary part (FZ)
1e10
Impedance C_d [Ns/m]
Frequency [Hz]
Model-5
Impedance, Imaginary part (MZ)
1e10
Impedance C_d [Ns/m]
Frequency [Hz]
h=5m, Vs=75 m/s
h=5m, Vs=150 m/s
h=5m, Vs=300 m/s

Figure A. 15

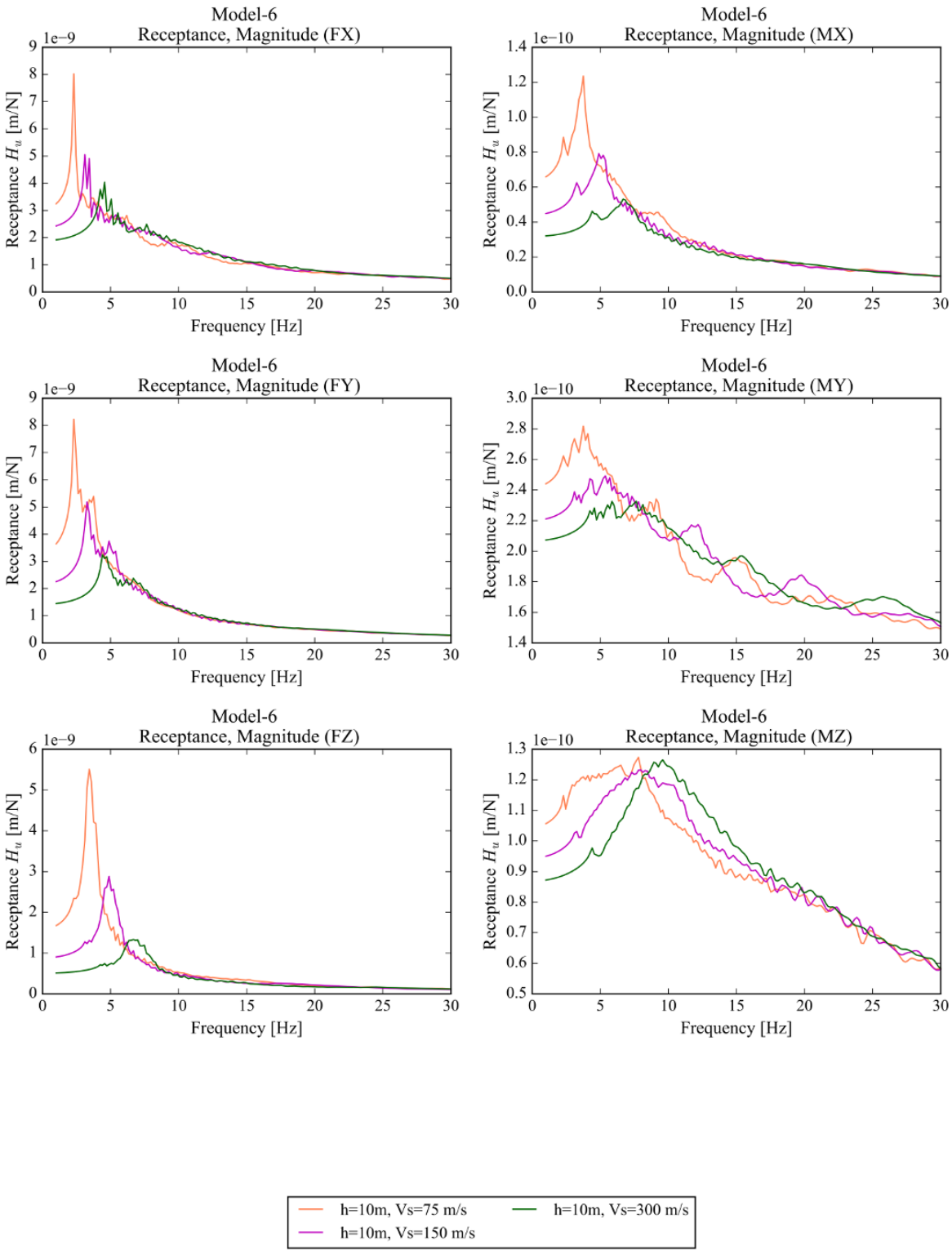
Model-6
Receptance, Magnitude (FX)
1e−9
Receptance H_u [m/N]
Frequency [Hz]
Model-6
Receptance, Magnitude (MX)
1e−10
Receptance H_u [m/N]
Frequency [Hz]
Model-6
Receptance, Magnitude (FY)
1e−9
Receptance H_u [m/N]
Frequency [Hz]
Model-6
Receptance, Magnitude (MY)
1e−10
Receptance H_u [m/N]
Frequency [Hz]
Model-6
Receptance, Magnitude (FZ)
1e−9
Receptance H_u [m/N]
Frequency [Hz]
Model-6
Receptance, Magnitude (MZ)
1e−10
Receptance H_u [m/N]
Frequency [Hz]
h=10m, Vs=75 m/s
h=10m, Vs=150 m/s
h=10m, Vs=300 m/s

Figure A. 16

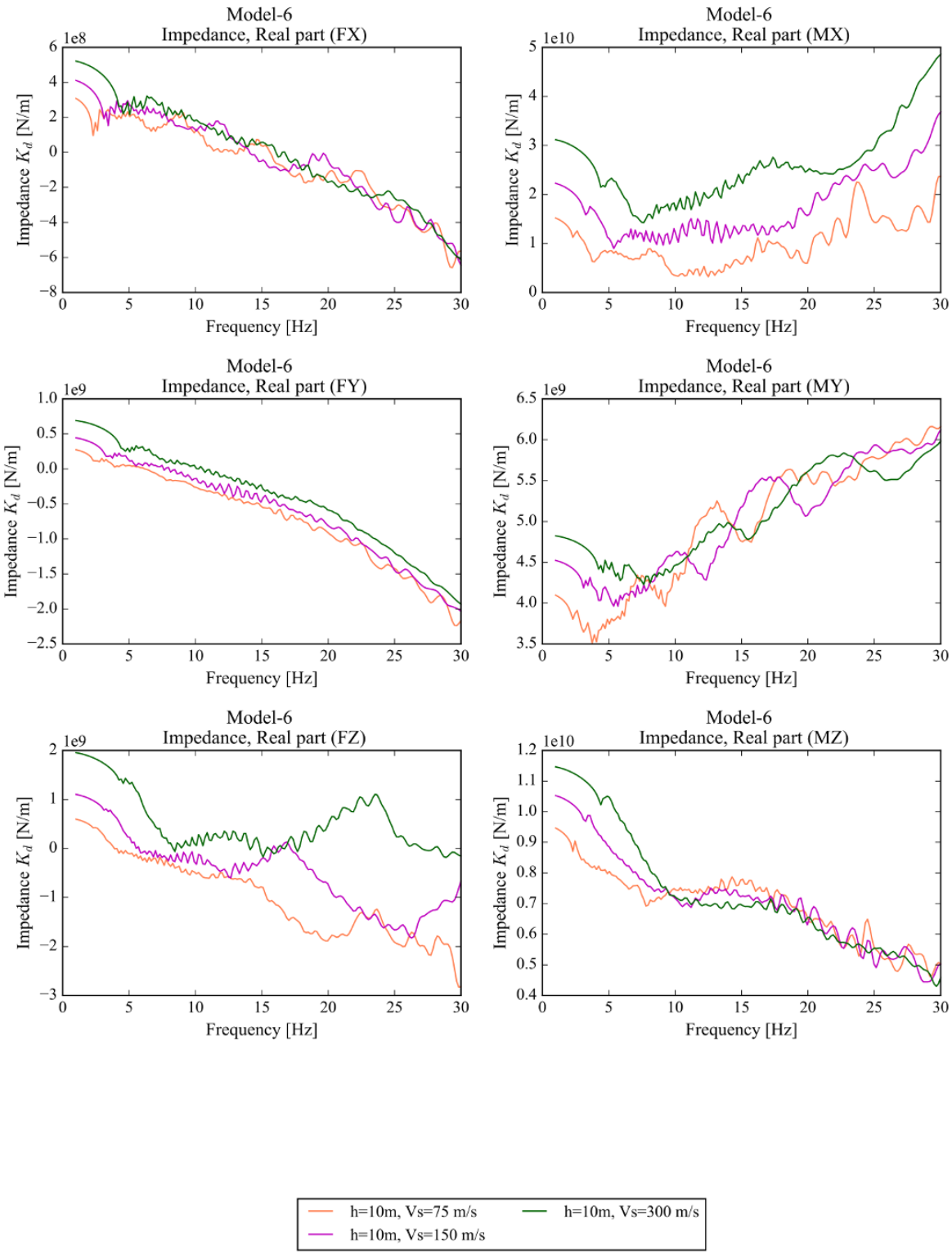
Model-6
Impedance, Real part (FX)
1e8
Impedance K_d [N/m]
Frequency [Hz]
Model-6
Impedance, Real part (MX)
1e10
Impedance K_d [N/m]
Frequency [Hz]
Model-6
Impedance, Real part (FY)
1e9
Impedance K_d [N/m]
Frequency [Hz]
Model-6
Impedance, Real part (MY)
1e9
Impedance K_d [N/m]
Frequency [Hz]
Model-6
Impedance, Real part (FZ)
1e9
Impedance K_d [N/m]
Frequency [Hz]
Model-6
Impedance, Real part (MZ)
1e10
Impedance K_d [N/m]
Frequency [Hz]
h=10m, Vs=75 m/s
h=10m, Vs=150 m/s
h=10m, Vs=300 m/s

Figure A. 17

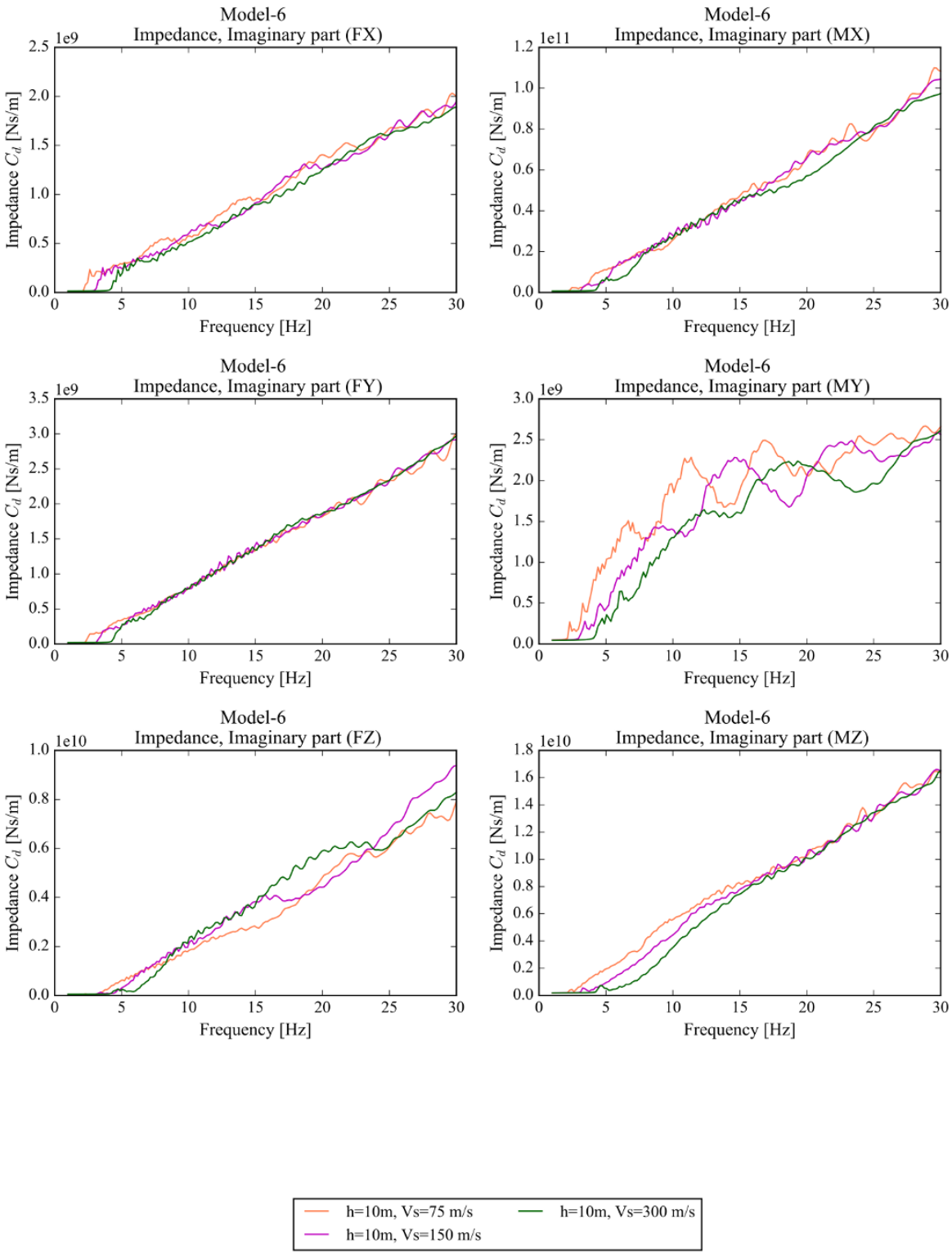
Model-6
Impedance, Imaginary part (FX)
1e9
Impedance C_d [Ns/m]
Frequency [Hz]
Model-6
Impedance, Imaginary part (MX)
1e11
Impedance C_d [Ns/m]
Frequency [Hz]
Model-6
Impedance, Imaginary part (FY)
1e9
Impedance C_d [Ns/m]
Frequency [Hz]
Model-6
Impedance, Imaginary part (MY)
1e9
Impedance C_d [Ns/m]
Frequency [Hz]
Model-6
Impedance, Imaginary part (FZ)
1e10
Impedance C_d [Ns/m]
Frequency [Hz]
Model-6
Impedance, Imaginary part (MZ)
1e10
Impedance C_d [Ns/m]
Frequency [Hz]
h=10m, Vs=75 m/s
h=10m, Vs=150 m/s
h=10m, Vs=300 m/s

Figure A. 18

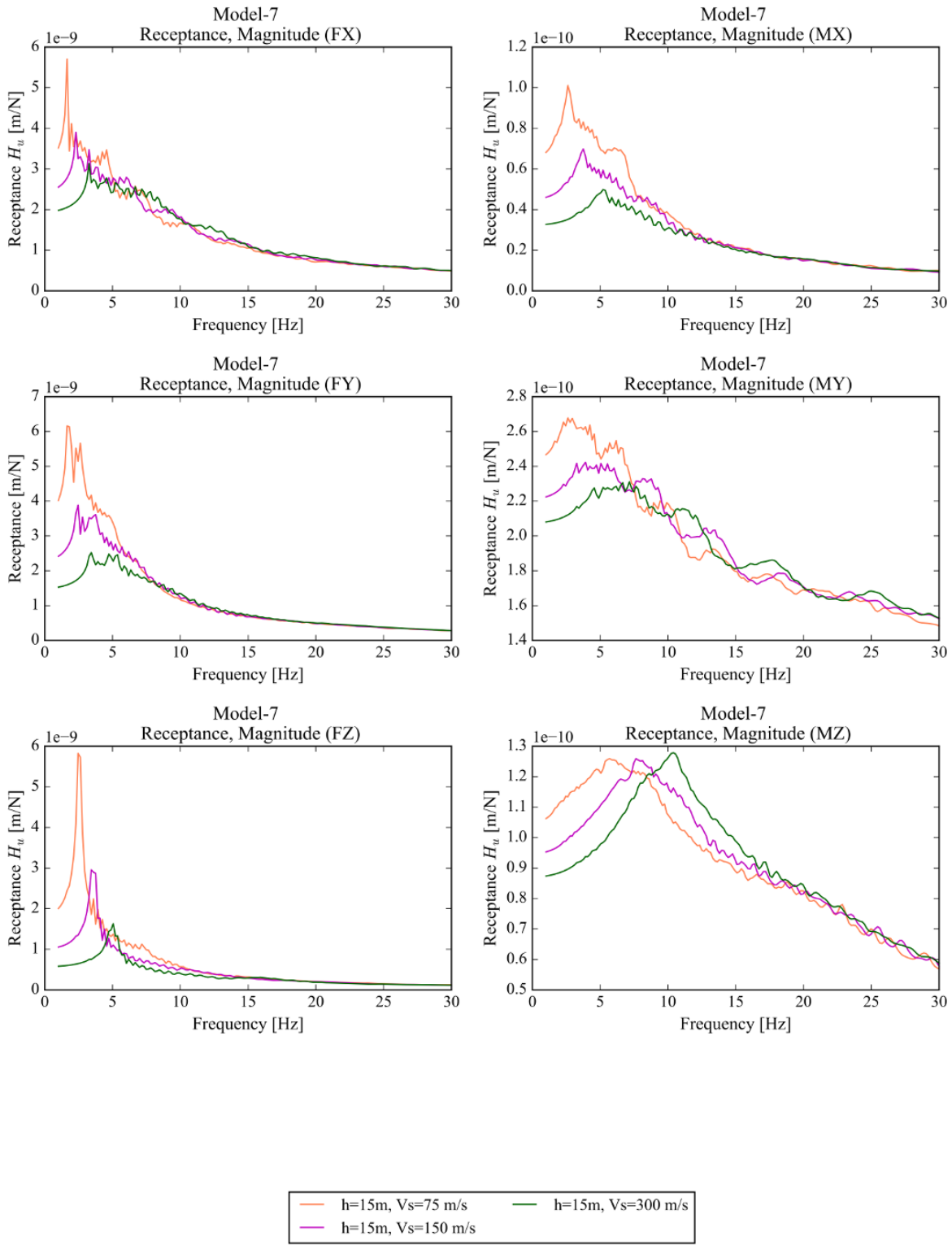
Model-7
Receptance, Magnitude (FX)
1e−9
Receptance H_u [m/N]
Frequency [Hz]
Model-7
Receptance, Magnitude (MX)
1e−10
Receptance H_u [m/N]
Frequency [Hz]
Model-7
Receptance, Magnitude (FY)
1e−9
Receptance H_u [m/N]
Frequency [Hz]
Model-7
Receptance, Magnitude (MY)
1e−10
Receptance H_u [m/N]
Frequency [Hz]
Model-7
Receptance, Magnitude (FZ)
1e−9
Receptance H_u [m/N]
Frequency [Hz]
Model-7
Receptance, Magnitude (MZ)
1e−10
Receptance H_u [m/N]
Frequency [Hz]
h=15m, Vs=75 m/s
h=15m, Vs=150 m/s
h=15m, Vs=300 m/s

Figure A. 19

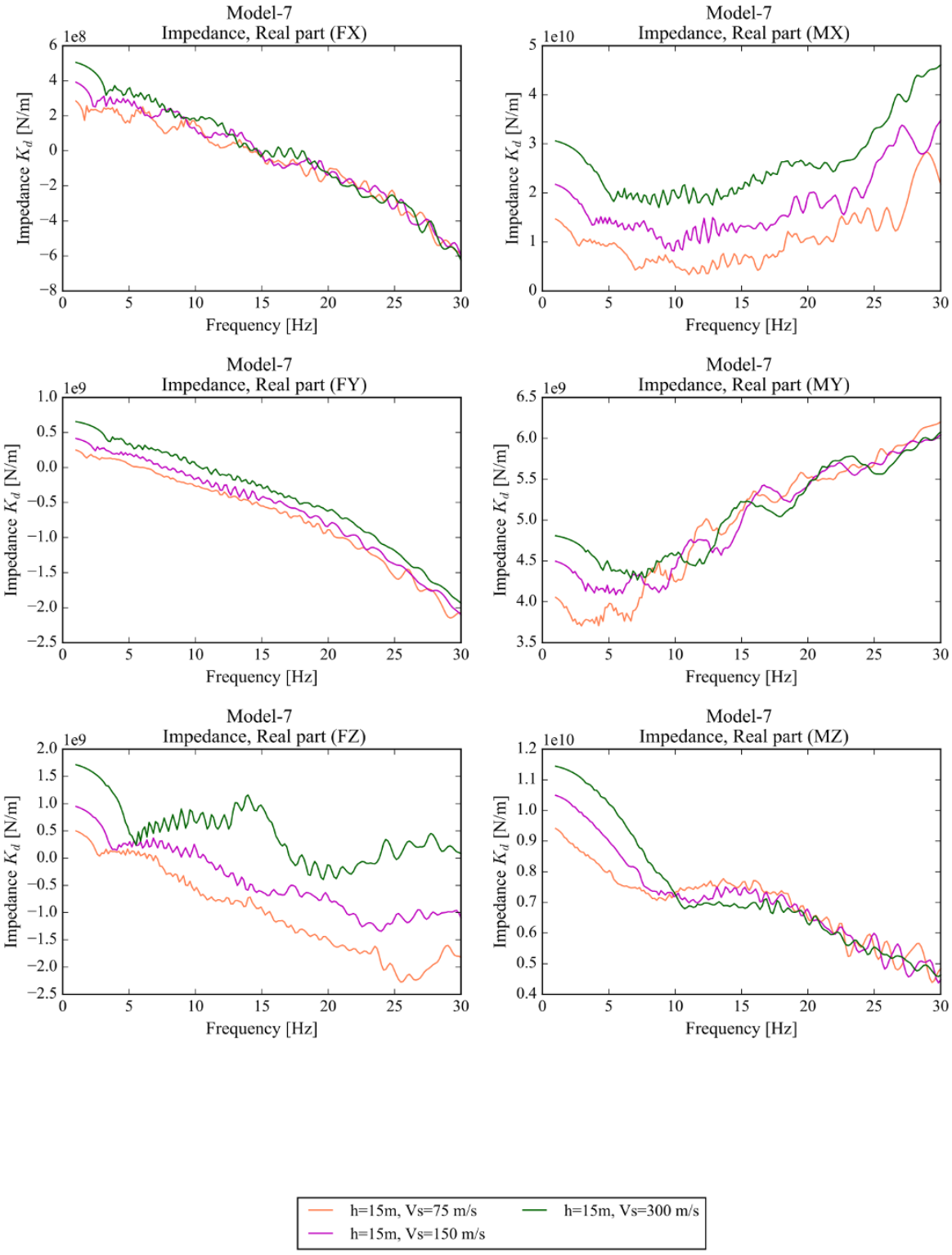
Model-7
Impedance, Real part (FX)
1e8
Impedance K_d [N/m]
Frequency [Hz]
Model-7
Impedance, Real part (MX)
1e10
Impedance K_d [N/m]
Frequency [Hz]
Model-7
Impedance, Real part (FY)
1e9
Impedance K_d [N/m]
Frequency [Hz]
Model-7
Impedance, Real part (MY)
1e9
Impedance K_d [N/m]
Frequency [Hz]
Model-7
Impedance, Real part (FZ)
1e9
Impedance K_d [N/m]
Frequency [Hz]
Model-7
Impedance, Real part (MZ)
1e10
Impedance K_d [N/m]
Frequency [Hz]
h=15m, Vs=75 m/s
h=15m, Vs=150 m/s
h=15m, Vs=300 m/s

Figure A. 20

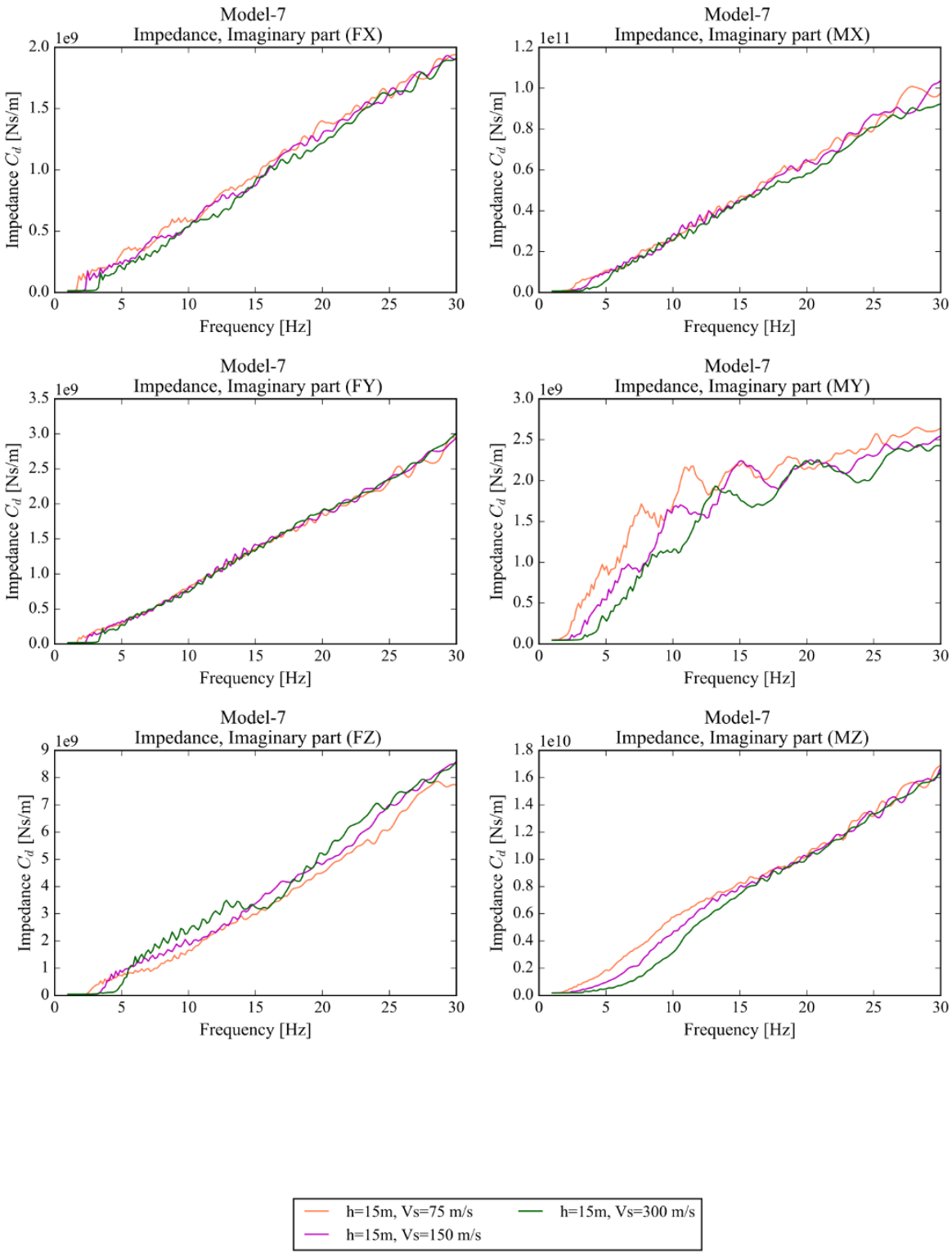
Model-7
Impedance, Imaginary part (FX)
1e9
Impedance C_d [Ns/m]
Frequency [Hz]
Model-7
Impedance, Imaginary part (MX)
1e11
Impedance C_d [Ns/m]
Frequency [Hz]
Model-7
Impedance, Imaginary part (FY)
1e9
Impedance C_d [Ns/m]
Frequency [Hz]
Model-7
Impedance, Imaginary part (MY)
1e9
Impedance C_d [Ns/m]
Frequency [Hz]
Model-7
Impedance, Imaginary part (FZ)
1e9
Impedance C_d [Ns/m]
Frequency [Hz]
Model-7
Impedance, Imaginary part (MZ)
1e10
Impedance C_d [Ns/m]
Frequency [Hz]
h=15m, Vs=75 m/s
h=15m, Vs=150 m/s
h=15m, Vs=300 m/s

Figure A. 21